Magnetic Resonance of Paramagnetically Doped Materials

James Wilman, MPhys

Thesis submitted to the University of Nottingham for the degree of Doctor of Philosophy

September 2016

Abstract

Colloidal quantum dots (QDs) allow for the tuning of dopant concentration as well as flexibility in the engineering of the surrounding medium. This thesis explores the use of magnetic resonance techniques and the development of hardware in order to characterize paramagnetically doped materials, in particular Mn-doped PbS colloidal QDs, and assess their potential for applications in quantum technologies such as quantum information processing (QIP).

Colloidal PbS:Mn QDs capped with thioglycerol/dithiolglycerol ligands were synthesised in aqueous solution. Methods of tailoring the Mn-Mn and Mn-^{1}H interactions, with the aim of maximizing phase memory times, were investigated. The distance between spins was optimized by initially, overgrowing the QDs with an undoped shell and secondly, by dispersing the QDs in solution. The use of a deuterated solution was found to further reduce the dephasing effects of Mn-^{1}H interactions. This resulted in unprecedentedly long phase memory (T_M ~ 8 μs) and spin–lattice relaxation (T_1 ~ 10 ms) time constants for Mn^{2+} ions at T= 4.5 K, and in the observation of electron spin coherence (T_M ~ 1 μs) near room temperature. Further improvements to relaxation times, as well as enhanced optical properties useful for the initialization and readout of spin qubits, were also studied by embedding the QDs in photonic crystals.

Magnetic resonance techniques combined with paramagnetic Mn-impurities in PbS QDs are used for sensitive probing of the QD surface and environment. We report inequivalent proton spin relaxations of the capping ligands and solvent molecules. We determine the strengths and anisotropies of the Mn-^{1}H spin interactions, and establish Mn-^{1}H distances with ~1 Å sensitivity. These findings demonstrate the potential of magnetically doped QDs as sensitive magnetic nano-probes and the use of electron spins for surface sensing.

We explore a means of characterizing mechanisms responsible for the functionality of paramagnetically doped materials. The development of instrumentation to identify and quantify interactions between paramagnetic and ordered magnetic

phases is described. A probe was designed and built with a fast response time and with the aim of facilitating fast field jump experiments to identifying interactions between the different magnetic phases by correlating the response of a sample to mw irradiation with its response to a field jump.

List of Publications

Electron spin coherence near room temperature in magnetic quantum dots
Fabrizio Moro, Lyudmila Turyanska, James Wilman, Alistair J. Fielding, Michael W. Fay, Josef Granwehr & Amalia Patanè, *Scientific Reports*, 5, 10855 (2015)
DOI: 10.1038/srep10855

Surface sensing of quantum dots by electron spins
Fabrizio Moro, Lyudmila Turyanska, James Wilman, Huw E. L. Williams, Alistair J. Fielding, Amalia Patanè, *Nano Letters*, 16 (10), 6343-6348 (2016)
DOI: 10.1021/acs.nanolett.6b02727

Aknowledgments

I would like to express my gratitude to my supervisors, Dr Lyudmila Turyanska and Dr Josef Granwehr for all their support and encouragement during my studies. I would also like to thank Dr Fabrizio Moro for his assistance, friendship and patience. Thanks also to the academic support from Professor Amalia Patané, Dr Jim Leggett, Dr Sankeerth Hebbar, Dr Peter Roberts and Mr Alan Dorkes at the University of Nottingham, Dr Alistair Fielding at the University of Manchester, all the staff from the Integrated Magnetic Resonance Centre (iMR CDT) and my examiners: Professor Tony Horsewill and Professor Eric McInnes.

This work was supported by the University of Nottingham, the Engineering and Physical Sciences Research Council (EPSRC) iMR CDT, the EPSRC national EPR facility at the University of Manchester, and the Leverhume Trust. I also thank Dr Walter Köckenberger for access to the W-band ESR spectrometer at the Sir Peter Mansfield Magnetic Resonance Centre (SPMMRC) and Dr Jonathon McMaster and Dr Stephen Williams for use of the X-band ESR spectrometer at the School of Chemistry, University of Nottingham.

Finally, I would like to give a special thank you to my friends and family, and all my colleagues at the University of Nottingham and the iMR CDT for their invaluable friendship and support.

Contents

Chapter 1 1

1.1 Colloidal quantum dots 1

1.2 Doped colloidal quantum dots 6

1.3 Material systems for quantum information processing 10

Chapter 2 20

Experimental Techniques 20

2.1 Colloidal growth 20

2.2 Morphological characterization 21

2.3 Electron Spin Resonance 22

2.4 Nuclear Magnetic Resonance 30

2.5 Optical Studies 31

Chapter 3 35

Properties of Mn^{2+} doped QDs 35

3.1 Morphological, optical and magnetic properties of PbS:Mn 35

3.2 Design of core/shell QDs 41

3.4 Pulsed-ESR studies 43

3.5 Discussion 46

Chapter 4 48

Electron spin coherence near room temperature 48

4.1 Designing QDs for increased T_M 49

4.2 Continuous–wave ESR 49

4.3 Mn–Mn dipolar interactions 51

4.4 Nuclear spin bath dephasing. 54

4.5 Electron–nuclear interactions 55

4.6 Spin dynamics temperature dependence 57

4.7 Discussion 60

Chapter 5 62

Photonic crystals 62

5.1 Design and fabrication of photonic cavities 63

5.2 Micro-PL mapping 65

5.3 Discussion 66

Chapter 6 68

Surface sensing of QDs by electron spins 68

6.1 Introduction 68

6.2 Materials 70

6.3 ^{1}H-NMR 71
6.4 Pulsed-ESR 78
6.5 Discussion 82
Chapter 7 84
Developing magnetic resonance instrumentation to study paramagnetically doped materials with mixed magnetic phases 84
7.1 Introduction 84
7.3 $KCr_3(SO_4)_2(OD)_6$ CW-ESR measurements 85
7.4 Hardware development 87
7.5 Discussion 95
Chapter 8 97
Conclusions and Outlook 97
Bibliography 100

List of Figures

Figure 1-1 A schematic diagram illustrating the changes in electronic density of states that occur as dimensionality is varied from 0D to 3D [2]. 2
Figure 1-2 Size-dependent PL properties of different material systems [8] 3
Figure 1-3 Self-purification process for a doped lead-salt structured nanocrystal. 10
Figure 1-4 The Bloch sphere represents the superposition of the basis of states,|1⟩ and |0⟩, of a qubit. 12
1-5 Diagram illustrating the principle of a micropillar cavity 17
Figure 2-1 Scheme of the hyperfine interaction between unpaired electron spins and the surrounding nuclear spins. The nuclear magnetic moment can add (a) and reduce (b) the overall magnetic field. 24
Figure 2-2 Splitting of the m_s = ±1/2 states due to I = 5/2 showing the transitions resulting from hyperfine interactions ($\Delta m_S=\pm1,\Delta m_I=0$). Lower inset presents absorption spectrum of $2I$+1 lines, where the distance between the peaks defines the hyperfine coupling, A.....24
Figure 2-3 Simplified scheme of a CW ESR spectrometer.....25
Figure 2-4 Spin echo sequence. 26
Figure 2-5 Spin echo sequences used for pulse ESR: (a) Inversion recovery sequence, (b) Nutation pulse sequence, (c) Davies ENDOR pulse sequence, (d) Mims ENDOR pulse sequence. 28
Figure 2-6 Experimental set-up for LOD ESR. A pick-up coil, oriented parallel to B_0, is integrated into a serial *LCR* circuit, and the detected signal is the voltage, V, across the capacitor, C [107].....30
Figure 2-7 NMR inversion recovery sequence 31
Figure 2-8 Schematic diagram of the PL mechanism in a direct band gap bulk 32
Figure 2-9 Schematic of experimental setup used in micro-PL studies.....33
Figure 2-10 Set-up for fabrication of 3D structures by 2PP [109].....34
Figure 3-1 (a) HRTEM images of Mn-doped PbS nanoparticles. (b) Histogram showing the size distribution of the QDs as derived from AFM for

PbS QDs with Mn_{EDX} = 0% (black bars) and 5% (patterned bars). Inset: AFM image of Mn-doped PbS QDs [112]. 36
Figure 3-2 (a) EDX spectrum (b) Mn content measured by EDX, Mn_{EDX} , as a function of the nominal Mn content. The dashed line is a guide to the eye. The right axis represents the number of Mn ions per QD [18]. 37
Figure 3-3 (a) PL Spectrum for QDs with Mn = 7 % showing the Mn-dopant PL emission at 1.9 eV and the emission from the QDs at lower energy at T = 300 K, laser excitation, λ = 633 nm, P = 25 W/cm^2 [13]. (b) Normalized PL spectra of Mn-doped PbS nanocrystals [112]. 38
Figure 3-4 Dependence of the QD PL peak energy, E_{QD}, on x (T = 295 K). The continuous line represents the calculated dependence of E_{QD} on x according to the model described in the text. The inset shows the Mn content as estimated from EDX (Mn_{EDX}, stars) and from the calculated and measured values of E_{QD} (Mn_{PL}, dots). To account for different values of E_{QD} at x = 0%, in the calculation of E_{QD}, we have assumed QD radii in the range R = 2.5–2.6 nm [18]. 39
Figure 3-5 Room temperature K-band EPR spectra for Mn-doped PbS nanocrystals with Mn content, Mn = 0.5 to 5% [18]. 40
Figure 4-1 Representation of magnetic interactions between Mn ions (red arrows) in two neighbouring PbS QDs dispersed in water. The hyperfine interactions between Mn spins and proton nuclear spins of the capping ligands and solvent matrix are shown. The continuous lines indicate strong interactions while the dotted lines indicate weak interactions. 49
Figure 4-2 (a) X-band CW-ESR spectrum (dotted line) for powder sample of $Mn_{0.05\%}$ and simulation (continuous line) to a spin-Hamiltonian model. (b) Experimental W-band CW ESR spectrum and simulations performed with cubic, a, (blue) and axial, D, (red) symmetry with D strain of 30%. 51
Figure 4-3 Spin dynamics for quantum dots in different matrices. (a) Hahn echo decay for $Mn_{0.05\%}$ as powder and frozen solutions at T = 5 K. Black lines are fits to stretched exponential (Eq. 2.5). (b) Inversion recovery echo trace for powder sample with biexponential fit (Eq.2.6) (black line). 51
Figure 4-4 EFS spectrum measured for a powder $Mn_{0.05\%}$ sample at T = 5 K with a maximum echo intensity at B = 345 mT. 52

Figure 4-5 Spin echo decay traces for Mn0.01% at T = 5 K as powder (dark green) and as frozen solution (light green). 53
Figure 4-6 Spin dynamics for quantum dots in deuterated solution for $Mn_{0.05\%}$ at T = 5 K. (a) Spin echo decay. Black lines are fits to stretched exponential (Eq. 2.5). Inset: representation of QDs in D_20/glycerol-D_8. (b) Inversion recovery echo trace with biexponential fit (Eq. 2.6) (black line). 54
Figure 4-7 Spin echo decay traces recorded for $Mn_{0.05\%}$ in different deuterated solvent matrices at T = 5 K and B = 345 mT.....55
Figure 4-8 Electron–nuclear spin dynamics. 2p-ESEEM traces of $Mn_{0.05\%}$ powder (red circles) and $DMn_{0.05\%}$ frozen solution in D_2O/glycerol-D_8 (grey circles) at T = 5 K and their Fast Fourier Transform (inset). Black lines are simulations by equation (4.3).....57
Figure 4-9 Temperature dependence of T_M (spheres), $1/T_M$ (stars), and s for $Mn_{0.05\%}$ in H_2O/glycerol-H_8. 58
Figure 4-10 (a) Spin echo decay traces for 4.5 K≤T≤200 K. (b) Inversion recovery traces for 4.5 K ≤T≤150 K. (c) Temperature dependence for T_M (spheres) and T_1 (triangles) for $DMn_{0.05\%}$ in D_2O/glycerol-D_8. Dashed lines are guides for the eye. 59
Figure 5-1 Diagram showing the photonic crystal design with a cavity of length, l = 0.5 μm and polymer rods of radius, r = 0.1 μm, lattice constant, a = 0.35 μm and *height* = 0.7 μm.....64
Figure 5-2 2PP micromachined photonic crystal designed to have a cavity of length, l = 0.5 μm (a) and fabricated with a cavity of length, l ~ 1μm (b). 65
Figure 5-3 (a) CCD image of the photonic crystal with the XY-map area defined by the green square with corresponding cursor PL spectrum. Inset: Result of the micro-PL mapping. (b) Experiment repeated with a second photonic crystal of the same dimensions. 66
Figure 6-1 Echo field swept spectrum recorded at Q-band (ν_{mw} = 33.85 GHz) for D-PbS:Mn solid state sample with Mn concentration of 0.03%. The arrow indicates the magnetic field position (B = 1.211 T) at which the pulsed-ESR experiments were conducted. 70

Figure 6-2 Schematic of a PbS:Mn QD and zoom of a surface Mn ion interacting with the TGL capping ligands and TEA solvent molecules in water solution. 71
Figure 6-3 Overview of ^{1}H-NMR spectra for solutions of undoped PbS QDs, TEA and TGL molecules. Insets are skeletal formulas for TGL and TEA..... 72
Figure 6-4 TEA peaks shifted downfield in PbS QDs. (a) 2, 4 and 5 CH_2 peaks and (b) 1, 5, and 7 CH_3 peaks. 73
Figure 6-5 TGL peaks are shifted in PbS QDs. (a) The 3CH peak is shifted upfield becoming almost unresolved in the QDs, 4' and 4" CH2 peaks are shifted downfield and separation is increased in the QDs, and (b) 2', and 2" CH2 peaks are shifted upfield in the QDs and the separation is decreased. 74
Figure 6-6 HSQC spectra of TGL and PbS QDs. The peaks assigned to the CH-groups of TEA and TGL molecules for the PbS QDs indicated. The different colour tone is used to distinguish between odd and even CH-groups. 74
Figure 6-7 (a) ^{1}H-NMR spectra for PbS QDs undoped and doped with Mn concentrations of 0.01 %, 0.03 % and 0.1 %. Peaks corresponding to TEA (a) and TGL (b) CH-groups are indicated. 75
Figure 6-8 Comparison between 1H- MR spectra for TGL (a) and TEA (b) molecules free in a solution containing $MnAc_2$ molecules (red curve) and bonded to Mn^{2+} - doped PbS QDs (black curve) with Mn concentration, Mn = 0.03%. 76
Figure 6-9 ^{1}H-NMR relaxation rates ($1/T_1$) for the TGL (a) and TEA (b) CH-groups of PbS:Mn QDs with Mn concentrations: 0 %, 0.01 %, 0.03 %, 0.05 % and 0.1 %. Calculated Mn induced magnetic fiels (B_e) and average distance, d between Mn and CH groups of the TGL (c) and (d) show the distance,*d* between Mn-spins and protons of TGL and TEA molecules and the magnetic field (B_e) generated by the Mn-spin impurity. 77
Figure 6-10 ^{2}H-ESEEM (a) ^{1}H-ENDOR-Mims (Inset: ^{1}H-ENDOR-Mims for a sample in deuterated solution) (b) and ^{55}Mn-Davies-ENDOR (c) Q-band spectra at T = 5 K for the PbS:Mn QD sample along with the simulations (green curve = matrix line, blue curve = ^{1}H and ^{2}H interacting with Mn ions, red curve = total contribution). The ^{1}H-Mims-ENDOR spectrum has been inverted along the intensity axis. 80

Figure 6-11 CW-ESR spectrum at X-band for PbSMn (Mn =0.05%) solid state (black curve) and simulation (red curve). 81
Figure 7-1 Normalized CW ESR temperature dependence for $KCr_3(SO_4)_2(OD)_6$ powder sample. 86
Figure 7-2 Diagram illustrating the probe structure and gradiometer tuning mechanism and a photograph of the finished probe 88
Figure 7-3 Diagram and photograph showing the axial gradiometer detection coil. 90
Figure 7-4 Layout of wires in each layer of multi-layer self-shielding coil (crosses denote the direction of the current) and photograph of the finished coil with layer 5 visible. 92
Figure 7-5 (a) Simulated field outside shielded multi-layer coil. (b) Field outside shielded coil (*r*: perpendicular distance from the coil centre, *z*: axial distance from the centre of the coil). The black dashed line represents the magnet bore and the red dashed line represents the edge of the coil. 93
Figure 7-6 Gaussmeter measurements outside shielded coil, along 'notches' (*r*: perpendicular distance from the coil centre, *z*: axial distance from the centre of the coil). The pink lines represent the 'normal' field (as Fig. 7.6b), the black dashed line represents the magnet bore and the red dashed line represents the edge of the coil. 93
Figure 7-7 (a) simulated field over one quadrant of the sample. (b) Field inside the shielded coil over 1 quadrant of the sample cup (*r*: perpendicular distance from the coil centre, *z*: axial distance from the centre of the coil). The black dashed line represents the edge of the sample cup. 94
Figure 7-8 Field inside the shielded coil (*r*: perpendicular distance from the coil centre, *z*: axial distance from the centre of the coil). The red dashed line represents the axial distance to the end of the coil. 95

List of Tables

Table 3-1 List of samples.....43
Table 4-1 Results of the fittings of the spin echo decay (Eq. 2.5) and inversion recovery data (Eq. 2.6) for Mn = 0.05 %. 51
Table 4-2 Results of fitting to the spin echo decay (Eq. 2.5) and inversion recovery (Eq. 2.6) data for Mn = 0.01 %. 54
Table 4-3 Results of fitting to the spin echo decay (Eq. 2.5) and inversion recovery (Eq. 2.6) data for Mn = 0.05 % in deuterated solution. 54
Table 4-4 Fitting parameters for the 2p-ESEEM trace (Eq. 4.3). 57
Table 4-5 Fitting parameters for the spin echo and inversion recovery traces shown in Figure 4-10 for $DMn_{0.05\%}$ in D_2O/glycerol-D_8. 59
Table 6-1 pulsed ESR simulation parameters for ^1H and ^2H. 80

Chapter 1

Controlling the size, shape and chemical composition of quantum dots (QDs) allows for the manipulation of their electronic, optical and magnetic properties leading to the possibility for novel applications such as quantum information processing (QIP), bioimaging and nanocrystal lasers. However, the exact effect of changing the QD structure and composition, and of incorporating different magnetic impurities, is as yet unknown and requires further study.

This chapter starts with an introduction to the subject of colloidal QDs in general and doped colloidal QDs. This is followed by a review of material systems for QIP, starting with an introduction to the criteria necessary for the realisation of a quantum computer and providing an overview of material systems that use the same control mechanism as the system being studied in this thesis.

1.1 Colloidal quantum dots

Colloidal QDs are semiconductor nanocrystals produced by colloidal chemistry whereby the nanocrystals are synthesized in solution and capped by a layer of

organic ligand molecules. The capping ligands prevent uncontrolled growth and stabilize the QD size and composition by chemical passivation of surface dangling bonds [1]. There is a variety of alternative 'physical' approaches to fabricating QDs, such as, molecular-beam-epitaxy (MBE) and metalorganic-chemical-vapor-deposition (MOCVD).

Colloidal QDs are 0D structures, i.e. the electron motion is confined in all three spatial directions resulting in quantization. They may be comprised of fewer than a hundred atoms or as many as a few tens of thousands of atoms with typical dimensions ranging from 1 to 100 nm.

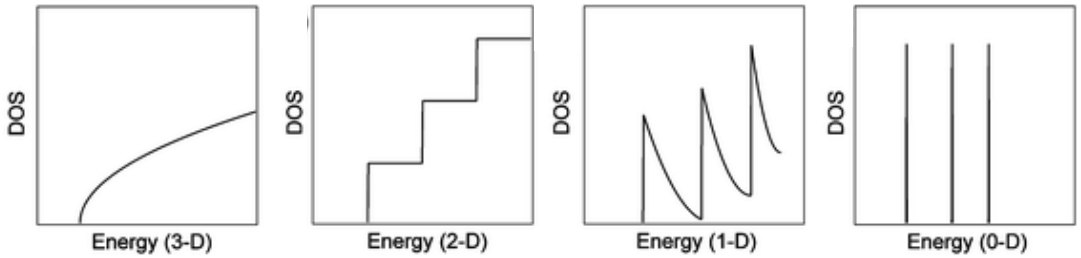

Figure 1-1 A schematic diagram illustrating the changes in electronic density of states that occur as dimensionality is varied from 0D to 3D [2].

Reducing the size of semiconductor structures to a size that is smaller than its exciton Bohr radius results in quantum confinement, as predicted by Efros and Efros in 1982 [3] and later confirmed experimentally by Ekimov et al. working on CdSe nanocrystals [4]. This reduction in size leads to changes in the dimensionality of a material which, when varied from 3D to 0D, leads to changes in the electronic density of states (Figure 1-1). In 0D structures, discrete δ-function-like electronic states are observed in the valence and the conduction bands. A consequence of these 'atomic-like' states is the unique optical and electronic properties observed in QDs [5] which have led to research covering a broad range of applications.

There are several advantages to using colloidal synthesis; these include high thermal and photo-stability [6], low cost and high rate of production. Colloidal growth provides greater flexibility to control QD size and composition. QDs have strongly size dependent energy gaps and, as such, controlling the size enables tunability of optical emission from UV to NIR (Figure 1-2). This effect can be approximated

with a simple 'quantum box' model for which the size dependent contribution to the energy gap is given by,

$$E_{QD} = E_g + \frac{\hbar^2 \pi^2}{2m_{eh}R^2} \ , \tag{1.1}$$

where E_g is the energy gap of a bulk semiconductor, R is the radius of the QD and m_{eh} is defined as, $m_e m_h/(m_e+m_h)$, where m_e and m_h are the effective masses of the electron and hole respectively [7]. As well as size, the chemical composition in colloidal QDs can be controlled. This allows for the incorporation of dopants, and hence, a means to manipulate electronic and magnetic properties.

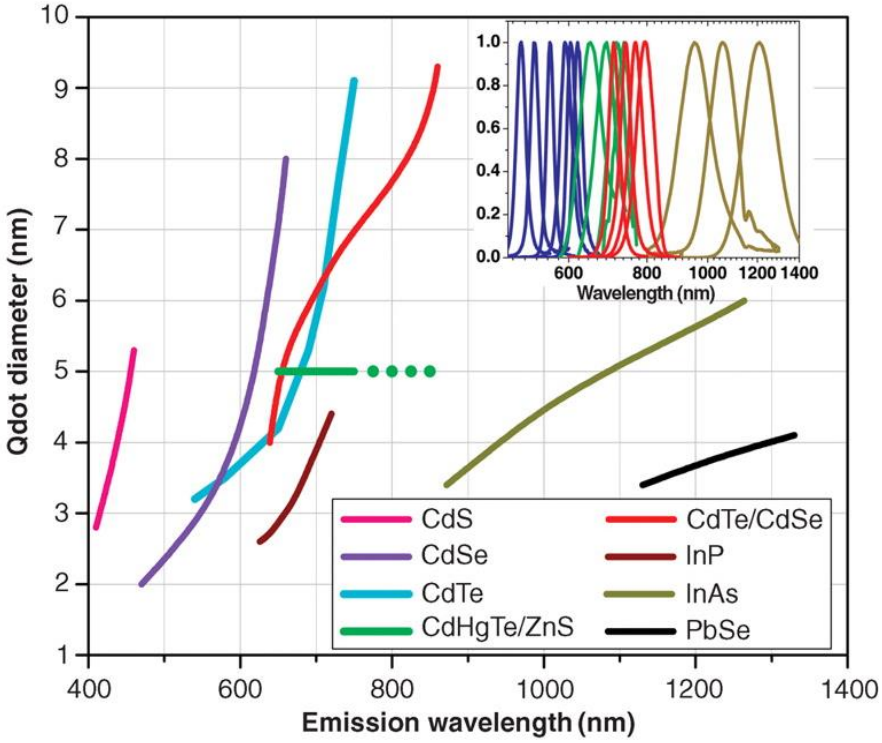

Figure 1-2 Size-dependent PL properties of different material systems [8]

Following on from the work of Ekimov, most of the early research into the electronic and optical properties of nanocrystal QDs was done on the II-VI compound, CdSe due to the ease with which high quality samples could be prepared. This was followed by work on CdS and CdTe in which excellent optical and electrochemical properties were also observed.

Novel physical and chemical behaviour has been observed as a result of manipulating matter on a nanometre length scale, such as, multiple exciton generation, enhanced quantum yield [9] as well as enabling multiple applications of QDs.

Much of the research into nanomaterials has been motivated by biological applications, such as luminescent biolabels. In 1998 Chan et al. reported highly luminescent ZnS-capped CdSe nanocrystals covalently coupled to biomolecules for use in ultrasensitive biological detection [10]. These biolabels were shown to be 20-times brighter than organic dyes such as rhodamine, 100-times more stable against photobleaching, and one-third as wide in spectral linewidth [10]. In the same year Bruchez et al. published results of their work on photostable semiconductor nanocrystals with narrow, tunable emission spectra for use as fluorescent probes in biological staining and diagnostics [11].

These studies were followed in subsequent years by many advances in the use of nanomaterials for a range of biomedical research, imaging and clinical applications. The cytotoxicity observed in cadmium-based QDs provided the motivation to develop more biocompatible, Cd-free nanocrystals. Alternative systems, such as Ag_2Se [12], Ag_2S [13], InP [14], $CuInS_2/ZnS$ [15] or Si, were explored and have been shown to be safer than Cd under UV irradiation [16]. Another example of Cd-free QDs is C-dots. These have the advantage of being benign, abundant and inexpensive as well as having strong, tuneable PL emission which, unlike many systems used in this field, can extend to the NIR spectral region [17]. UV emission can cause tissue damage, and visible emission has a shallow tissue penetration depth. Therefore, there is an advantage in establishing systems like C-dots which emit in the NIR and, as such, have low absorption and scattering in living tissue [18, 19]. However, addressing the solubility of these materials in physiological solvents remains challenging. Further improvements to synthesis techniques are required to optimize the coupling of magnetic and optical properties, to maintain PL quantum yields, and to enable versatile functionalization and the reduction in the toxic effects of the nanomaterials [20].

A further promising application for semiconductor nanocrystals is in low cost, high efficiency solar cells. Since 1985 the research group of Michael Grätzel have made considerable progress with dye-sensitized mesoscopic solar cells (DSCs) and have studied the use of colloidal QDs as alternative photoabsorbers to replace the dyes [21]. DSCs use molecules to absorb photons and convert them to electric charges without the need of intermolecular transport of electronic excitation [22]. They are stable, low cost cells with competitive efficiencies which provide a further step towards the acceptability of renewable energy technologies based on solar power. Of particular interest are QDs with an absorption range up to NIR that would enhance solar energy harvesting. Zaban et al. demonstrated photoelectrochemical solar cells based on photosensitization of TiO_2 electrodes with InP QDs [23]. The InP QDs were absorbed onto the TiO_2, extending its photoresponse over the visible and near-IR spectral region. Similar work was done by Plass et al. in which PbS QDs were used to sensitize TiO_2 leading to faster carrier recombination compared to dye-sensitized systems [24].

A first step towards nanocrystal quantum dot lasers was demonstrated by Klimov et al. in their studies of optical gain in CdSe colloidal QDs [25]. They observed narrowband stimulated emission, with a pronounced gain threshold, at wavelengths tunable with the size of the QD. This prompted much subsequent research to further understand the mechanisms and parameters that contribute to the performance of semiconductor nanocrystal lasers. The research has culminated in the development of core/shell 2D semiconductor nanocrystals. Work on these structures, such as colloidal nanoplatelets [26], have shown that high-energy carriers relax to the band edge on time scales much faster than recombination times, as needed for stimulated emission and lasing. As such, low amplified spontaneous emission (ASE) thresholds ($6\ \mu J/cm^2$) and high saturated gain ($600\ cm^{-1}$) have been measured in these systems, demonstrating the potential for turning colloidal nanocrystal lasers into a practical reality.

Electroluminescent devices based on nanoscale semiconductor materials have also been constructed. Colvin et al. made light emitting diodes from CdSe and a semiconducting polymer [27]. These devices realise all the advantages of bulk semiconductor diodes in a material that, by changing the nanocrystal size or the

operating voltage, is capable of producing different emission colours. Similar results were obtained a few months later by Dabbousi et al. in another CdSe QD/polymer composite [28]. A considerable improvement in the luminescent power efficiency was subsequently demonstrated by Coe et al. with a quantum dot LED device containing a single monolayer of CdSe(ZnS) QDs sandwiched between two organic thin films [29]. Companies like Sony and Samsung have exploited the tunable emission of QDs to convert light from blue LEDs into highly saturated, narrow band primary colours for their latest LCD TV screens.

1.2 Doped colloidal quantum dots

The incorporation of dopants into semiconductor lattices is widely used to control electrical properties of materials [30]. Furthermore, it has been shown to affect optical and magnetic properties [31]. In order to realize the potential of nanoscale semiconductor materials in future technologies, it is necessary to control and understand the effects of doping in these systems. In this respect, colloidal synthesis has an advantage over nanostructures formed by lithographic processing or by self-assembly, as it makes it possible to control doping levels of impurities, and enables the effective tuning of the distance between the impurities.

The ability to manipulate luminescent properties to produce high quantum yields, narrow emission line shapes or broadband excitation profiles has increased the potential of using magnetically doped nanomaterials in magnetic resonance imaging (MRI) applications [31]. It has been established that contrast enhancement is dependent on composition, size, surface properties and degree of aggregation of the nanocrystals [32]. Investigations into the relationship between these parameters and the contrast of relaxation times, of nuclei under the influence of the nanocrystals, have been studied along with the different approaches to integrating fluorescence with magnetic properties in the nanocrystals [32, 33].

In this work we aim to exploit both the magnetic and optical properties resulting from the incorporation of isolated impurities. As such, there are two categories of

doped semiconductors that are relevant to this work: dilute magnetic semiconductors (DMS), and semiconductors doped with luminescence activators.

1.2.1 Dilute magnetic semiconductors

Initial studies on DMS were driven by the observation of 'giant' Zeeman effects in the excitonic levels, suggesting possible magneto-optic applications [34]. The 'giant' Zeeman effect is a consequence of a strong exchange interaction between the *d*-electrons of the magnetic ions and the charge carriers of the QD. When a magnetic field is applied, the net alignment of the spin of the magnetic ions leads to the 'giant' Zeeman energy splitting of the free carriers. The resulting splitting is much larger than the 'regular' Zeeman splitting which is a result of the direct action of the magnetic field on the electron spin of the magnetic ions.

Recently, attention has turned to applying the properties of QDs in the field of spin-based electronics. Central to these applications, is the ability to manipulate local spins by *g*-factor engineering for which various approaches have been demonstrated. For example, Salis et al. used a $Al_xGa_{1-x}As$ quantum well in which the alloy composition, *x* was gradually varied through the structure [35]. It was shown that the application of an electric field leads to a displacement of the electron wavefunction. At different Al concentrations, different spin splitting was observed and therefore, different *g*-factors were probed as a function of the electric field. Doty et al. demonstrated a further example of electrically tunable *g*-factors on individual vertically stacked InAs/GaAs quantum dot pairs separated by thin tunnel barriers [36]. An electric field was used to tune the relative energy of the two QDs and a corresponding strong resonant increase or decrease in *g*-factors was observed. A somewhat different approach was taken by Nakaoka et al. who reported *g*-factor tuning through the strain engineering of self-assembled InGaAs QDs [37]. The strain was varied in two ways: by thermal annealing, which decreased both electron and hole *g*-factors, and also by introducing a strain reducing layer, which enhanced the electron and reduced the hole *g*-factors. More recently *g*-factor engineering has been achieved in nanoscale DMS systems. An example of this is the demonstration by Bussian et al. of a widely tunable magnetic *sp–d* exchange interaction between

excitons and dopant ions, using 'inverted' core–shell nanocrystals [38]. The nanocrystals were composed of Mn^{2+}-doped ZnSe cores overcoated with undoped shells of narrower-energy gap CdSe, and the effective exciton *g*-factors were tuned from -200 to +30 solely by increasing the shell thickness.

Techniques for tuning the *g*-factors of the carriers can be useful for tailoring material properties for different applications. For example, a high excitonic g-factor maximises the separation of spin states and as such can be used to reduce off-resonant laser coupling [39]. Whereas, a zero exciton *g*-factor is required to produce a magnetic field tunable, polarization insensitive photodetector [40], and also to use the exciton spin degree of freedom for QIP.

1.2.2 Incorporating Mn^{2+} in colloidal nanocrystals

Doping with Mn ions is of particular interest as they have interesting magnetic properties and can act as luminescence activators. Mn^{2+} ions are effective dopants due to their half-filled *d* orbitals which yields a maximum *sp-d* exchange interaction between single carriers or excitons with the transition metal ion [41]. This leads to correlated carrier and magnetic ion spins in individual QDs [42] and can be used as a means of probing and manipulating the spin state of the magnetic impurities.

A lot of work has been done in recent years by the Gamelin research group on Mn-doped II-VI semiconductor QDs, i.e. CdS [43], CdSe [44-47], ZnSe [48] and ZnO [49-53]. Much of the group's work has been done on ZnO:Mn which is unique among Mn^{2+}-based II-VI QDs because of its mid-gap $Mn^{2+/3+}$ level, which gives rise to a rich variety of unusual electronic and magnetic properties [51].

One of the biggest challenges to overcome with the incorporation of dopants into nanocrystals is quenching of the luminescence efficiency. In Mn-doped II-VI QDs an increase in Mn concentration leads to a reduction and subsequent quenching of the QD luminescence [54]. The Mn-impurity has an energy level at lower energies compared to the energy gap of II-VI QDs, allowing non-radiative redistribution of

photogenerated charges between the QD and the Mn-energy states, hence radiative recombination is observed from the lower energy Mn-level to the QD valance band. In particular, the Mn-related PL band is observed at E ~ 1.9 eV [18] compared to II-VI QD emission at E_{QD} > 1.9 eV and up to 3.7 eV [55]. However, in IV-VI QDs the E_{QD} = 1 eV to 1.4 eV [18] which is at lower energy compared to the position of Mn-energy level, hence the emission is observed at the energy corresponding to the QD energy gap. In our PbS:Mn QDs, the Mn-related PL emission in PbS is either not observed or is significantly weaker (~3 orders of magnitude) compared to the QD PL emission[18].

IV-VI-based nanomaterials are widely explored for NIR optoelectronics [56-58]. Bulk PbS has direct bandgap, Eg = 0.2586 eV at 4K and 0.41 eV at room temperature [59] and the effective mass of the free carriers is very small and approximately equal, $m_e^* \approx m_h^* \approx 0.09m_0$, where m_0 is the electron mass in vacuum. The combination of these parameters and a large Bohr radius, R_{ex} ~ 20 nm, result in strong carrier confinement in IV-VI QDs and enable tuning of the bandgap over a wide range of frequencies.

There are various factors that affect the doping of nanomaterials: impurity solubility, nanocrystal size, shape and surface morphology [60]. In particular, the large surface/volume ratio can result in the nanocrystals 'self-purification' such that the dopants diffuse out of the core to the surface of the nanocrystals (Figure 1-2) [61]. It is important to determine the position of the impurity in the crystal lattice of the QD. Isheim et al. studied Mn dopants in PbS nanowires [62] and suggested strong preference for Mn-ions to occupy lattice sites of the Pb sublattice. Mn^{2+} ions act neither as donors nor as acceptors in Pb salts if Mn^{2+} substitutes Pb^{2+} and thus will not affect the carrier type and concentration in the QD core.

In order to establish the effect of tuning the strength of carrier confinement and magnetic doping concentration on the emission energy, Prado et al. compared electronic properties of QDs of two IV-VI semiconductor materials by modifying the quantum confinement from spherical to semispherical and varying the diluted concentration of incorporated Mn^{2+} ions [63]. The change in confinement resulted

in changes in the magnetic energy dispersions and the incorporation of magnetic ions in IV–VI QDs strongly modified the QD interband absorption spectra.

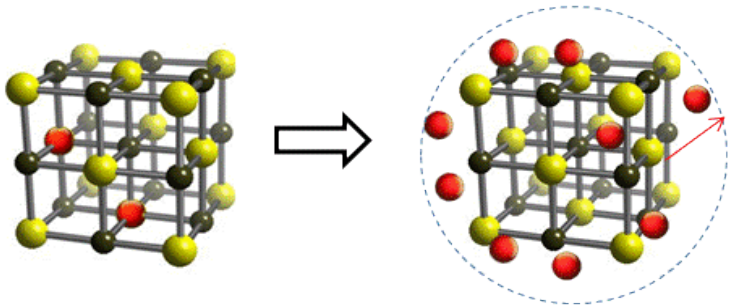

Figure 1-3 Self-purification process for a doped lead-salt structured nanocrystal.

Further examples of research on Mn-doped lead chalcogenide QDs are scarce. The few exceptions include the first synthesis of Mn-doped PbSe nanocrystals performed by Ji et al. in 2003 [64], evidence of successful growth of Mn^{2+}-doped PbS and PbSe nanocrystals embedded in a glass matrix reported by Silva et al. [65, 66] and the work done by Long et al. who studied carrier-dopant exchange interactions in Mn doped PbS synthesized in organic solvents [67].

1.3 Material systems for quantum information processing

Possibly the greatest potential future market for semiconductor nanocrystals is in the area of quantum information processing (QIP). It is expected that quantum computers will have far greater computational power than classical ones. Development of quantum computing would also enable quantum cryptography which allows for absolute secrecy of communication between two parties [68]. A considerable body of work is presently underway to create physical computing devices that operate in the quantum mechanical regime. There is a vast variety of approaches to QIP, proposed theoretically and explored experimentally, covering virtually every branch of quantum physics.

1.3.1 Quantum information processing

In the paper, '*The Physical Implementation of Quantum Computation'* [69] David P. DiVincenzo outlined five requirements for the implementation of quantum computation:

i. A scalable physical system with well characterized qubits

A physical system which comprises a collection of qubits is the most basic requirement for implementing quantum computation. In order to obtain long coherence times necessary for QIP, the qubits must be completely isolated from the outside world. However, isolation and control becomes much more difficult as more qubits are added into the computer. As such, finding an appropriate, scalable physical system presents a considerable challenge.

A qubit is a quantum two-level system such as the spin-up and spin-down state of a spin ½ particle. Whereas the bit is the fundamental unit in classical information the qubit is the fundamental unit of quantum information, i.e. it represents the simplest quantum system. The quantum state of a qubit is a vector in a two dimensional complex space. The computational basis states of a qubit are $|1\rangle$ and $|0\rangle$, and the general quantum state is the linear combination, or superposition, of these basis states:

$$|\psi\rangle = \alpha|0\rangle + \beta|1\rangle, \tag{1.2}$$

where α and β are amplitudes with the normalization constraint:

$$|\alpha|^2 + |\beta|^2 = 1, \tag{1.3}$$

i.e. the length of the state vector is equal to 1 (it is a unit or normalized vector).

Taking the normalization constraint into account, Equation 1.2 can be rewritten in spherical polar coordinates as:

$$|\psi\rangle = cos\frac{\theta}{2}|0\rangle + e^{i\varphi}sin\frac{\theta}{2}|1\rangle. \tag{1.4}$$

The numbers θ and φ define a point on the unit three-dimensional sphere, known as the Bloch sphere (Figure 1-3). The Bloch sphere is particularly useful as it

corresponds with the classical picture of magnetic resonance experiments, and as such it is possible to imagine mw pulses rotating the spins to different points on the sphere. It is limited however, as it can only depict the general quantum state of a single qubit. The general quantum state of two qubits is a four dimensional vector with one dimension for each distinguishable state of the two systems,

$$a|00\rangle + b|01\rangle + c|10\rangle + d|11\rangle. \tag{1.5}$$

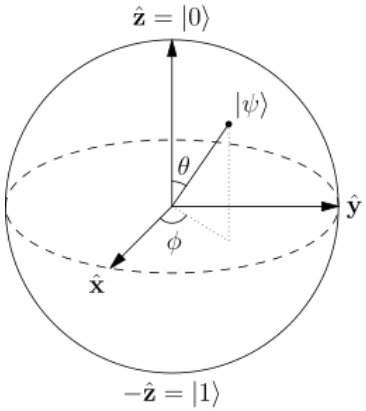

Figure 1-4 The Bloch sphere represents the superposition of the basis of states,$|1\rangle$ and $|0\rangle$, of a qubit.

For a qubit to be 'well characterized' its physical parameters should be accurately known. As well as the presence of, and coupling to other states of the qubit, the interactions with other qubits and couplings to external fields may be used to manipulate its state. Also, if the qubit has more than two states the probability of the system going into one of these other states should be small.

ii. The ability to initialize the state of the qubits to a simple fiducial state, such as $|000\ldots.\rangle$

This describes the requirement that qubits should be initialized to a known value prior to computation. A possible solution would be to use resonant optical excitation of one of the exciton levels of a magnetically doped QD. By optically pumping in this way it is possible to initialize the state of a spin qubit [70].

iii. Long relevant decoherence times, much longer than the gate operation time

In the case of ESR the 'relevant' decoherence time is the phase memory time, T_M. The processes that affect T_M are spin-spin relaxation (characterized by T_2), spectral diffusion, spin diffusion and instantaneous diffusion. The upper limit of T_M is the spin-lattice relaxation constant, T_1, which characterises the interactions between the electron spins and the surrounding lattice. The length of the decoherence time is less important than the ratio of the decoherence time to the gate operation time, or 'clock time'. The clock time is determined by the Rabi oscillation period for which the figure of merit, Q_M, indicates the potential number of quantum logic operations that can be executed before coherence is lost.

iv. A 'universal' set of quantum gates

It is necessary to have a set of quantum gates from which any function can be computed. In ESR, a single qubit gate involves using mw pulses to rotate the qubit from one point on the Bloch sphere (Figure 1-3) to another point. Varying the power and duration of the pulses determines the amount of rotation, and changing the phase determines the rotation axes; as such, any point on the Bloch sphere can be accessed with either a single pulse or a sequence of pulses around the *x* and *y* axes.

In order to obtain a universal set of quantum gates it is necessary to combine the single qubit gates with a controlled-NOT (CNOT) gate. This is a two bit gate involving a control bit and a target bit – for example, if the control bit is $|1\rangle$ the target bit is flipped, and if the control bit is $|0\rangle$ the target bit is left unchanged, i.e. $|1\rangle|0\rangle \rightarrow |1\rangle|1\rangle$ and $|0\rangle|1\rangle \rightarrow |0\rangle|1\rangle$ where the first term is the control bit.

v. A qubit-specific measurement capability

It is necessary to have a means of reading out the state of the qubit. In a semiconductor the spin state of a magnetic dopant is coupled to the exciton spin state. This provides an opportunity to read out the state of the qubit using PL as a probe, and was demonstrated by Besombes et al. for a single Mn atom in a CdTe/ZnTe QD [71].

1.3.2 Sources of spin decoherence

Significant progress has been made in the use of magnetically doped semiconductors to control quantum states and to probe the mechanisms of spin decoherence. In 2006 Tyryshkin et al. [72] reported measurements of long coherence times at 7 K in P-doped bulk Si. Spin relaxation experiments were carried out with natural Si and ^{28}Si-purified silicon. The presence of ^{29}Si magnetic nuclei in natural Si was found to decohere the electron spin in less than 0.5 ms. However, much longer transverse relaxation times of T_2 = 60 ms were observed in the isotropically pure ^{28}Si.

The use of phosphorus (P) as a dopant has been shown to give the longest transverse relaxation times in isotopically pure ^{28}Si [73, 74]. However, bismuth (Bi) is in the same group as phosphorus and shares some of the advantages such as long coherence times. Furthermore, the use of bismuth as a dopant permits additional possibilities. A very large hyperfine coupling, in combination with the large nuclear spin of I = 9/2, allows for working in the hybrid nuclear–electronic regime. Morley et al [75] used bismuth-doped silicon to demonstrate the quantum control of the electronic and nuclear spin states in 'hybrid nuclear–electronic' qubits. They observed coherence times up to T_2 = 4 ms, that is five orders of magnitude longer than the manipulation times, and is limited only by naturally occurring ^{29}Si nuclear spin impurities. Coherent control of the hybrid nuclear-electronic transitions was demonstrated with Rabi oscillations at 8 K. This hybrid regime produces long coherence times with quantum control of more than two orders of magnitude faster than in pure nuclear states.

However, the long relaxation times, observed in ^{28}Si:P and ^{28}Si:Bi, decrease rapidly with increasing temperature. Bader et al. measured relaxation times in 1Ni:1Cu molecular nanomagnets in which a decoherence time of T_M = 1 μs was observed up to room temperature and long T_M = 68 μs was observed at 7 K [76]. These long relaxation times were attributed to the rigidity of the lattice, thus diminishing the limiting effects of spin-lattice relaxation, and also to the removal of nuclear spins from the vicinity of the magnetic ions.

A somewhat different system in which long decoherence times are also observed up to room temperature is diamond nitrogen vacancy (NV) centres, $T_2 = 58\,\mu s$ at 300 K [77]. The NV centre is a point defect in the diamond lattice formed when two C atoms are replaced by a nitrogen atom and a vacant site. Takahashi et al. attributed the primary source of decoherence in diamond to the N spin bath fluctuations. It was demonstrated that by decreasing the temperature, the spin bath is polarized and decoherence is quenched, T_2 ~ 250 μs at 2 K [78].

The ability to optimize spin properties by engineering the structure of the material is one of the main advantages offered by colloidal QDs. An example of how this flexibility can be exploited is demonstrated by Schimpf et al. [79], where T_1 and T_2 in Mn-doped colloidal QDs was increased via surface (or ligand) deuteration, (from T_1 = 48 μs to 80 μs and from T_2 = 581 ns to 760 ns) which lowers the relevant Larmor frequency, or by shell growth (T_1 = 0.7 ms to 2.0 ms and T_M = 2.1 μs to 4.7 μs) which reduces the dipolar coupling between Mn spins and external nuclear spins.

1.3.3 Exciton-spin interactions

The interaction between the exciton and the magnetic ions in QDs can be exploited to manipulate the quantum state of an individual spin [80]. The size and shape of the QDs strongly influence the strength of exciton confinement in QDs, and can be used as a tool for engineering of the exciton *g*-factor [81], as discussed in Chapter 1.2.1.

In 2008, Beaulac et al. [82] reported the successful synthesis of colloidal CdSe QDs doped with Mn^{2+}. This led to the emergence of properties including spin-polarizable excitonic photoluminescence (PL), magnetic circular dichroism, exciton storage, and excitonic magnetic polaron formation. It was reported that the properties of CdSe:Mn with diameter, $d \approx 2.5$ nm, are similar to those of Mn^{2+}-doped ZnS, ZnSe, or CdS nanocrystals [46], showing Mn^{2+} PL with long exciton lifetime. At intermediate sizes, $d \approx 3.3$ nm, thermal equilibrium between excitonic and Mn^{2+} excited states leads to long excitonic PL decay times at elevated temperatures [45], (τ = 15 μs at 200 K), exceeding the decay times of undoped CdSe by ~ 10^3. At large

sizes, $d \approx 4.2$ nm, all Mn^{2+} states reside outside the band gap, and the nanocrystals show excitonic PL that coexists with strong dopant-exciton magnetic exchange coupling, leading to the first demonstration of spin-polarizable exitonic PL in any colloidal doped QD [47].

The interaction between excitons and magnetic ions in QDs is of particular interest for readout and initialization of qubits. Besombes et al. demonstrated how the spin state of Mn incorporated into II-VI QDs could be read using a PL spectrum [71]. When a Mn atom is incorporated into a II-VI QD, the spin of an optically created electron-hole pair interacts with the five *d*-electrons of the Mn. This leads to splitting of the PL spectrum into six ($2I$+1) components. The spin state of the Mn-ions fluctuates during optical measurements, and as such, the six lines are observed simultaneously in the time averaged PL spectra. The intensities of the lines reflect the probability for the Mn to be in one of its six spin components. Thus, PL can be used to probe the spin state of Mn, providing a means of reading out the result of quantum computations.

A technique for initializing spin states by means of optical pumping was reported by Le Gall et al. [70] and was demonstrated for QDs grown by molecular beam epitaxy (MBE) on a ZnTe substrate and doped with individual Mn atoms. The confined carriers and Mn spins become strongly mixed in these systems such that the resonant optical excitation of the QD affects the spin state of the Mn electrons [5]. It is possible to exploit this phenomenon by optically exciting one of the six exciton levels in order to initialize the spin state of an embedded Mn ion. A pumping efficiency of about 75 % with an initialization time in the tens of nanoseconds range was achieved [70].

1.3.4 Microcavities

Incorporating QDs into microcavities could provide the benefits of a rigid structure, and could be used to optimise decoherence times and enhance interaction of the spin qubit with light.

Microcavities consist of a cavity with diameter of about half the wavelength of the QD emission, surrounded by distributed Bragg reflectors (DBR). DBRs are composed of repeating regions of high and low refractive index. Increasing the refractive contrast of the layers increases the reflectivity, *R* [83],

$$R = \frac{n_2^{2N} - n_1^{2N}}{n_2^{2N} + n_1^{2N}} \ , \tag{1.6}$$

where n_1 and n_2 are the alternating refractive indices, *N* is the number of repeating pairs and it is assumed that the light originates and terminates in vacuum. Light incident on the DBRs, with periodic spacing, is partially reflected at each layer interface resulting in constructive interference of the light wave [84]. Wavelengths that are able to propagate through the structure define the cavity mode and groups of modes form bands. The wavelength of the cavity mode is defined by the dimensions of the structure as well as temperature. When a QD is incorporated into the cavity, enhancement of stimulated PL emission is achieved by matching the wavelength of the cavity mode with that of the QD emission. The Purcell Effect quantifies the enhancement of spontaneous emission rates in a resonant cavity and is proportional to the quality factor, *Q*, which defines the ratio between the energy stored in the cavity, at the resonant frequency, with the power dissipated.

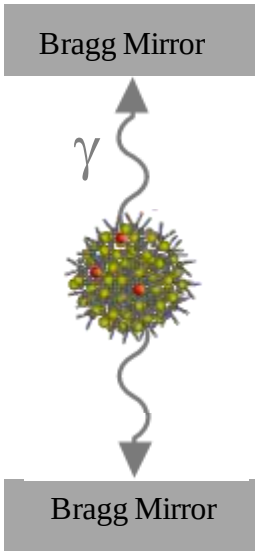

1-5 Diagram illustrating the principle of a micropillar cavity

The simplest type of optical microcavity is the micropillar (or micropost) cavity (Figure 1-5). Various techniques have been used to fabricate these structures and combine them with QDs. For example, DBRs have been constructed by spin coating alternating polymer layers (poly-vinylcarbazole (PVK) and poly-acrylic acid (PAA)) with high and low refractive indices [85]. In between the DBRs was sandwiched a PVK defect layer, doped with a single QD which defined the 1D cavity. This process is compatible with the standard solution processing technique of colloidal QDs and produces a PL signal with $Q \sim 30$.

A further example of a simple, low cost microcavity was demonstrated by Goldberg et al. using a combination of Plasma Enhanced Chemical Vapour Deposition (PECVD) and dip coating [86]. Alternating Si_3N_4 and SiO_2 DBRs were first fabricated using PECVD, then CdSe/ZnS (core/shell) QDs in a toluene solution were deposited by dip coating the lower DBR. The PL spectrum showed a factor of 3 increase in Q ($Q \sim 60$) and a Purcell factor ~ 1.3.

In order to improve the control of the wavelength of the cavity mode and decrease the stress of the active layer, Martirandonna et al. used a hot embossing technique to assemble a 'mold' over the active layer and lower DBR of their microcavity structure [87]. A factor of 10 increase in Q was measured ($Q \sim 146$) with the structure which consisted of CdSe/ZnS core/shell colloidal QDs in PMMA deposited by spin-coating and sandwiched between TiO_2/SiO_2 DBRs prepared by e-beam evaporation.

A similar structure was fabricated by Kahl et al. using magnetron sputtering with a spin coated active layer [88]. In order to improve performance, pillar microcavity structures were milled into the planar cavity with a focused ion beam (FIB). The emitted photons were shown to exhibit 3D confinement due to laterally guided modes producing a significantly improved $Q \sim 10000$.

A lattice of holes in a material of high refractive index, or alternatively a lattice of columns, provides the periodic refractive contrast necessary for Bragg reflection. The cavity can be incorporated into this photonic crystal by engineering a defect into the lattice. An example of a 3D photonic crystal is the 'inverted template assisted

self-assembled structure' [89, 90]. In order to fabricate these structures colloidal crystals were grown by sedimentation of nanoscale polystyrene (PS) latex spheres suspended in water. The suspension was then dried to form an artificial opal. After dissolving the PS spheres this titania inverse opal photonic crystal was soaked in a ZnSe-coated CdSe colloidal QD solution to allow the nanocrystals to infiltrate the structure. An enhancement of up to a factor of 5 was achieved using this approach [89].

A similar principle can be applied to a 2D photonic crystal. Wu et al. fabricated a Si membrane atop a SiO_2 membrane [91-93]. An etch mask was first fabricated by electron beam lithography and was used to produce a triangular lattice of holes in the Si membrane by electron-cyclotron resonance (ECR) etching. Soaking of the structure in a PbSe QD solution for ~10 hours resulted in a photonic crystal with Q ~ 775 and a Purcell factor ~ 35.

Despite many examples of microcavities, as well as the success in achieving long decoherence times in magnetically doped semiconductors, and also the progress made in the optical manipulation of electron spins, there is still a lack of understanding of the limiting factors and mechanisms affecting T_M in these systems. Understanding these mechanisms is an important prerequisite to future utilization of QDs in quantum technologies.

Chapter 2

Experimental Techniques

The experiments used in this thesis cover a diverse range of techniques. This chapter briefly describes the methods used for the synthesis and morphological characterisation of the nanocrystals, and provides details of the various magnetic resonance experiments that form the focus of the thesis. Experimental procedures used for the optical studies are also included.

The work was carried out at The University of Nottingham and the National EPR Research Facility at the University of Manchester.

2.1 Colloidal growth

Mn-doped PbS QDs were synthesised by Dr L. Turyanska, modifying the method described by Levina et al. [94]. The samples were prepared using thioglycerol (TGL) and dithioglycerol (DTG) as capping agents. These are small (~0.5 nm) organic compounds with functional groups of –SH (TGL) and –OH (DTG). The strong affinity of Pb^{2+} and S^{-} lead to the formation of bonds and results in passivation of the nanocrystal surface.

The nanoparticles were synthesised by preparing a Pb^{2+} precursor solution containing 2.4×10^{-4}mol of lead acetate $Pb(CH_3COO)_2$, 1.5×10^{-3}mol of TGL and 5×10^{-4}mol of DTG in 15 ml of deionized water. Triethylamine was then added in order to adjust the pH to a value of 11.0 and, while maintaining the pH, manganese acetate $Mn(CH_3COO)_2$ was added. In order to facilitate the incorporation of the Mn-atoms during the nucleation stage of the nanocrystals growth, a 0.1 mol solution of sodium sulphide Na_2S was slowly added at a molar ratio MR = 1:0.3 of Pb(Mn) to S. The samples were synthesised and stored under N_2 atmosphere to prevent oxidation and sedimentation [18].

2.2 Morphological characterization

The structure of the nanocrystals was determined using high resolution transmission electron microscopy (HRTEM) and atomic force microscopy (AFM). Size distribution profiles were obtained from analysis of the AFM images, and the incorporation of Mn in the nanocrystals was assessed by energy-dispersive X-ray (EDX) spectroscopy.

For the HRTEM study, the nanoparticles were deposited on a lacey-carbon coated Cu grid or a graphene oxide-coated grid, and images were recorded by Dr. M. W. Fay (Nottingham Nanotechnology and Nanoscience Centre) on the JEOL1200EX and JEOL2100F microscopes operating at 120 kV. HRTEM, or phase contrast TEM, provides a means of imaging the atomic structure of a sample. The technique uses a magnetic field to focus a beam of electrons through a thin sample. The final image is formed by the interference between the direct beam and the diffracted beams and is detected by a charge-coupled device (CCD) camera [95]. A resolution of < 0.01 nm [96] is achieved due to the small de Broglie wavelength of the electron.

EDX spectra and maps were recorded with an Oxford Instrument ultrathin-window EDX detector. This spectroscopic technique uses a focused electron beam to excite an electron in the sample and eject it from an inner shell. The subsequent hole is

then filled by an electron from a higher energy shell, and an X-ray is emitted with energy equal to the difference between the two shells. In this way it is possible to produce an X-ray spectrum characteristic of the elements comprising the sample [97].

For the AFM studies, the nanoparticles were spin-coated onto Si substrates. The cantilever has a ~20 nm tip which is used to probe the morphology of the sample. The movement of the cantilever over the sample is controlled by a piezoelectric transducer and a laser, focused to the tip, is reflected off the back of the cantilever into a detector. As the cantilever is displaced via interaction with the surface, the laser beam is also displaced. This displacement is detected and an image of the structure of the surface is reconstructed [98].

2.3 Electron Spin Resonance

Electron spin resonance (ESR) can be used to analyse systems containing paramagnetic ions. ESR experiments can be divided into two categories: continuous wave (CW) and pulsed. CW ESR allows identification of the paramagnetic species in a sample, to determine the various spin Hamiltonian parameters and to characterize the local environment [99]. Pulse ESR is used to investigate the spin dynamics of the sample [100]. Of particular interest are investigations of the Zeeman effect, the hyperfine interaction, the zero-field splitting, and the study of relaxation times, in particular the phase memory time, T_M.

The most commonly used spectrometer for ESR studies is X-band (9.5 GHz). There can, however, be advantages in using high frequency mw radiation. The high magnetic field means there is a greater alignment and stability of spins giving an increased resolution of the $\boldsymbol{g}$ tensors and the Larmor frequency, i.e. the frequency with which the net magnetization precesses around the axis of the external field. The higher frequency at W-band is beneficial for probing time-resolved molecular dynamics, and is particularly useful for relaxation time studies and also for resolving hyperfine structure otherwise unresolved at lower frequency. In this work we used

X-band (~9.5 GHz), K-band (~24 GHz), Q-band (~35 GHz) and W-band (~95 GHz) spectrometers. K-band CW experiments were performed on an EMX spectrometer with a 1.8 T electromagnet and CW/pulsed X- and Q-band experiments were performed on a Bruker Elexsys E580 with a 1.8 T electromagnet (National EPR facility and service, University of Manchester) at temperatures ranging from T = 5 K to T = 300 K. Low temperature W-band CW experiments were performed on a home-built spectrometer based on a Krymov bridge and probe (SPMMRC, University of Nottingham) [101].

2.3.1 Continuous Wave ESR

In this work CW ESR spectra were measured and simulated in order to determine spin Hamiltonian parameters and consequently assist us in the characterization of the local environment of the QDs.

When a paramagnetic sample is placed in a magnetic field, the degeneracy of the unpaired electron is lifted as described by the spin Hamiltonian,

$$\mathcal{H} = g\mu_B \boldsymbol{S} \cdot \boldsymbol{B}, \tag{2.1}$$

where g is the g-factor, μ_B is the Bohr magneton, $\boldsymbol{B}$ is the magnetic field and $\boldsymbol{S}$ is the spin angular momentum operator. As the degeneracy is lifted, two spin states, $m_s = \pm 1/2$, are created. The energy difference between these states increases with an increasing magnetic field and the sample will absorb mw radiation when the following resonance condition is satisfied,

$$\Delta E = h\nu = g\mu_B B_r, \tag{2.2}$$

where ν is the mw frequency and B_r is defined as the resonant field.

The hyperfine interaction is a result of the coupling of the electron magnetic moment to the magnetic moment of surrounding nuclei. This perturbation in the electron energy leads to another term in the spin Hamiltonian,

$$\mathcal{H} = \boldsymbol{S} \cdot \boldsymbol{A} \cdot \boldsymbol{I}, \tag{2.3}$$

where ***A*** is the hyperfine coupling constant and ***I*** and ***S*** are the nuclear and electron spins respectively. Figure 2-1 shows how the nuclear magnetic moment can add energy to, or subtract energy from, the electron magnetic moment depending whether they are aligned parallel or anti-parallel.

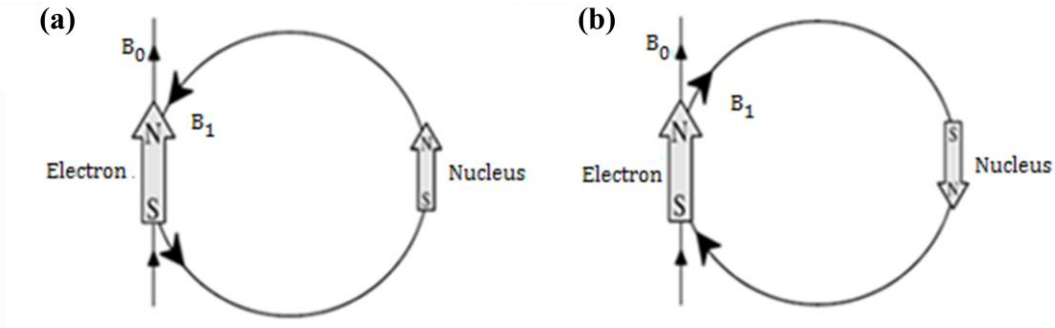

Figure 2-1 Scheme of the hyperfine interaction between unpaired electron spins and the surrounding nuclear spins. The nuclear magnetic moment can add (a) and reduce (b) the overall magnetic field.

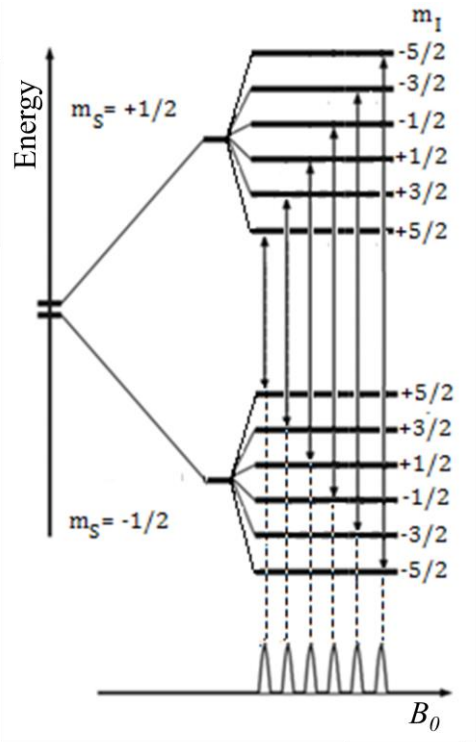

Figure 2-2 Splitting of the $m_s = \pm 1/2$ states due to $I = 5/2$ showing the transitions resulting from hyperfine interactions ($\Delta m_S = \pm 1, \Delta m_I = 0$). Lower inset presents absorption spectrum of $2I+1$ lines, where the distance between the peaks defines the hyperfine coupling, A.

The hyperfine coupling constant A is defined by the distance between the lines in the absorption spectrum (Figure 2-2) and gives information about the local environment such as the identity and number of atoms surrounding the unpaired electron and the distance between these atoms and unpaired electrons. The diagram shows an $I = 5/2$ system giving $2I+1$ peaks in the absorption spectrum.

Zero field splitting lifts the degeneracy of the m_s states and is independent of a magnetic field. It can be expressed as

$$\mathcal{H} = \boldsymbol{S} \cdot \boldsymbol{D} \cdot \boldsymbol{S}, \tag{2.4}$$

where the $\boldsymbol{D}$ tensor describes axial symmetry ($D = 0$ for cubic symmetry). The term describes the distortion of the crystal field symmetry and originates from the dipolar spin-spin interaction and the spin orbit coupling. The dipolar interaction describes the effect of each unpaired electron's magnetic field on another unpaired electron's magnetic field, i.e. two electrons with their spins aligned parallel to one another experience a repulsive interaction. The spin orbit coupling describes the interaction between the electron's spin and the magnetic field generated by the electron's orbit around the nucleus.

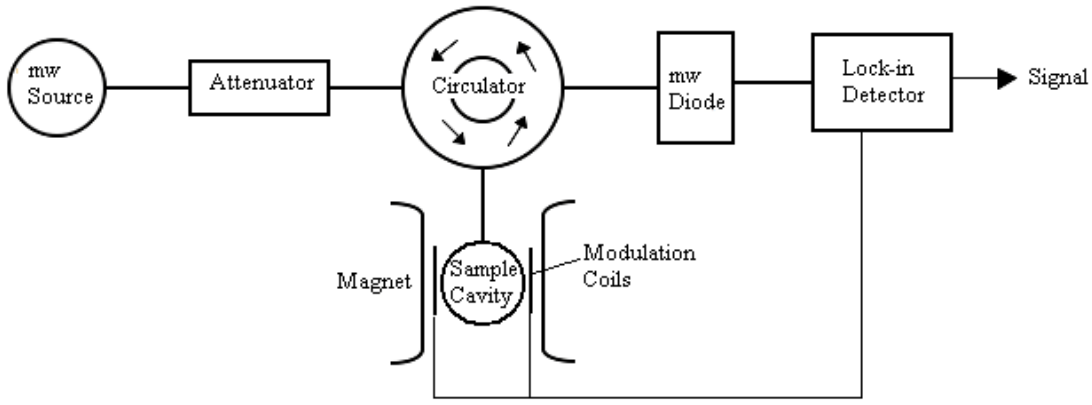

Figure 2-3 Simplified scheme of a CW ESR spectrometer.

Figure 2-3 shows the main components of a CW ESR spectrometer. Most ESR experiments use a resonant cavity, i.e. a box or cylinder that, at resonance, can support a standing wave. The mws are coupled to the cavity via the iris. By adjusting the size of the iris the cavity is tuned by matching its impedance to the impedance of the waveguide. When critically coupled, all energy incident on the

cavity is absorbed. In the CW ESR experiment, the frequency is held constant and the magnetic field is swept. At resonance, the spins realign which changes the magnetic susceptibility, which in turn changes the impedance, and causes power to be reflected producing the ESR signal via the lock-in detector.

Parameters were determined by simulating CW spectra with *EasySpin* [102]. This allowed us to determine the hyperfine coupling, zero-field splitting, *g*-values and linewidths.

2.3.2 Pulse ESR

Pulse ESR works on the same principle as CW ESR but instead of continuous irradiation of the sample a pulse forming unit allows the user to define sequences of pulses.

Figure 2-4 shows the standard spin echo pulse sequence which was used in most of the pulse ESR experiments described in this thesis. The first pulse flips the spins into the transverse plane and the spins begin to dephase in time, τ. They are then refocused by the second pulse leading to an echo at time, 2τ.

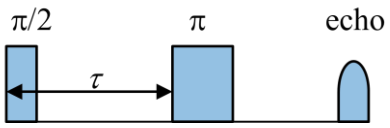

Figure 2-4 Spin echo sequence.

By measuring a series of spin echoes whilst incrementally changing the magnetic field, an echo field swept (EFS) spectrum is recorded. Echo intensity is plotted against magnetic field giving a spectrum analogous to a CW absorption spectrum. An EFS spectrum was recorded prior to all pulsed experiments in order to establish at which points in the field resonances are observed. Measurements were then performed with a fixed B_0-field corresponding to a particular hyperfine peak.

In order to determine how long coherence can be maintained, a spin echo decay (SED) experiment was performed. The SED experiment consists of a set of standard spin echo sequences (Figure 2-4) with the time between pulses incrementally increased. As a result of increased dephasing, the echo exponentially decays as a function of τ. The decay constant, T_M, can be fitted to the function:

$$I(2\tau) = I(0)\exp\left[\left(-\frac{2\tau}{T_M}\right)^s\right], \tag{2.5}$$

Where *s* is a stretching parameter.

The spin-lattice relaxation time, T_1, can be determined using an inversion recovery experiment. The pulse sequence used is shown in Figure 2-5a. The initial pulse inverts the spins, and is followed by a spin echo sequence after a time, *t*. The echo intensity is then plotted against the variable *t* and T_1 can be derived from the biexponential function:

$$I(t) = I_1\exp\left(-\frac{t}{T_1}\right) + I_{SD}\exp\left(-\frac{t}{T_{SD}}\right), \tag{2.6}$$

where I_1 and I_{SD} are amplitudes, and T_{SD} is the spectral diffusion time constant.

Figure 2-5b shows the pulse sequence for a nutation experiment. This experiment is used to establish the nutation (Rabi) frequency (Ω_R) and subsequently the potential number of quantum logic operations, as expressed by the figure of merit [103],

$$Q_M = \Omega_R T_M/\pi. \tag{2.8}$$

The initial pulse duration is incrementally increased leading to electron spin oscillations and the subsequent fast Fourier transform of these oscillations produces the power dependent nutation frequency peaks.

Various techniques can be used to identify and characterize nuclear interactions with the electron spin. The techniques used in this work are electron spin echo envelope modulation (ESEEM), and electron-nuclear double resonance (ENDOR). ESEEM is a technique for detecting nuclear frequencies in the low-frequency range (<100 MHz). The decay curve in the SED experiment is modulated due to the presence of magnetic nuclei in the vicinity of the electron spin. The modulation is a

result of oscillations between allowed and forbidden electron coherences or by the evolution of nuclear coherences. By subtracting a stretched exponential fit from the decay curve, the modulation can be isolated. The Fourier transform of the modulation allows the identification of the nuclear frequencies responsible for the modulation.

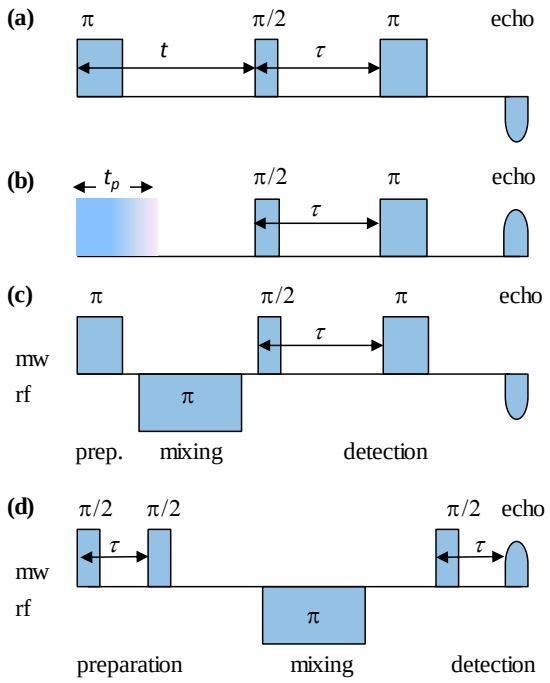

Figure 2-5 Spin echo sequences used for pulse ESR: (a) Inversion recovery sequence, (b) Nutation pulse sequence, (c) Davies ENDOR pulse sequence, (d) Mims ENDOR pulse sequence.

ENDOR is a polarization transfer ESR technique. The technique utilizes the much larger magnetic moment of the electron to detect NMR transitions that may otherwise be impossible to detect due to the nearby electron spin. ENDOR enables characterization of the hyperfine interactions between the unpaired electron and nearby nuclei.

The pulse sequences used for ENDOR experiments consist of preparation, mixing and detection periods (Figure 2-5c,d). During the preparation period one or more mw pulses invert the electron spin population. The mixing period consists of an *rf* pulse in which the frequency is incrementally increased in each subsequent

sequence. When the *rf* is on resonant with an NMR transition the magnetization is transferred to the other ESR transition and the change in electron spin population is recorded during the detection period.

The most commonly used ENDOR pulse sequences were developed by Davies [104] and Mims [105]. The two ENDOR techniques can be complementary. Davies ENDOR (Figure 2-5c) uses selective pulses and is more effective with strongly coupled nuclei. Mims ENDOR (Figure 2-5d) uses a stimulated echo with non-selective pulses and is more effective with weakly coupled nuclei.

2.3.3 Longitudinally detected (LOD) ESR

Traditional techniques in ESR use the same 'antenna' for transmitting high power excitation, as well as for detection of the very small magnetic fields produced by precessing spins. As such it is necessary to have a period of deadtime prior to detection. An alternative approach, which doesn't have this limitation and therefore is particularly useful for measurements in fast relaxing species, is LOD ESR, which detects the *z*-component of the electron magnetization [106]. This approach naturally has somewhat different hardware requirements. With LOD, a voltage induced by a change of the M_z magnetization is measured,

$$V_{ind} \propto -nA(dM_z(t)/dt). \tag{2.9}$$

The signal is detected by a pick-up coil oriented parallel to the polarizing magnetic field B_0, where n is the number of turns of the detection coil and A is its cross section. The coil is integrated into a serial *LCR* circuit, and the detected signal is the voltage, V across the capacitor, C (Figure 2-6).

A probe was designed and built to be operated on a W-band home-built spectrometer [101] and the effectiveness of the detection and shielding coils were assessed with bench top tests.

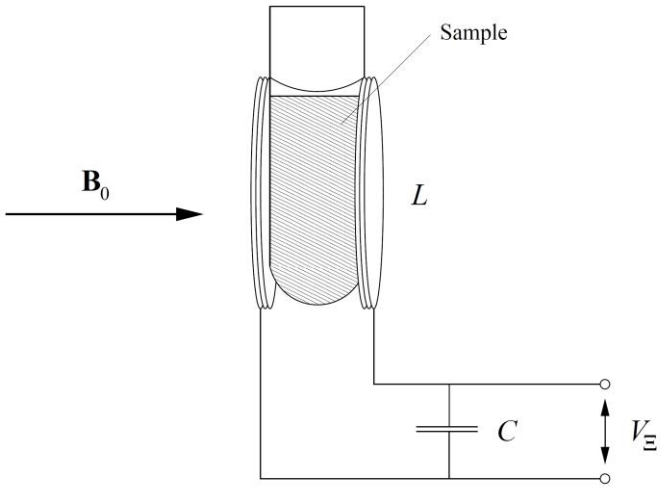

Figure 2-6 Experimental set-up for LOD ESR. A pick-up coil, oriented parallel to B_0, is integrated into a serial *LCR* circuit, and the detected signal is the voltage, *V*, across the capacitor, *C* [107].

2.4 Nuclear Magnetic Resonance

The principle of nuclear magnetic resonance (NMR) is similar to ESR, except that instead of measuring the interaction of unpaired electrons with an external magnetic field it is concerned with the interaction of nuclei with an external field. The degeneracy of the nuclear spin states is lifted on application of the magnetic field resulting in two spin states separated by an energy,

$$\Delta E = \gamma \hbar B_0 \tag{2.10}$$

where γ is the gyromagnetic ratio, B_0 is the external magnetic field. ΔE generally corresponds to frequencies in the *rf* range.

The NMR data, in this work, were collected by Dr Huw Williams and Dr Fabrizio Moro at 600 MHz on a Bruker Avance III spectrometer at 600 MHz and at a temperature of 298 K. Solvent suppression was achieved using excitation sculpting, where required. Spin lattice relaxation time experiments were conducted with an inversion recovery sequence (Figure 2-7). Data were acquired as a pseudo 2D spectrum and the relaxation delay was set at > 5 T_1 to facilitate complete recovery

between transients. Data were phased and baseline corrected prior to integration using TOPSPIN 3 software.

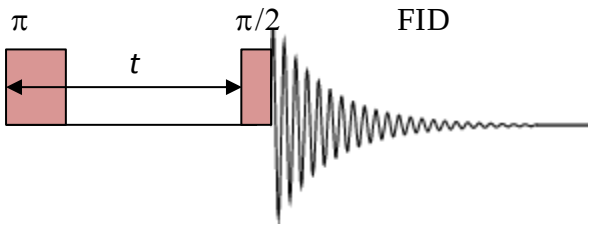

Figure 2-7 NMR inversion recovery sequence

2.5 Optical Studies

The optical studies include photoluminescence (PL) measurements to characterize the QDs and the fabrication of photonic crystals using two-photon polymerization (2PP) micromachining.

PL is used to probe the optical properties of semiconductors. Using this technique it is possible to determine the dependence of the band gap energy on QD size and composition.

Figure 2-8 shows a schematic diagram of the PL mechanism in a direct band gap bulk semiconductor. Semiconductors have a fully occupied valence band and an unoccupied conduction band that are separated by the band gap energy, $E_{g.}$ Electrons in the valence band can be excited into the conduction band following the absorption of photons, where the energy of the photons, $h\nu > E_g$. This process is followed by carrier relaxation where the excited electron and corresponding hole relax via phonons (quantised lattice vibrations) to the conduction band minimum and valence band maximum, respectively. This process occurs much faster than recombination, ensuring that when the carriers do subsequently recombine, they do so at an energy

equivalent to E_g. A similar process occurs in QDs, where carriers relax to the lowest discrete energy levels, prior to emitting a photon of energy, E_{QD} [108].

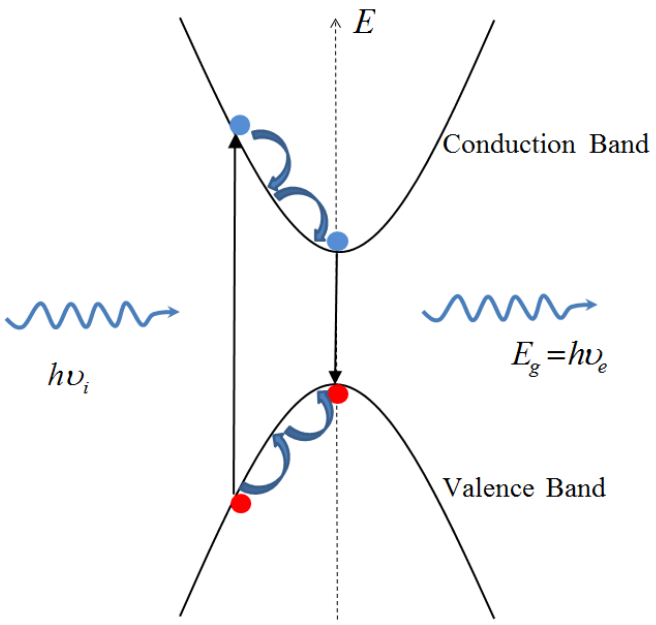

Figure 2-8 Schematic diagram of the PL mechanism in a direct band gap bulk

A Horiba Jobin Yvon Ltd. (HR800) Lab Ram set-up was used for the micro-PL studies (Figure 2-9). The samples are prepared by drop-casting the QD solution onto a glass substrate and allowing them to dry. Optical excitation is performed with a He-Ne laser (λ = 633 nm), or a Nd:YVO4 laser (λ = 532 nm). The He-Ne laser provides a power to the sample of up to 14 mW and the Nd:YVO4 laser provides a power of up to 300 mW. This leads to corresponding power densities of $\sim 2 \times 10^6$ W/cm^2 and $\sim 40 \times 10^6$ W/cm^2 respectively for a focused laser spot diameter of 1 μm. The laser is focussed through a microscope equipped with 10×, 50× and 100× objectives. The PL emitted by the studied sample is then dispersed by a 150 gmm^{-1} or a 1200 gmm^{-1} grating and detected by either a nitrogen-cooled (InGa)As array photodiode (800 nm ≤ λ ≤ 1500 nm) or by a CCD camera (200 nm ≤ λ ≤ 1100 nm).

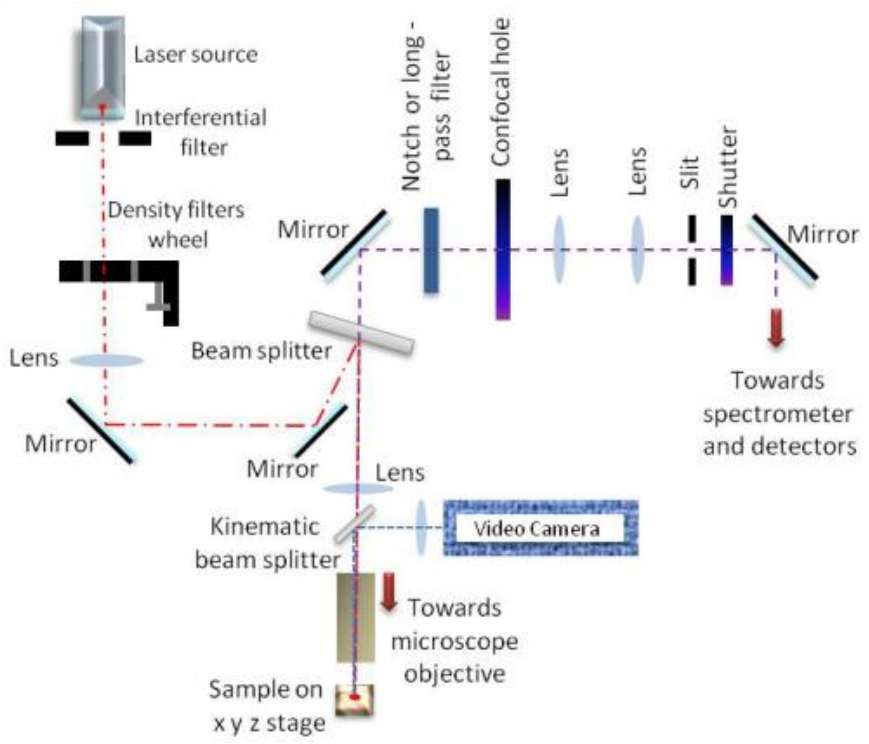

Figure 2-9 Schematic of experimental setup used in micro-PL studies.

In this work we used micro-PL set-up to map the optical properties of photonic crystals fabricated, by Mr Andrew Knott, using the Nanoscribe Photonic Professional GT 2PP three dimensional microfabrication system. Figure 2-10 illustrates the set-up consisting of a highly accurate positioning system combined with a femtosecond laser and a CCD camera which allows the process to be monitored in real time.

Initially, the ultra-short Ti:sapphire NIR laser pulses (< 100 fs) are focused onto a liquid photo resist, which has been drop-cast onto a glass substrate. The pulses initiate two-photon absorption and subsequent excitation to a higher energy electronic state. This leads to chain-growth polymerization of molecules incorporating double or triple carbon-carbon bonds. Non-illuminated regions remain filled with polymer subunits and are washed out to reveal the final structure [109]. The system can reproduce feature sizes down to 100 nm with a lateral resolution down to 300 nm [110] and a typical vertical resolution of ~800 nm [111].

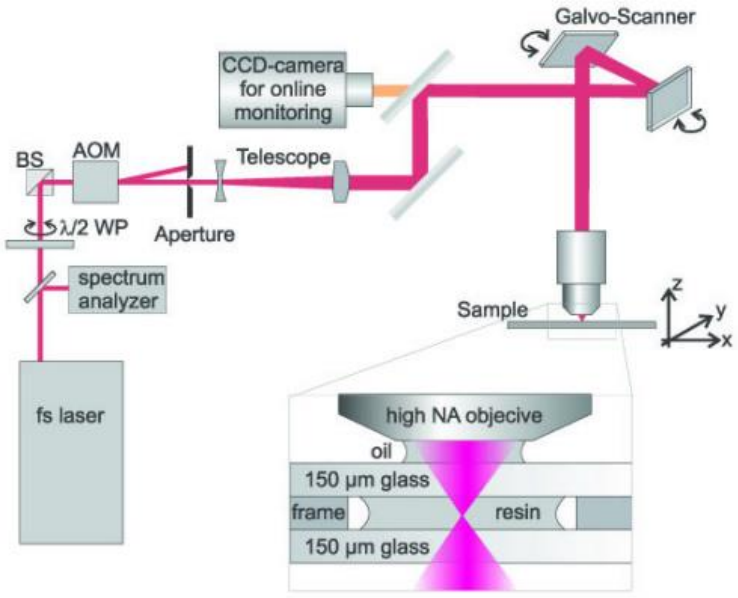

Figure 2-10 Set-up for fabrication of 3D structures by 2PP [109]

Chapter 3

Properties of Mn^{2+} doped QDs

Controlling the incorporation of magnetic ions into colloidal QDs enables the tuning of the magnetic and optical properties of the nanocrystals [18, 112]. Establishing the successful incorporation of the ions and determining the effects on the fundamental properties, requires the use of several complementary techniques.

Prior to performing the EPR studies, all samples were characterized using standard techniques and the results were compared to those previously published to ensure consistency of the samples.

3.1 Morphological, optical and magnetic properties of PbS:Mn

High resolution transmission electron microscopy (HRTEM) studies show that the nanocrystals have a circular shape, and highly crystalline core which is not affected by the incorporation of Mn (Figure 3-1a). Electron diffraction results show that they

also retain the rock-salt crystal structure of bulk PbS. The histogram in Figure 3-1b shows the size distribution of undoped nanocrystals compared to that of nanocrystals doped with Mn = 5 %. The distribution is not affected by the incorporation of Mn and AFM studies show an average nanoparticle diameter of (4.5±1.0) nm for samples with Mn concentrations, Mn ≤ 7 %.

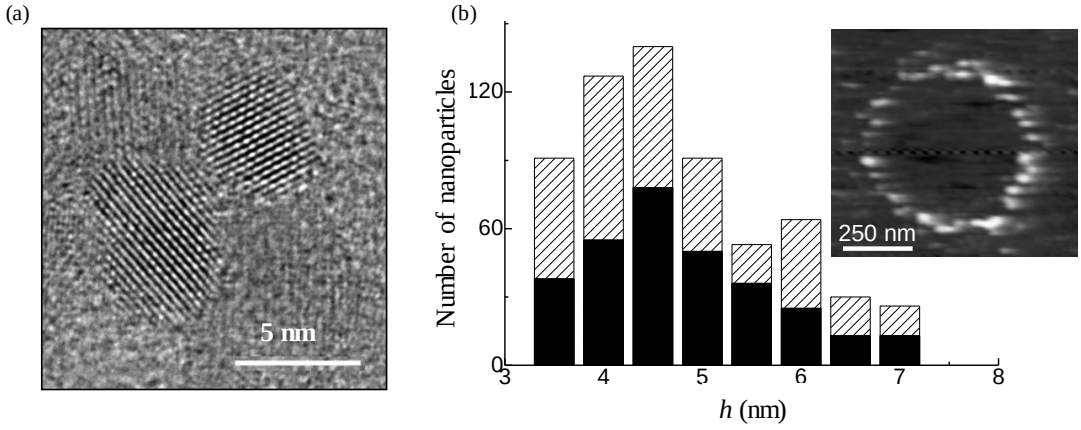

Figure 3-1 (a) HRTEM images of Mn-doped PbS nanoparticles. (b) Histogram showing the size distribution of the QDs as derived from AFM for PbS QDs with Mn_{EDX} = 0% (black bars) and 5% (patterned bars). Inset: AFM image of Mn-doped PbS QDs [112].

The successful incorporation of Mn into the QDs was confirmed by compositional characterization obtained using energy-dispersive X-ray (EDX) spectroscopy. A peak associated with Mn was observed at 5.9 keV, (Figure 3-2a). However, analysis of the EDX spectra show that not all of the Mn used in the precursor is incorporated into the nanocrystals and that the deviation increases with higher Mn content, (Figure 3-2b) [18].

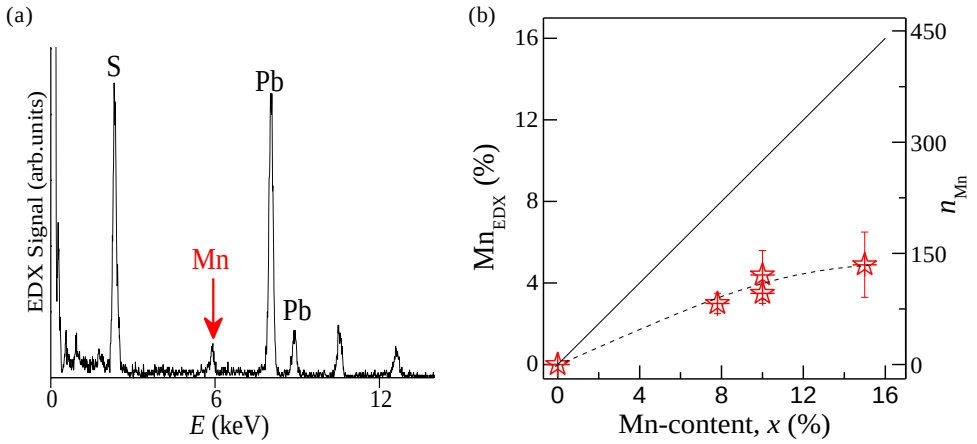

Figure 3-2 (a) EDX spectrum (b) Mn content measured by EDX, Mn_{EDX} , as a function of the nominal Mn content. The dashed line is a guide to the eye. The right axis represents the number of Mn ions per QD [18].

In IV-VI QDs the Mn-related PL emission (E ~ 1.9 eV) is either not observed or is much weaker than the QD PL emission that occurs at much lower energies (E_{QD} ~ 1.2 eV) (Figure 3-3a). The QD PL peak tends to blue-shift with increasing Mn concentration as a result of a change in composition, providing a means of tuning the PL emission of the nanocrystals (Figure 3-3b). The blue-shift is attributed to an alloy effect which can be described by Vegard's law for a (PbMn)S alloy with Mn fraction, x:

$$E_g^{PbMnS}(x) = (1-x)E_g^{PbS} + (x)E_g^{MnS}, \tag{3.1}$$

where bandgap energies are E_g^{PbS} = 0.41 eV and E_g^{MnS} = 3.10 eV at T = 295 K [59]. Figure 3-3 also shows weaker temperature dependence of the QD band gap with increasing Mn concentration, as expected for PbMnS alloy, as the temperature coefficient, $\alpha = \partial E/\partial T$, is positive for PbS ($\alpha^{PbS} = +0.52$ meV K^{-1}) [59] and negative for MnS ($\alpha^{MnS} = -2$ meV K^{-1}) [113].

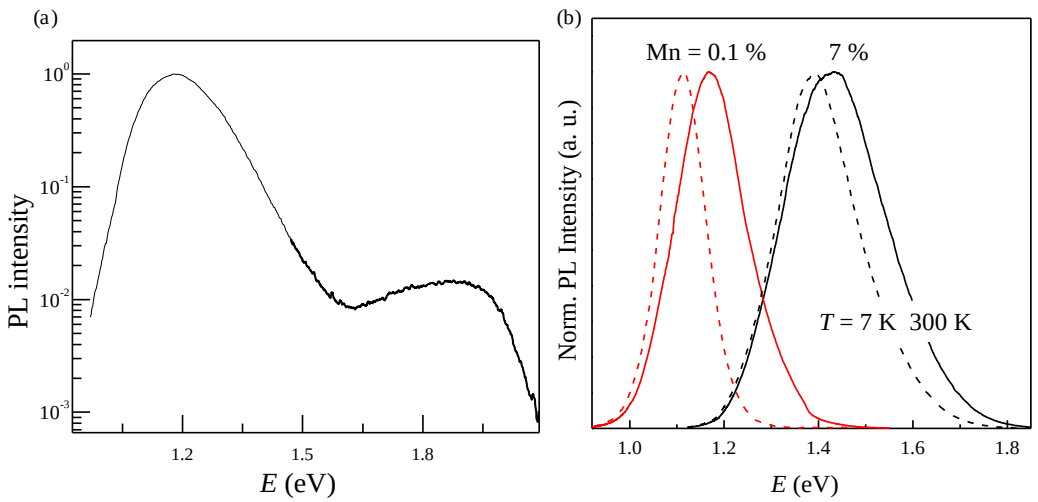

Figure 3-3 (a) PL Spectrum for QDs with Mn = 7 % showing the Mn-dopant PL emission at 1.9 eV and the emission from the QDs at lower energy at T = 300 K, laser excitation, λ = 633 nm, P = 25 W/cm^2 [13]. (b) Normalized PL spectra of Mn-doped PbS nanocrystals [112].

The increase in the bandgap energies, resulting from the alloying effect, induces a corresponding increase in the exciton recombination energy, E_{QD} which can be estimated using a simple spherical model to account for the confinement effects [114]:

$$E_{QD} = \sqrt{E_g^2(x) + 2\hbar^2 E_g(x)\pi^2 m^{*-1} R^{-2}}, \qquad (3.2)$$

Where m^* is the average effective mass and R is the QD radius. Figure 3-4 shows the calculated value of E_{QD} (continuous line) compared with the measured values (dots), showing good agreement up to x ~ 3 %, where x is the nominal Mn concentration. For larger x the disagreement can be attributed to partial incorporation of Mn into the nanocrystal as observed in the EDX studies. These are consistent with the Mn concentration derived from the measured and calculated dependence of E_{QD} on x (Figure 3-4 inset) and, as such, indicate an effective Mn concentration of up to Mn = 8 % in the nanocrystals.

As well as peak emission, the incorporation of Mn affects the optical linewidth. The observed increase is possibly due to slight differences in size distribution and compositional disorder. There is also a small decrease in the emission intensity (<

factor of 10 from x = 0 % to 7 %) suggesting a low level of thermal escape and a low density of Mn-induced non-radiative combination centres.

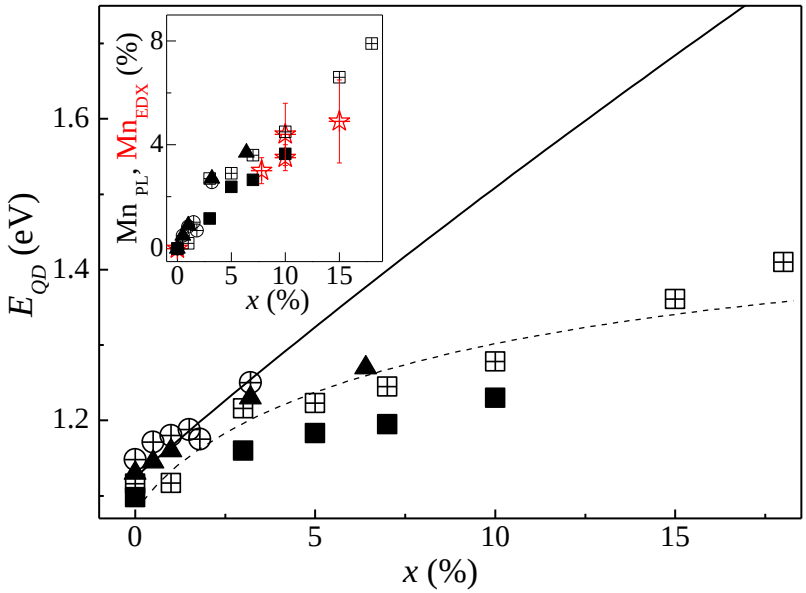

Figure 3-4 Dependence of the QD PL peak energy, E_{QD}, on x (T = 295 K). The continuous line represents the calculated dependence of E_{QD} on x according to the model described in the text. The inset shows the Mn content as estimated from EDX (Mn_{EDX}, stars) and from the calculated and measured values of E_{QD} (Mn_{PL}, dots). To account for different values of E_{QD} at x = 0%, in the calculation of E_{QD}, we have assumed QD radii in the range R = 2.5–2.6 nm [18].

Magnetic studies provide additional confirmation for Mn incorporation into the QDs. K-band ESR results showed that decreasing the dopant concentration allowed the observation of the hyperfine peaks (Figure 3-5). For low Mn concentrations, Mn = 0.5 %, six well defined peaks, corresponding to the hyperfine interactions between *d*-shell electrons (S = 5/2) and the Mn-nuclear spins (I = 5/2) are observed, (see Chapter 2.3.1. and Figure 2-2). The asymmetry in the lines suggests additional unresolved hyperfine splitting likely due to a contribution from Mn ions located on the surface due to the 'self-purification' mechanism (Chapter 1.2.4), as well as those successfully incorporated into the core of the nanocrystals. As the Mn concentration is increased, the strength of Mn-Mn dipolar interactions increases leading to broadening of the hyperfine peaks, (Chapter 2.3.1) until, for Mn = 5 %, the signal merges into one broad line.

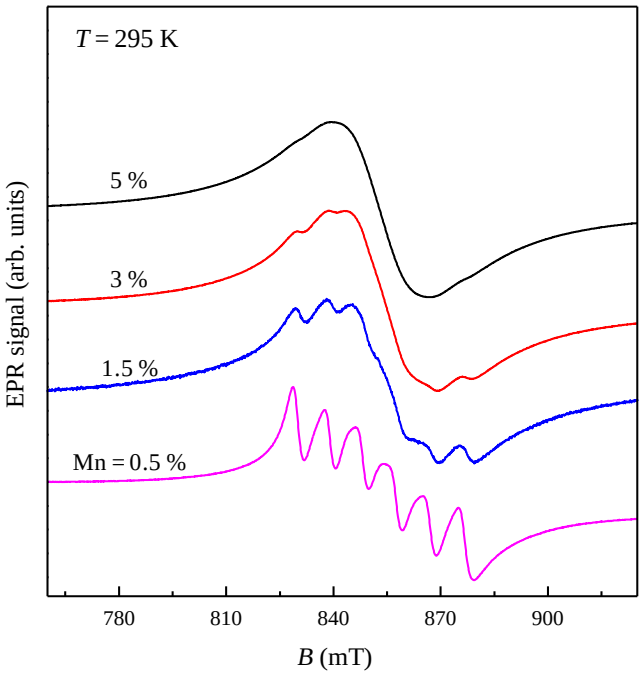

Figure 3-5 Room temperature K-band EPR spectra for Mn-doped PbS nanocrystals with Mn content, Mn = 0.5 to 5% [18].

The combination of morphological, optical and magnetic studies is used to confirm Mn incorporation and to check the consistency of synthesis and QD quality. These studies confirm the successful incorporation of Mn ions into the QDs, and provide a guide for the quantification of Mn and some idea about its location in the nanocrystal. The possibility to change the magnetic and optical properties, provides potential for the use of these nanocrystal in quantum technologies.

In order to build on these results it is necessary to carry out studies in order to further understand the properties of the QDs. In particular, the properties of the Mn spins, and their interactions with the environment.

3.2 Design of core/shell QDs

In this work we investigate the effect of QD morphology on its magnetic properties. We engineer the core/shell structure where Mn^{2+} is either in the core or in the shell of the QD. The comparison of relaxation times between core and core/shell structures enabled us to determine the screening effect of shell growth on Mn interactions with another impurity and with the environment.

Pulsed ESR studies have enabled the identification of the main sources of electron spin dephasing in magnetic colloidal QDs, i.e. Mn–Mn dipolar interactions and interactions of the Mn spins with the protons of the capping ligands [50, 115]. These findings indicate that much longer electron spin dynamics and improved control of quantum coherences could be achieved by engineering of the QD structure.

Overgrowing colloidal QDs to form core/shell structures has been shown to be a useful way to modify the physical properties of nanocrystals. For example, the technique has been used to passivate and protect the QD surface, thus enhancing and stabilizing optical properties [116]. It has also been used to inhibit the rate of energy loss to lattice vibrations, which has potential use in improving the efficiency of photovoltaics [117]. Shell growth has been shown to be effective at suppressing luminescence intermittency (blinking) which has been observed to decrease monotonically with increasing shell thickness [118], and carrier separation and the modification of Auger recombination have also been reported [119]. Recent results have shown that dipolar coupling can be reduced by shell growth due to the increase in distance between magnetic impurities and external nuclear spins [79]. Mn-doped CdSe QDs were compared with nanocrystals with a similar core overgrown with an undoped CdSe shell in which increased T_1 and T_2 times were observed.

In this work we attempt to suppress Mn-Mn interactions by overgrowing the QD core with an undoped PbS shell in order to screen the Mn ions from one another, thus suppressing Mn-Mn dipolar coupling. Furthermore, this technique should also decrease the Mn-^{1}H interactions as the distance between the Mn ions and protons both in the capping ligands and in the matrix increases. We expect that this will lead

to longer relaxation times and could provide an effective tool for the structural adjustment of spin dynamics in PbS:Mn nanocrystals.

We have selected representative samples of different structure, where PbS:Mn (Mn = 0.01 % to 0.05 %) is either in the core or in the QD shell. The samples used in this experiment are listed in Table 3-1 with schematic representations shown in Figure 3-6a. The sample labelled 'bulk' was prepared by thermal annealing of a QD solution in order to remove the capping ligands and facilitate precipitation to emulate a bulk crystal [120]. We would expect a non-uniform distribution of Mn ions in such a system leading to poor isolation of the Mn and shortened coherence times. PL measurements confirmed that there were no discrete structures at sizes of $d < 20$ nm. It was possible to estimate the diameter of the QDs from a comparison of PL and TEM data which was quantified using a hyperbolic-band model for carriers confined in the potential of a spherical QD with infinite barriers [114]. The sample labelled '0.05' had a diameter of 5 nm and a Mn concentration, Mn = 0.05 % which equates to ~1 Mn ion per QD. Sample '0.01' had on average 1 Mn ion in every 5 QDs and as such the Mn ions were physically separated by undoped QDs. A comparison with sample '0.05' is used to extract information about the potential of this 'self-dilution' in order to increase relaxation times. The final two samples, '0.05/0' and '0/0.05', had a core/shell structure with shells of two monatomic layers. Our TEM studies (Figure 3.6c and d) indicate that the core/shell samples form a characteristic elongated structure (width to length ratio, *w/l* ~ 1.5) while maintaining a crystalline core. A comparison of '0.05/0' with '0.05' will enable us to determine the effectiveness of using an un-doped shell as a 'barrier' to reduce the dipolar coupling of nearby Mn ions and also to increase the distance between Mn ions and protons in the capping ligand/matrix, and thus reduce Mn-^{1}H interactions. A further comparison of '0.05/0' with '0/0.05' may give an indication of whether the Mn ions were successfully incorporated into the core or whether they diffused out to the QD surface. All samples were dried to form a 'powder' prior to measuring.

Table 3-1 List of samples

Sample name	Structure	Mn	*N* (Mn per QD)	*d (Mn toMn)*
Bulk	Bulk MnPbS	0.05 %	-	< 5 nm
0.01	MnPbS QD	0.01 %	0.2	5-10 nm
0.05	MnPbS QD	0.05 %	1	5 nm
0.05/0	Core(MnPbS)/Shell(PbS) QD	0.05 %	1	5 nm
0/0.05	Core(PbS)/Shell(MnPbS) QD	0.05 %	1	< 5 nm

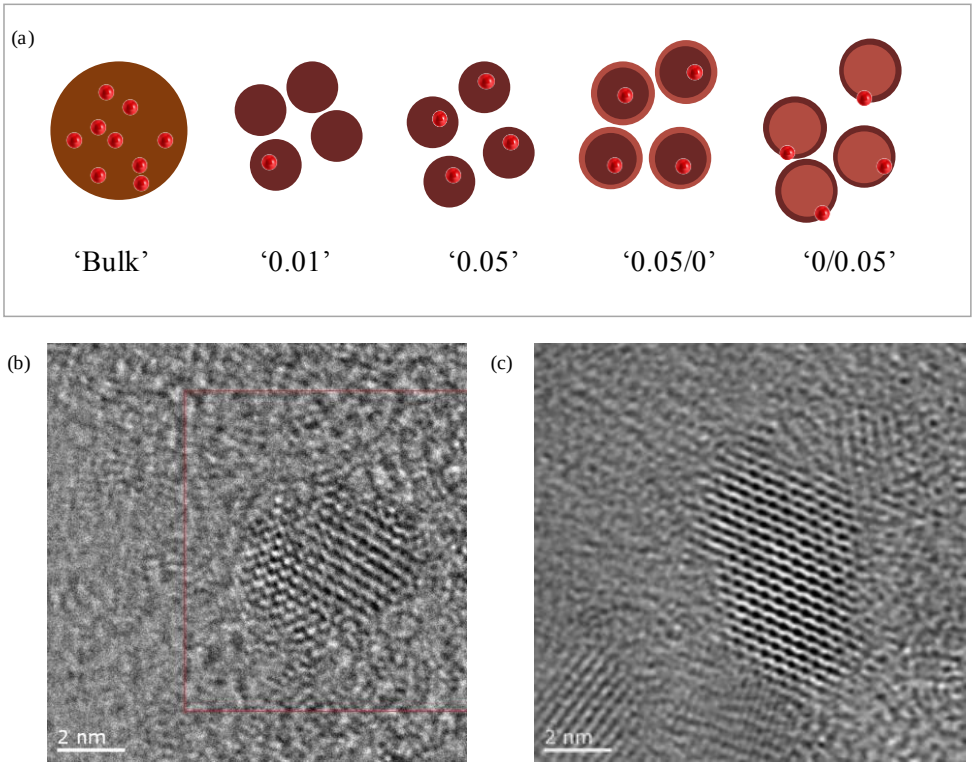

Figure 3-6 Schematic of the samples (a). TEM images of spherical core (b) and elongated core/shell (c) nanocrystals.

3.4 Pulsed-ESR studies

All pulsed-ESR experiments were performed at X-band on a Bruker Elexsys E580 with a 1.8 T electromagnet. Echo field swept (EFS), T_1 and T_2 experiments (Chapter 2.3.2) were measured using powder samples at T = 5 K.

All EFS spectra show six hyperfine lines typical of ^{55}Mn nuclei (I = 5/2) interacting with the *d*-electrons of $^{55}Mn^{2+}$ (S = 5/2) (Figure 3-7). The broad 'wings' which

extend to lower and higher magnetic fields arise from the zero field splitting of the $|m_S| > \frac{1}{2}$ transitions [121].

The five spectra are broadly similar, with each showing indications of six hyperfine lines and broad 'wings' either side. However, the core/shell sample '0.05/0' appears to have less defined hyperfine lines compared with the other samples. It also appears to have a more defined multiplet structure with 'shoulders' visible either side of the main signal and a broad curve centred at B ~ 186 mT.

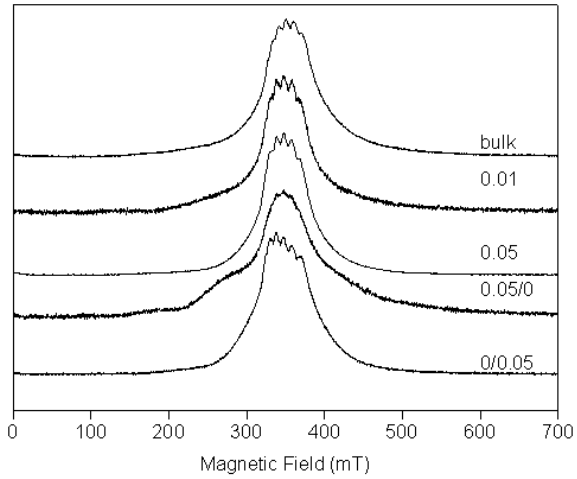

Figure 3-7 X-band echo field swept spectra on powder samples at T = 5 K.

Spin echo decay (SED) experiments were performed and the data were fitted to a stretched exponential function (Equation 2.5) to obtain the phase memory time, T_M; the results are shown in Figure 3-8. The longest T_M times were observed for the sample '0.01' as expected due to the larger average distance between Mn ions. The 'bulk' sample showed the shortest T_M times. This could be a result of the missing screening effect of the ligands or a reduction in the average Mn-Mn distances due to the clustering of the Mn ions. The core/shell sample with the undoped shell, '0.05/0', has a slightly shorter T_M time as compared to sample '0.05'. This is the opposite of what we would have expected and we envisage that this discrepancy could arise from either an inconsistent number of Mn ions successfully incorporated

during synthesis or could be due to significant thermally induced Mn^{2+} outdiffusion in these QDs via the self-purification mechanism.

An unexpected observation of longer T_M time in the sample with an undoped core overgrown with a doped shell, '0/0.05', is likely due to the smaller volume of the shell compared to the core and thus the effective dilution of Mn^{2+}. The stretch parameter for all the samples deviate little from s = 1, as such we can ascribe the dephasing mechanism to spectral diffusion, i.e. nuclear spin motion. A similar trend was observed in the inversion recovery experiment except that '0.05/0' had longer T_1 than '0.05' (Figure 3-9). This may suggest that overgrowing the QD core creates a more rigid nanocrystal. However, at T = 5 K, T_1 (which defines the maximum T_M) is much greater than T_M and, as such, spin-lattice relaxation is not a limiting factor to the coherence time.

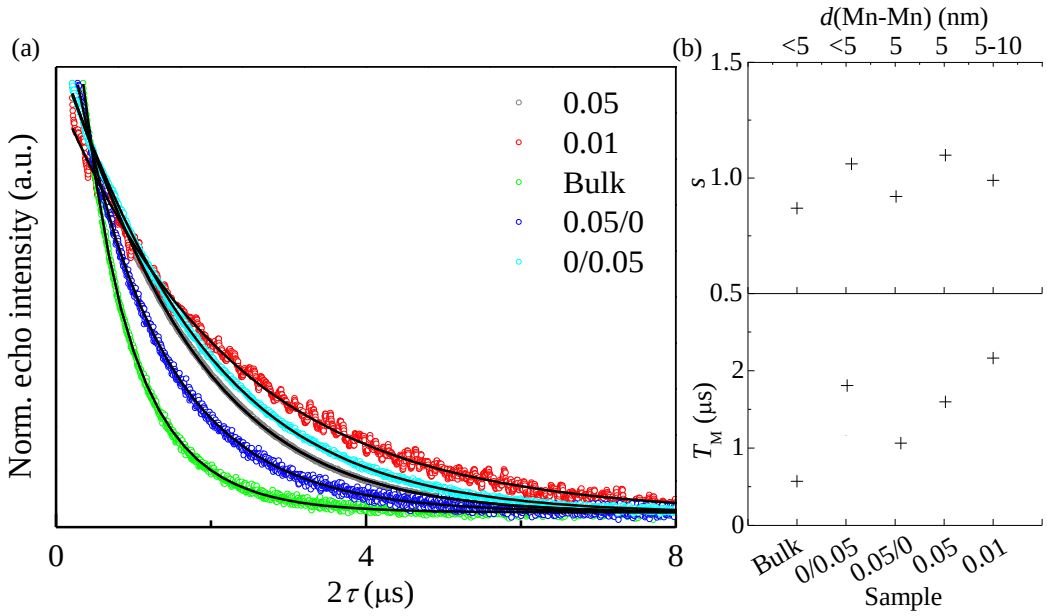

Figure 3-8 (a) X-band spin echo decay experiment at 347.5 mT and 5 K (π = 32 ns). The data was fitted to a stretched exponential function and (b) T_M and the stretch parameter, s were plotted as a function of estimated Mn-Mn distance.

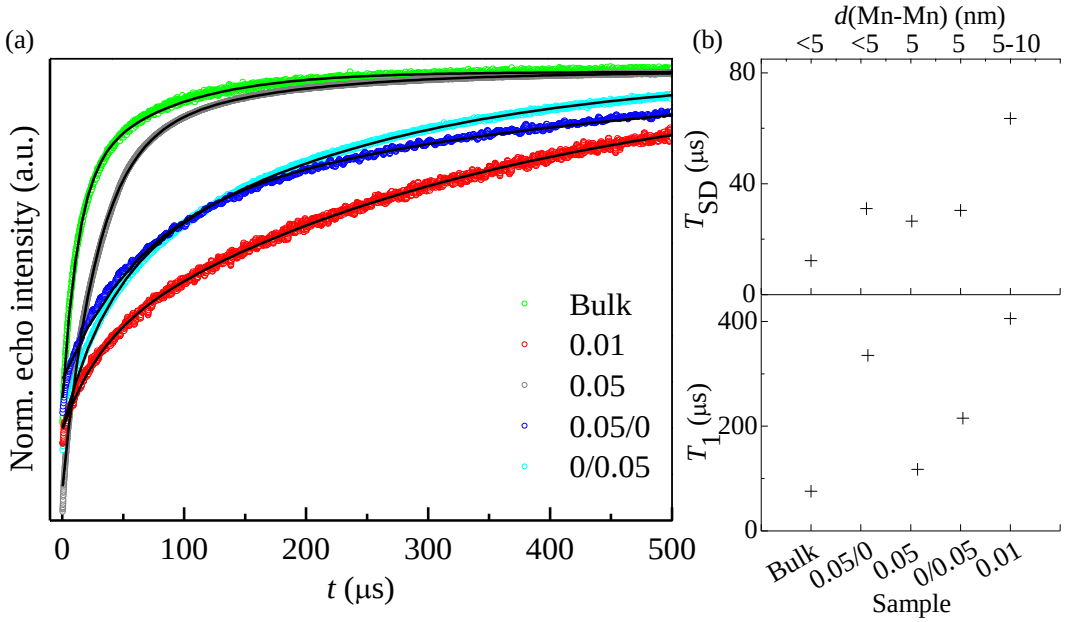

Figure 3-9 (a) X-band inversion recovery experiment at 347.5 mT and 5 K (π = 32 ns). The data was fitted to a biexponential function. (b) T_1 and the spectral diffusion parameter, T_{SD} as a function of estimated Mn-Mn distance.

3.5 Discussion

In both the T_1 and T_2 experiments the 'bulk' sample relaxes quicker than the other samples, suggesting that incorporating Mn into nanocrystals has some beneficial effect on limiting Mn-Mn dipolar coupling. However, the experiment does not appear to show any evidence that engineering core/shell structures has a significant effect on relaxation times.

The comparison between the two core/shell samples was inconclusive. Results on CdSe:Mn and CdSe:Mn/CdSe QDs [79] showed an increase in T_1 from 0.7 ms to 2 ms and an increase in T_2 form 2.1 μs to 4.7 μs with the introduction of an undoped shell. Why we do not observe similar results in the comparison of relaxation times between '0.05/0' and '0.05' cannot be explained within our understanding of the system. The result suggests either that an undoped shell has no screening effect, or that the Mn ions are diffusing from the core, into the shell [122]. Alternatively, it may be the case that the shell was too thin and that it is necessary to perform further

studies on samples with thicker shells. Further studies including detailed morphological characterization and assessment of the Mn^{2+} position in each of these samples is required to draw conclusions.

However, the results presented in this chapter show clear evidence that to separate the Mn ions in order to significantly suppress dipolar interactions it may be necessary to dilute QDs and study their properties in frozen solution or another matrix.

Chapter 4

Electron spin coherence near room temperature

This chapter describes the controlled suppression of Mn-Mn and Mn-^{1}H interactions by the dilution of nanocrystals in deuterated solution. Measurements were made in frozen solution resulting in unprecedentedly long phase memory (T_M ~ 8 μs) and spin–lattice relaxation (T_1 ~ 10 ms) time constants for Mn^{2+} ions at T = 4.5 K, and in observable electron spin coherence near room temperature (T_M ~ 1 μs).

In this work we isolate Mn^{2+} ions by dispersing colloidal PbS:Mn QDs in a proton-spin free matrix. This resulted in the controlled suppression of Mn–Mn dipolar interactions in the QD ensemble and reduced interactions with surrounding nuclear spins. The isovalence of Mn^{2+} and Pb^{2+} atoms ensures that the Mn-doped PbS QDs are electrically neutral and that Mn–Mn interactions mediated by free electrons (i.e. RKKY) are absent [123]. The results of pulsed ESR experiments show unprecedentedly long phase memory time and spin–lattice relaxation time constants for Mn spins. Furthermore, coherence could be observed near room temperature.

4.1 Designing QDs for increased T_M

Thioglycerol/dithiolglycerol capped PbS:Mn colloidal QDs, Figure 4-1, were synthesised in aqueous solution (Chapter 2.1) with Mn concentration, Mn = 0.05% (sample $Mn_{0.05\%}$) and Mn = 0.01% (sample $Mn_{0.01\%}$). The synthesis of PbS:Mn QDs in 99.8% deuterated water (sample $DMn_{0.05\%}$) produces a sample free from proton-spin solvent molecules. The QDs were measured as powders and as frozen solutions in H_2O and in D_2O, and in 1:1 mixtures of H_2O:$C_3H_8O_3$ (glycerol-H_8) and D_2O:$C_3D_8O_3$ (glycerol-D_8). Figure 4-1 illustrates the magnetic interactions between two neighbouring QDs dispersed in water with strong hyperfine interactions between the Mn spins and the capping ligands and weak hyperfine interactions between the Mn spins and the water molecules.

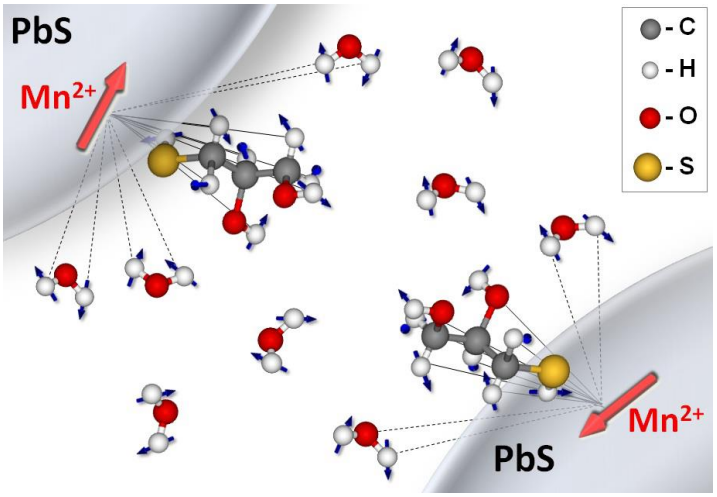

Figure 4-1 Representation of magnetic interactions between Mn ions (red arrows) in two neighbouring PbS QDs dispersed in water. The hyperfine interactions between Mn spins and proton nuclear spins of the capping ligands and solvent matrix are shown. The continuous lines indicate strong interactions while the dotted lines indicate weak interactions.

4.2 Continuous–wave ESR

Figure 4-2a (dotted line) shows the X-band CW-ESR spectrum for powder $Mn_{0.05\%}$ at T = 300 K. The spectrum consists of six lines centred close to the free electron g

value. We ascribe the six features to the six hyperfine lines of ^{55}Mn nuclei (I = 5/2) interacting with the d-electrons of Mn^{2+} (S = 5/2) [124]. The isotropic spin Hamiltonian parameters [124] g = 2.001±0.005 and A = 267±1 MHz were determined from the CW-ESR simulation (Figure 4-2a continuous line). This was consistent with previously reported results [66, 115]. An intrinsic Lorentzian linewidth Γ_L = 0.5±0.1 mT was assumed for the fit. We obtained further constraints to these parameters by fitting a CW-ESR spectrum at W-band frequency (ν_{mw} ~ 94 GHz, Figure 4-2b) with *Easyspin* [102] using the spin-Hamiltonian model [124],

$$\hat{H} = g\mu_B \boldsymbol{B}\hat{S} + D\hat{S}_z^2 + E\left(\hat{S}_x^2 + \hat{S}_y^2\right) + A\hat{S}\hat{\boldsymbol{I}} \tag{4.1}$$

where g is the Landé g factor, μ_B is the Bohr magneton, $\boldsymbol{B}$ is the magnetic field vector, D and E are the axial and planar magnetic anisotropy, A is the isotropic hyperfine coupling constant, and S and I are the electron and nuclear spin quantum numbers, respectively. The first, second and third terms account for the Zeeman interaction, the zero-field splitting, and the hyperfine interaction, respectively. At X-band the zero-field splitting parameter, D, could not be quantified unequivocally because of the large linewidth broadening most likely caused by large strain of the spin-Hamiltonian parameters. However, at W-band, the fit is considerably more satisfactory than a simulation with cubic symmetry (Figure 4-2b, blue spectrum). This shows features (labelled *) that strongly diverge from the experimental spectrum as well as a discrepancy in the symmetry of the hyperfine lines. Therefore, we assume the anisotropic axial character of the Mn local environment in the QDs and in Figure 4-2a we report an attempt with D = 50 MHz and an overall g-, A- and D- strain, $\Gamma = \sqrt{\Gamma_x^2 n_x^2 + \Gamma_y^2 n_y^2 + \Gamma_z^2 n_z^2} = 11.78$ mT, where $\Gamma z/\Gamma xy$ = 3:1 and n = (n_x, n_y, n_z) defines the orientation of the magnetic field vector. The small magnetic anisotropy, D, and large anisotropic strain suggest that Mn ions are surrounded by a distribution of distorted cubic environments, possibly due to their proximity to the QD surface.

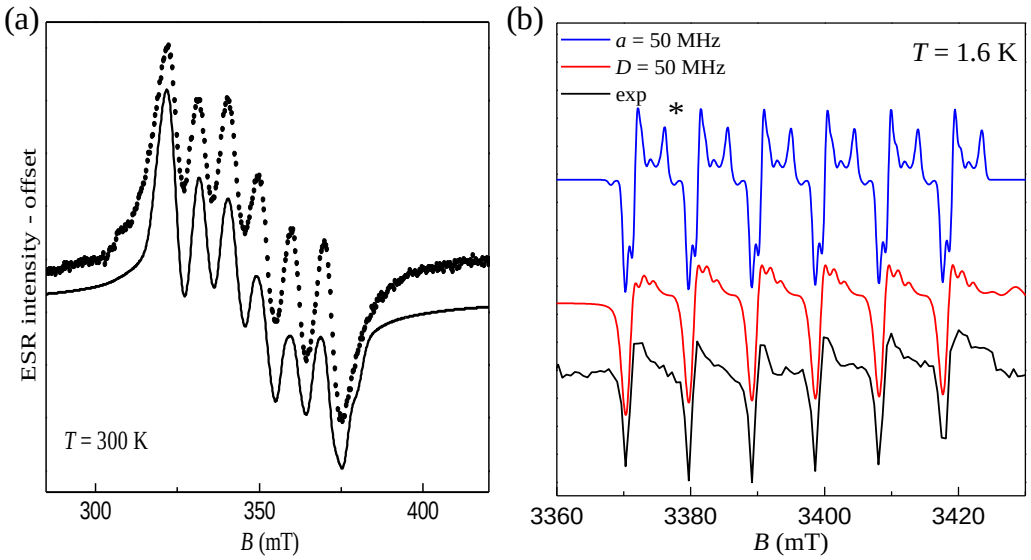

Figure 4-2 (a) X-band CW-ESR spectrum (dotted line) for powder sample of $Mn_{0.05\%}$ and simulation (continuous line) to a spin-Hamiltonian model. (b) Experimental W-band CW ESR spectrum and simulations performed with cubic, *a*, (blue) and axial, *D*, (red) symmetry with *D* strain of 30%.

4.3 Mn–Mn dipolar interactions

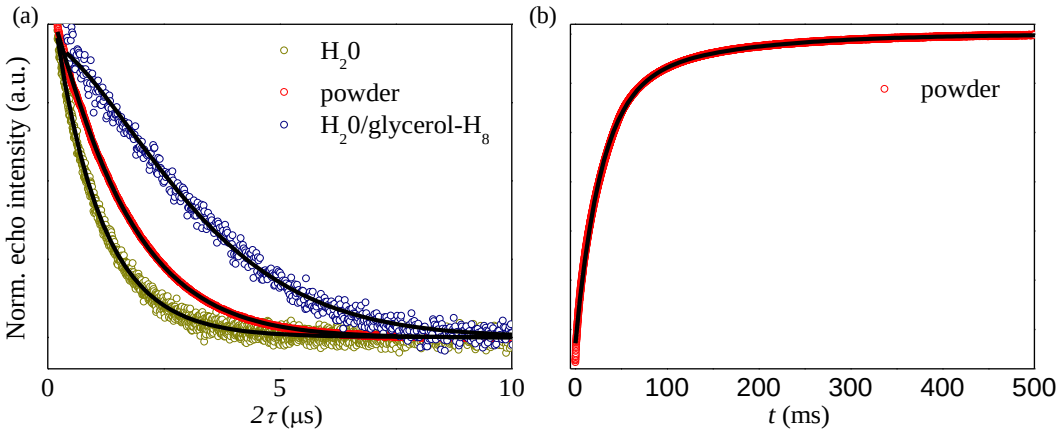

Figure 4-3 Spin dynamics for quantum dots in different matrices. (a) Hahn echo decay for $Mn_{0.05\%}$ as powder and frozen solutions at T = 5 K. Black lines are fits to stretched exponential (Eq. 2.5). (b) Inversion recovery echo trace for powder sample with biexponential fit (Eq.2.6) (black line).

Table 4-1 Results of the fittings of the spin echo decay (Eq. 2.5) and inversion recovery data (Eq. 2.6) for Mn = 0.05 %.

$Mn_{0.05\%}$	**π (ns)**	**τ (ns)**	**T_M (μs)**	**s**	**T_1 (ms)**	**T_{SD} (ms)**
Powder	32	130	1.56 ± 0.01	1.13 ± 0.01	130 ± 10	27 ± 5
Powder	120	210	1.69 ± 0.01	1.13 ± 0.01	-	-
H_2O	120	210	0.99 ± 0.01	0.96 ± 0.01	-	-
H_2O/glyc.-H_8	32	400	3.54 ± 0.01	1.51 ± 0.02	-	-

The effect of the Mn-Mn separation in PbS:Mn QDs diluted in different solvents on T_M and T_1 (see Chapter 2.3.2 for pulse sequences) of Mn^{2+} ions at T = 5 K was examined (Figure 4-3 and Table 4-1). All the pulsed-ESR experiments for samples with Mn = 0.05 % were conducted at B = 345 mT, which corresponds to the maximum echo intensity of the EFS spectrum (Figure 4-4).

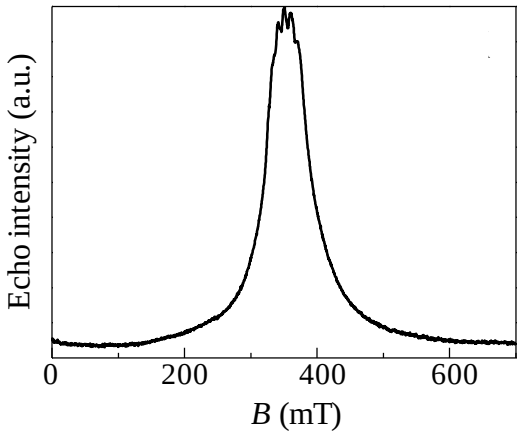

Figure 4-4 EFS spectrum measured for a powder $Mn_{0.05\%}$ sample at T = 5 K with a maximum echo intensity at B = 345 mT.

For $Mn_{0.05\%}$ QDs as powder (Figure 4-3a, red curve), the fit of the spin echo decay to a stretched exponential decay function gives T_M ~ 1.6 μs, while the fit of the inversion recovery echo signal to a biexponential function (Figure 4-3b) gives T_1 ~ 130 μs and T_{SD} ~ 27 μs. The fast relaxing contribution, T_{SD}, is ascribed to spectral diffusion [125]. In the $Mn_{0.05\%}$ powder sample the average Mn-Mn distance is d ~ 6 nm [115]. Using this distance we can use a simple model for two interacting spins to estimate the maximum dipolar field, B_{dip}, experienced by next neighbour Mn ions, as B_{dip} ~ 50 μT, corresponding to a dipolar time constant T_{dip} ~ 1 μs which is derived from the dipolar frequency,

$$\frac{\omega_{dip}}{2\pi} = \frac{1}{T_{dip}} = \frac{\mu_0 g_A g_B \mu_B^2 S_A S_B}{2\pi h r^3} \tag{4.2}$$

for two S_A and S_B electron spins at distance r [125]. These values suggest that dipolar interactions between Mn ions are an important source of electron spin dephasing. To increase the Mn-Mn separation, we disperse the QDs in aqueous solution with density, δ = 5 mg/ml. This corresponds to an average distance between

the Mn^{2+} ions of d ~ 35 nm. Thus, we estimate B_{dip} ~ 0.2 μT with an upper bound for T_M given by T_{dip} ~ 60 μs. Surprisingly, the resulting spin echo decay (Figure 4-3a, yellow curve) shows a faster relaxation, T_M ~ 1.0 μs at T = 5 K, compared to that of the powder. A combination of several factors contributes to fast spin echo decay: the formation of regions with high QD concentrations resulting from the crystallization of water [126], the presence of solvent protons at a short distance from the Mn^{2+}, and the absorption of mw radiation by the water molecules, which leads to enhanced vibrations and librations [127] of the dielectric dipoles and heating of the environment. To overcome these effects, we dilute the QDs in H_2O/glycerol-H_8. Lattice vibrations and QD agglomeration can be reduced by adding glycerol to aqueous solution to produce a glass [128]. As shown in Figure 4-3a (blue curve), in this case we achieved a significantly longer spin-echo decay (T_M ~ 3.5 μs) compared to both $Mn_{0.05\%}$ QDs as powder and dispersed in water. Reducing the Mn concentration in the QDs to Mn = 0.01% in frozen H_2O/glycerol-H_8 (Figure 4-5) did not lead to significant changes in the spin echo decay, T_M(0.01%) = 3.48ms (table 4-2). This proves that we have reached a limit where the separation between the QDs is large enough to suppress Mn–Mn dipolar interactions.

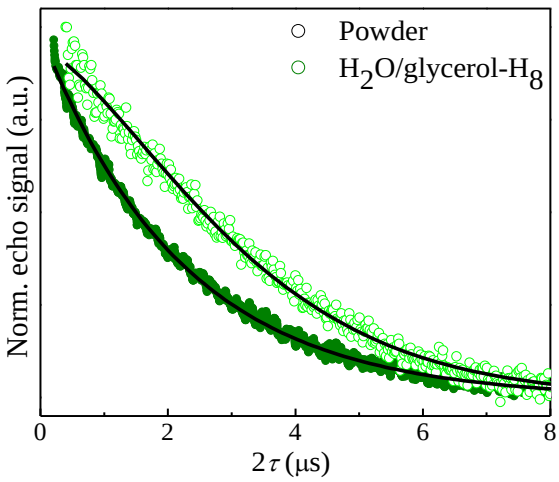

Figure 4-5 Spin echo decay traces for Mn0.01% at T = 5 K as powder (dark green) and as frozen solution (light green).

Table 4-2 Results of fitting to the spin echo decay (Eq. 2.5) and inversion recovery (Eq. 2.6) data for Mn = 0.01 %.

$Mn_{0.01\%}$	π (ns)	τ (ns)	T_M (µs)	s	T_1 (µs)	T_{SD} (µs)
Powder	120	210	2.22 ± 0.01	1.00 ± 0.01	332.5±0.7	29.7±0.2
H_2O/glycerol-H_8	32	400	3.48 ± 0.02	1.45 ± 0.02	-	-

4.4 Nuclear spin bath dephasing.

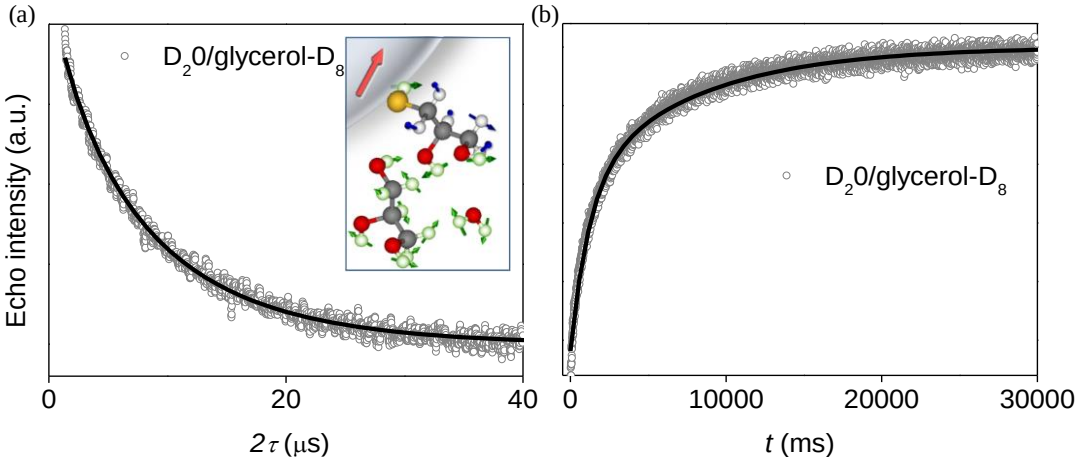

Figure 4-6 Spin dynamics for quantum dots in deuterated solution for $Mn_{0.05\%}$ at T = 5 K. (a) Spin echo decay. Black lines are fits to stretched exponential (Eq. 2.5). Inset: representation of QDs in D_20/glycerol-D_8. (b) Inversion recovery echo trace with biexponential fit (Eq. 2.6) (black line).

Table 4-3 Results of fitting to the spin echo decay (Eq. 2.5) and inversion recovery (Eq. 2.6) data for Mn = 0.05 % in deuterated solution.

$Mn_{0.05\%}$	π (ns)	τ (ns)	T_M (µs)	s	T_1 (ms)	T_{SD} (ms)
D_2O/glyc.-D_8	32	400	8.4 ± 0.01	1.0 ± 0.1	7670 ± 70	1230 ± 10
	600	1362	8.45 ± 0.06	-	-	-

The suppression of Mn–Mn dipolar interactions enables identification of other sources of electron spin dephasing. Protons present in water can dephase electron spins via nuclear spin flip-flop (i.e spin diffusion) and nuclear motions (i.e. rotational diffusion and vibration processes) [126]. Dilution of QDs in deuterated water and deuterated glycerol (Figure 4-6) should lead to longer T_M because the electron–nuclear spin coupling is diminished by the smaller magnetic moment of D-nuclei compared to H, μ(D)/μ(H) = 0.307, and by the smaller nuclear spin diffusion effects, which scale as the square of the nuclear magnetic moment. Overall, in the absence

of protons, T_M is expected to increase approximately with the negative third power of the nuclear moment [126], μ^{-3}, which corresponds to a factor of 35. Furthermore, we find that T_1 is increased by a factor of ~80 compared to $Mn_{0.05\%}$ in powder, thus suggesting that spin–lattice relaxation processes are mediated by Mn–Mn and Mn–nuclear spin bath interactions.

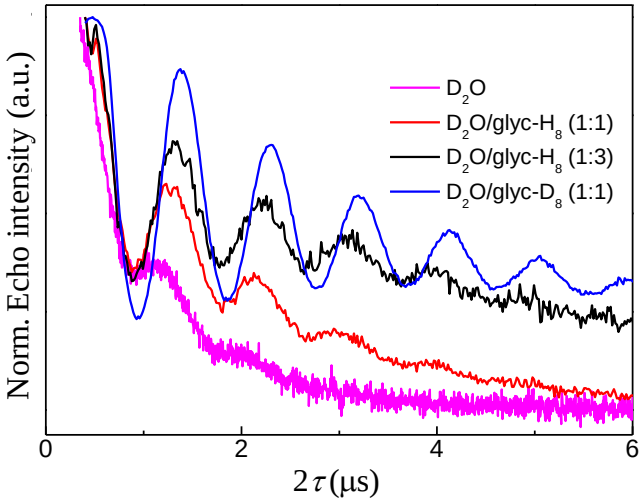

Figure 4-7 Spin echo decay traces recorded for $Mn_{0.05\%}$ in different deuterated solvent matrices at T = 5 K and B = 345 mT.

It was found that different deuterated matrices produced similar effects to those observed in the protonated matrices (Figure 4-7). The dispersion of $Mn_{0.05\%}$ in D_2O (no glycerol) leads to a spin echo decay, (T_M ~ 1.1 μs), which is faster than the spin echo decay observed in powder samples (T_M ~ 1.6 μs). The addition of protonated glycerol with ratios 1:1 and 1:3 (red and black curves) show a longer spin echo decay (T_M ~ 1.9 μs and ~ 5.4 μs, respectively). The dispersion of $Mn_{0.05\%}$ in D_2O and deuterated glycerol shows a still longer spin echo decay (T_M ~ 8.5 μs) modulated by deuterium spin flip–flops.

4.5 Electron–nuclear interactions

To identify the nuclear species responsible for the electron spin dephasing, we have performed 2p-ESEEM experiments on powder $Mn_{0.05\%}$ and on $DMn_{0.05\%}$ in

D_2O/glycerol-D_8 (Figure 4-8). The 2p-ESEEM data were fitted to a modulated stretched exponential function:

$$I(2\tau) = I(0)\exp\left(-\frac{2\tau}{T_M}\right)^{s} + \langle k\rangle\cos(\omega_I\tau)\exp\left(-\frac{2\tau}{T_N}\right)^{s_N}, \qquad (4.3)$$

where $\langle k\rangle$ is the modulation depth, ω_I is the Larmor angular frequency of a nucleus coupled to the electron spin, T_N and s_N are the decay constant and stretching parameter of the electron–nuclear spin oscillations, respectively.

For $Mn_{0.05\%}$, the modulated part of the echo decay is dominated by a contribution with a shorter period than for $DMn_{0.05\%}$. The Fast Fourier Transform (FFT) of the data shows intense peaks at $\omega_I/2\pi$ ~ 14.9 MHz for $Mn_{0.05\%}$ and $\omega_I/2\pi$ ~ 2.3 MHz for $DMn_{0.05\%}$ QDs (see inset in Figure 4-8), which are close to the natural Larmor frequencies, at B = 345 mT, of hydrogen ($\omega_I/2\pi$ = 14.69 MHz) and deuterium ($\omega_I/2\pi$ = 2.25 MHz), respectively. The observation of Mn–deuterium ESEEM for $DMn_{0.05\%}$ can be attributed to the proximity of deuterated solvent molecules to Mn ions near the QD surface. The absence of modulations corresponding to the ^{1}H Larmor frequency may be explained by the partial exchange between deuterium molecules and protons of the O–H and S–H groups in the capping ligands (Figure 4-6a, inset). We note that despite the relatively large natural abundance of ^{207}Pb nuclei (~22%) their contribution to the ESEEM spectra ($\omega_I/2\pi$ = 3.08 MHz) could not be observed [115].

For $Mn_{0.05\%}$ a small peak at $\omega I/2\pi$ ~ 3.9 MHz (indicated by *, inset Figure 4-8) is observed close to the Larmor frequency of ^{23}Na ($\omega_I/2\pi$ = 3.88 MHz, $\mu = 2.22\mu_N$, and natural abundance ~100%). The presence of ^{23}Na nuclei could be due to the use of Na salts in the synthesis and possibly incorporated as interstitial impurity within the QDs [129]. Alternatively, this peak could be caused by coupling to ^{207}Pb. A weak peak at $\omega/2\pi$ = 29.5 MHz is also observed, which we ascribe to the sum, $\omega_+ = \omega_\alpha + \omega_\beta$, harmonic of the principal proton frequencies, $\omega_I \approx \omega_\alpha \approx \omega_\beta$, resulting from Mn–proton spin dipolar interactions [125].

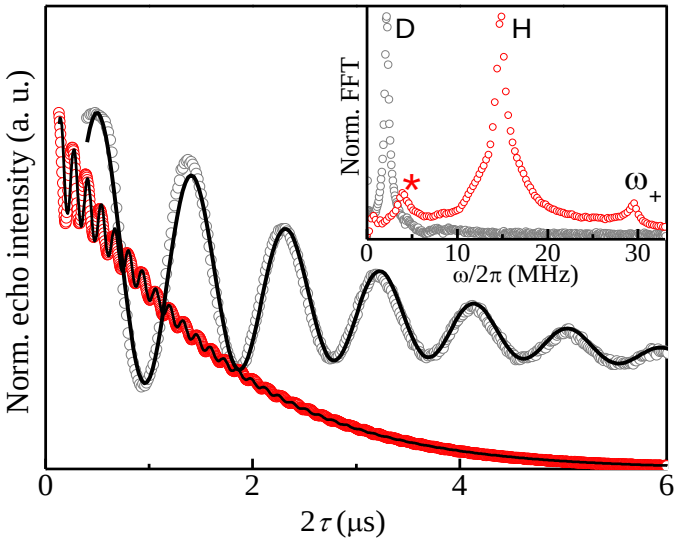

Figure 4-8 Electron–nuclear spin dynamics. 2p-ESEEM traces of $Mn_{0.05\%}$ powder (red circles) and $DMn_{0.05\%}$ frozen solution in D_2O/glycerol-D_8 (grey circles) at T = 5 K and their Fast Fourier Transform (inset). Black lines are simulations by equation (4.3).

Table 4-4 Fitting parameters for the 2p-ESEEM trace (Eq. 4.3).

$Mn_{0.05\%}$	***π*** **(ns)**	***T_N*** **(μs)**	***s_N***	***k***
Powder	32	0.5	1.0	0.12
H_2O/glyc.-H_8	32	1.5	0.9	0.09
D_2O/glyc.-D_8	32	2.4	1.3	0.52

The ESEEM modulation depth, *k*, depends on the electron–nuclei distance as well as the nuclear spin density close to the electron spins [100]. We find that *k* is essentially unchanged for powder and the corresponding frozen solution (see Table 4-3), suggesting a similar nuclear spin density for both samples.

4.6 Spin dynamics temperature dependence

Long lifetimes of Mn^{2+} spins in PbS QDs are observed at $T > 5$ K for $Mn_{0.05\%}$ and $DMn_{0.05\%}$. The protonated sample, $Mn_{0.05\%}$, depends linearly on temperature up to T = 40 K (Figure 4-9). At higher temperature the echo signal drops below the noise

level. We observe that s gradually decreases from ~ 1.8 at T = 3.2 K, reaching a plateau at ~ 1 for T > 15 K. For 2 < s < 3, the dephasing mechanism is ascribed to nuclear spin flip–flop processes (i.e. nuclear spin diffusion), whereas for 0.5 < s < 1 it is ascribed to the motion of the nuclei relative to the electron spin. Based on the above arguments, our results show that for T > 15 K the electron spin dephasing is dominated by nuclear spin motions, whereas, for T < 15 K, the nuclear spin motion and spin flip–flop processes both contribute to dephasing the electron spins.

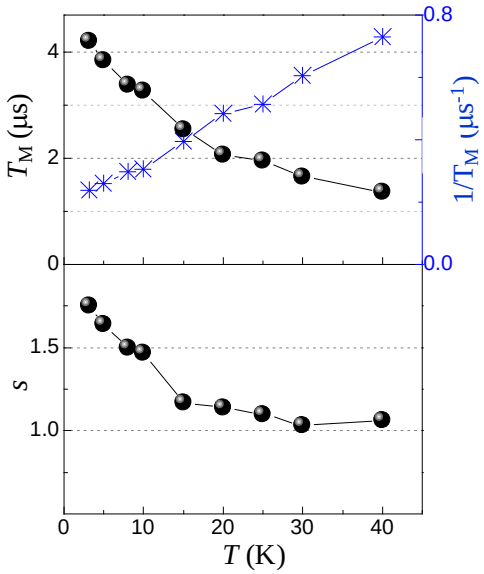

Figure 4-9 Temperature dependence of T_M (spheres), $1/T_M$ (stars), and s for $Mn_{0.05\%}$ in H_2O/glycerol-H_8.

For T < 20 K in the deuterated sample, T_M is essentially constant while at higher temperature T_M smoothly decreases, reaching T_M ~ 1.0 μs at T = 230 K (Figure 4-10). For T > 230 K the echo intensity is comparable to the noise level, preventing analysis of T_M. The stretching parameter s remains constant at s = 1 across the entire temperature range investigated. For T < 80 K, T_1 is much larger than T_M and depends strongly on temperature, with T_1 ~ 10 ms at 4.5 K and T_1 ~ 9 μs at 80 K. For T > 80 K, T_1 ~ T_M and its temperature dependence is weaker.

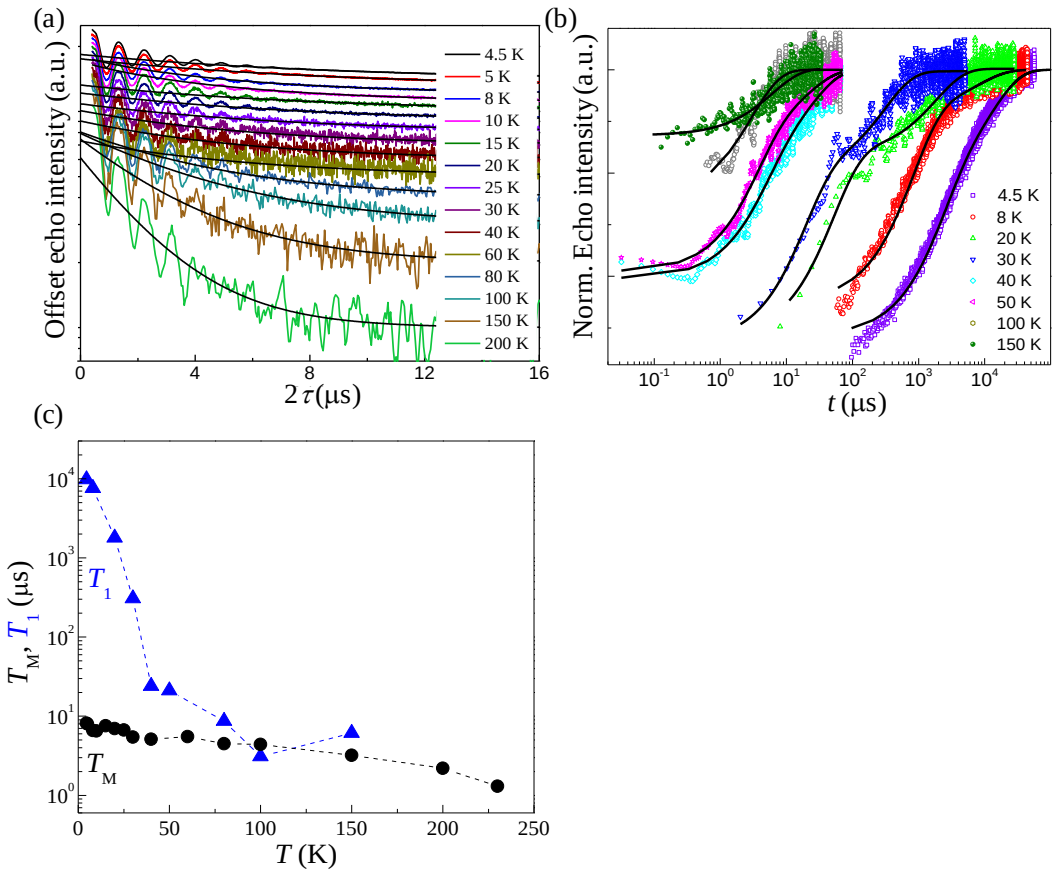

Figure 4-10 (a) Spin echo decay traces for 4.5 K≤T≤200 K. (b) Inversion recovery traces for 4.5 K ≤T≤150 K. (c) Temperature dependence for T_M (spheres) and T_1 (triangles) for $DMn_{0.05\%}$ in D_2O/glycerol-D_8. Dashed lines are guides for the eye.

Table 4-5 Fitting parameters for the spin echo and inversion recovery traces shown in Figure 4-10 for $DMn_{0.05\%}$ in D_2O/glycerol-D_8.

T (K)	T_M (μs)	T_1 (μs)	T_{SD} (μs)
4.5	8.19 ± 0.02	9790 ± 50	1034 ± 10
5	7.97 ± 0.01	8440 ± 70	1230 ± 12
8	6.61 ± 0.04	7300 ± 200	758 ± 10
10	6.51 ± 0.05	-	-
15	7.58 ± 0.08	-	-
20	6.98 ± 0.07	1830 ± 40	50 ± 3
25	6.7 ± 0.2	-	-
30	5.44 ± 0.08	308 ± 10	18 ± 2
40	5.1 ± 0.1	24 ± 6	4.4 ± 0.8
50	-	21 ± 5	3.4 ± 0.4
60	5.5 ± 0.2	-	-
80	4.5 ± 0.2	8.7 ± 2	1.7 ± 0.2
100	4.4 ± 0.2	3.1 ± 0.5	-
150	3.2 ± 0.3	6.1 ± 0.6	-
200	2.2 ± 0.4	-	-
230	1.3 ± 0.5	-	-

4.7 Discussion

Our study indicates that the relaxation times of Mn spins in PbS QDs can be tailored by modifying the QD environment. Dispersing the QDs in a proton free glassy matrix has been shown to suppress major sources of electron spin dephasing, i.e. Mn–Mn dipolar interactions, and minimize Mn-nuclear interactions. As a result, we have achieved an enhancement of T_M by a factor of ten, and we have observed spin coherence near room temperature. This was possible due to the large separation between the Mn ions (d ~ 35 nm) and the small magnetic moment of deuterated matrix molecules. This led to a reduction of the time dependent magnetic field perturbations seen by each individual Mn ion due to the surrounding electron and nuclear spins.

Our results also show that in the temperature regime below 20 K, where $T_1 >> T_M$ and $1/T_M$ is approximately constant, spin–lattice relaxation is not a limiting factor for electron spin coherence. Instead, 2p-ESEEM experiments indicate that electron–deuterium spin interactions represent a source of electron spin dephasing. An approximately monoexponential spin echo decay across all temperatures suggest that nuclear spin diffusion processes are a less important source for electron spin dephasing in deuterated solution than for $Mn_{0.05\%}$ in H_2O/glycerol-H_8. In the latter, the stretching parameter, s, is temperature dependent with $s > 1$ for $T < 20$ K (Figure 4-9). We ascribe this effect to the smaller magnetic moment of deuterium compared to that of protons [130, 131].

At temperatures above 80 K, where T_1 ~ T_M, spin–lattice relaxation processes become a more dominant source of electron spin echo dephasing due to enhanced thermal motion of the nuclear spins of the capping ligands and/or of the solvent molecules near the QD surface. This is likely due to the softening of the glassy matrix as temperatures approach the sample melting point. These motions modulate Mn–nuclear spin dipolar interactions, leading to electron spin dephasing and rapid exchange of magnetic energy between the Mn^{2+} spins and its environment.

In summary, we have demonstrated quantum coherence near room temperature for electrons spins confined in colloidal quantum dots. The long lifetime of electron spin dynamics observed at T = 4.5 K (T_M ~ 8 μ s and T_1 ~ 10 ms) and, the observation of quantum coherence up to T = 230 K (T_M ~ 1 μs) are unprecedented for Mn ions and are very rare amongst transition metal ions. In comparison, T_M or T_2 of Mn spins or confined electrons in other low dimensional systems, such as self-assembled QDs [130, 132, 133], layered magnetic semiconductors [134] and quantum wells [135, 136], do not exceed 1 ns, and those for magnetic colloidal QDs in the solid state are < 1 μs [50, 137]. In addition, we note that T_1 for $Mn_{0.05\%}$ is one order of magnitude longer than that found in self-assembled QDs [130] and diluted magnetic quantum wells [138, 139]. Overall, the T_M and T_1 values we observe for PbS:Mn QDs are comparable only to molecules based on Cr and V ions in D_2O/glycerol-D_8 [140] and on Cu ions diluted in a diamagnetic matrix [76]. Considering that further improvements of the Mn spin lifetime could be achieved by incorporation into nuclear spin free nanocrystals, by deuteration of the capping ligands, by substitution of ligands with larger steric hindrance [141], and by embedding the QDs in a nuclear-spin free matrix rigid at room temperature, colloidal QDs could enable the exploitation of magnetic interactions in confined electron spins for spintronics and quantum information processing application.

Chapter 5

Photonic crystals

Embedding magnetically doped nanocrystals in an optical cavity could have the benefits of a rigid structure for optimised relaxation times, as well as enhanced optical properties of the QDs. In this work we have designed and fabricated 2D photonic crystals using two photon polymerisation (2PP) micromachining. Nanocrystals were incorporated into the structures and the optical enhancement was assessed using micro-PL mapping.

Photonic crystals have the potential to be used in a wide range of applications including miniature lasers [142] and light emitting diodes [143] as well for solar energy harvesting [144]. In recent years, progress has been made in achieving the control of spin qubits coupled to photonic crystal cavities [145]. In this work we incorporate nanocrystals into 2PP micromachined photonic crystals. Our ESR experiments (Chapter 4-5) show that, at temperatures approaching room temperature, spin lattice relaxation becomes a limiting factor to coherence times of nanocrystal electron spin qubits [146]. Incorporating colloidal QDs into rigid structures could have the benefit of minimizing spin lattice relaxation, potentially enabling room

temperature spin coherence. Furthermore, enhancing the optical properties through the use of photonic crystals may improve the feasibility of utilizing interactions between the excitons and magnetic ions for the initialization and readout of the electron spin qubits (Chapter 1.3.3).

2D photonic crystals are simple to design and provide a structure suitable for incorporating nanocrystals. 2PP micromachining was chosen because it has the potential to provide a cheap, fast method of fabricating multiple structures (< 3 minutes for each microcavity). Furthermore, the manufacturers of the 3D micro-printer have recently claimed the ability to fabricate features down to 100 nm [110] which would provide adequate resolution for our purposes.

5.1 Design and fabrication of photonic cavities

The objective of this work was to initially design a photonic crystal in order to establish the feasibility of the 3D printing technique. Therefore, we designed a polymer cavity optimized for undoped PbS QDs (E_g ~ 1 eV). The use of polymer rods (n ~ 1.48) in air (n ~ 1) limits the refractive contrast that can be achieved (Equation 1.6), and therefore restricts the Bragg reflection, but it allows us to 'print' the structure directly. If successful, this technique could be used to fabricate a template for a highly refractive replica for improved enhancement, e.g. infiltration of the polymer structure with a titanium-IV-iospropoxide precursor in a He atmosphere followed by exposure to moisture in air to form a solid TiO_2 replica with n ~ 2.5 [109].

The dimensions of the photonic crystal were determined using the 'gap recipe/map' for a 2D triangular lattice of dielectric rods as set out in the book: 'Photonic Crystals: Molding the Flow of Light'[147]. A triangular lattice was chosen as this allows for slightly larger dimensions compared to the alternatives. The 'gap recipe' determines the optimal ratio of rod radius, r, to lattice constant, a, that maximises the gap size as a function of index contrast, n_{hi}/n_{lo}. For a photonic crystal with an index contrast of,

n_{hi}/n_{lo} = 1.48, corresponding to polymer rods (*IP-L* photoresist [110]) in air, the optimal ratio of radius to lattice constant is, *r/a* = 0.28. This corresponds to the centre of a large TM band gap at $\omega a/2\pi c = a/\lambda = 0.3$. At a wavelength, $\lambda = 1080$ nm, consistent with the peak PL emission for PbS QDs, we were able to obtain optimal dimensions of, *r* = 100 nm, *a* = 350 nm and *height* = 2*a* = 700 nm, from which the structure can be completely determined (Figure 5-1). Finally, removing a single rod from the centre produces a photonic crystal design with a cavity of length, *l* = 500 nm, surrounded by a periodic index contrast causing Bragg reflection of the emission of embedded nanocrystals.

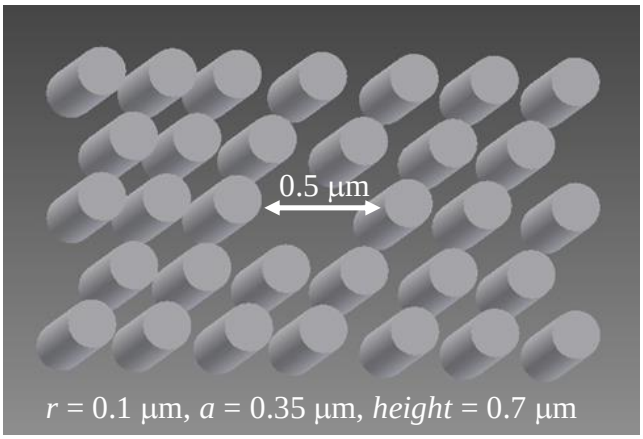

Figure 5-1 Diagram showing the photonic crystal design with a cavity of length, *l* = 0.5 μm and polymer rods of radius, *r* = 0.1 μm, lattice constant, *a* = 0.35 μm and *height* = 0.7 μm.

The photonic crystals were fabricated, by Mr Andrew Knott, using 2PP micromachining (Chapter 2.5). Figure 5-2a shows a 100× optically magnified image of one of our attempts to fabricate a photonic crystal according to our calculation of optimal dimensions. Since the polymer is transparent to white light, it is difficult to achieve good resolution in an optical microscopy image and our attempts to produce SEM images resulted in damage to the polymer. However, we would have expected a cavity of *l* ~ 0.5 μm to be clearly visible at this magnification and the lack of a discernible cavity suggests that a photonic crystal of this size is

beyond the capabilities of the *Nanoscribe* system and therefore, the structures were discarded.

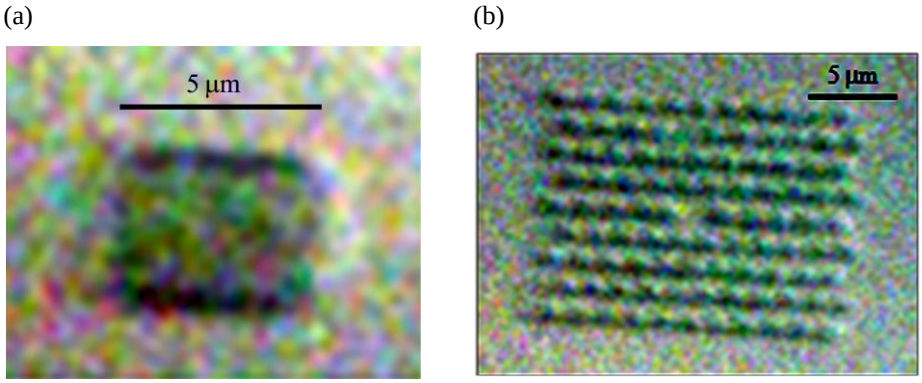

Figure 5-2 2PP micromachined photonic crystal designed to have a cavity of length, l = 0.5 μm (a) and fabricated with a cavity of length, l ~ 1μm (b).

Figure 5-2b shows an image of a larger photonic crystal, a = 1600 nm, with rods fabricated as small as the system would allow (r ~ 500 nm), i.e. resulting from a single laser pulse. The cavity is of approximate length, l ~ 1 μm, which is approximately equivalent to the wavelength of the nanocrystal peak emission and which should therefore sustain a standing wave.

5.2 Micro-PL mapping

PbS colloidal QDs were drop-cast onto the photonic crystals and allowed to dry prior to performing micro-PL mapping. The QDs used for the initial tests were undoped in order to minimize any complicating factors. A 100× objective was selected to allow mapping with resolution of ~0.5 μm, and an image was acquired with the CCD camera. A 6 μm × 6 μm area centred over the cavity was defined (green square: Figure 5-3a). The area was divided into 49 equally spaced data points and each point was excited with a He-Ne laser (Chapter 2.5). Imaging was done from the substrate side to enable imaging of the QDs in the cavity and, where possible, avoid emission

from QDs on the surface. The result of the mapping are shown in the inset of Figure 5-3a displaying a clear optical enhancement around the area of the cavity. The cursor spectrum with a peak at $\lambda \sim 1040$ nm is shown alongside. The experiment was then successfully repeated with 25 data points over the central area of a second photonic crystal of similar dimensions (Figure 5-3b).

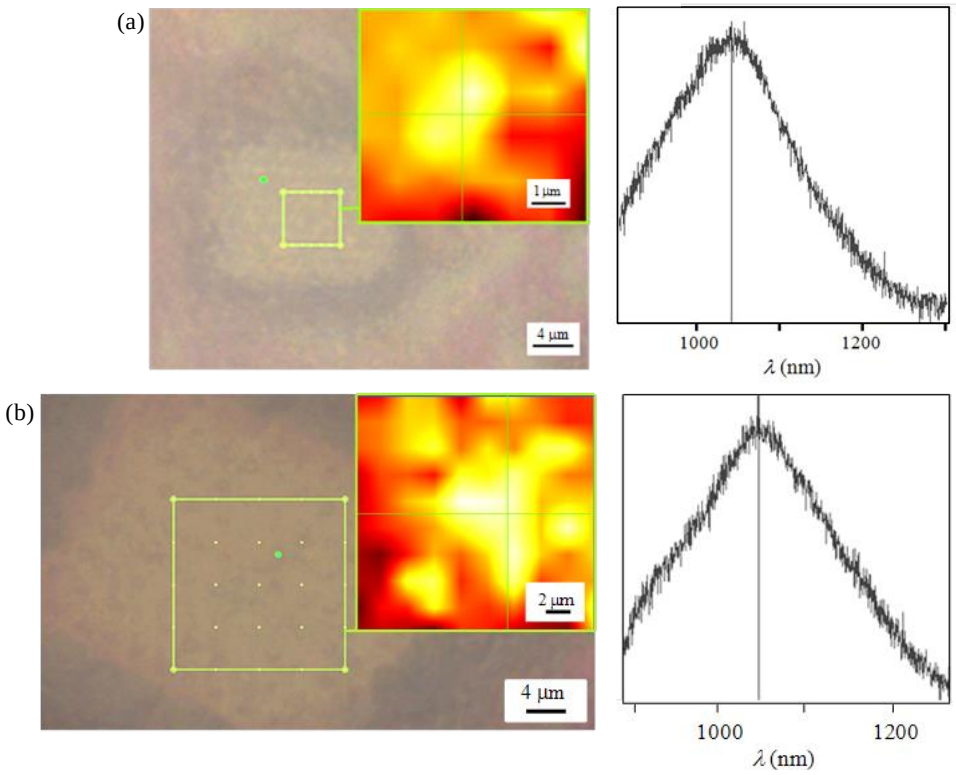

Figure 5-3 (a) CCD image of the photonic crystal with the XY-map area defined by the green square with corresponding cursor PL spectrum. Inset: Result of the micro-PL mapping. (b) Experiment repeated with a second photonic crystal of the same dimensions.

5.3 Discussion

The resolution we were able to obtain with the 2PP fabrication was poorer than expected and it seems unlikely that it could be improved sufficiently to fabricate structures at the desired scale. Fabricating larger structures with better resolution also presents problems. As the volume of the cavity is increased, resonant frequencies become less sparsely distributed [148]. As such, it may become impossible to isolate a single resonance in a larger structure.

The second structure we printed (Figure 5-2b) pushed the *Nanoscribe* system to its limits but was still a considerable compromise in terms of size and accuracy. As well as inaccuracy in terms of the dimensions and spacing of the rods there was a further inaccuracy in the shape, i.e. a single laser pulse is likely to produce conical, rather than cylindrical, features; as such, a meaningful characterization of the final structure without far better images is not possible. The PL-map does however show a clear, if small, enhancement which is encouraging considering the inaccuracies of the fabrication. However, it is clear that an alternative technique, such as, ECR etching (Chapter 1.3.4) will have to be considered for this work to proceed further.

Chapter 6

Surface sensing of QDs by electron spins

This chapter reports the use of magnetic resonance techniques for sensitive probing of the QD surface and environment. We reveal inequivalent proton spin relaxations of the capping ligands and solvent molecules, strengths and anisotropies of the Mn-nuclear spin interactions, and Mn-nuclei distances with ~1 Å sensitivity. These findings demonstrate the potential of magnetically doped QDs as sensitive magnetic nano-probes and the use of electron spins for surface sensing.

6.1 Introduction

The design of nanocrystals through the controlled incorporation of paramagnetic impurities or modification of the surface by capping ligands requires analytical techniques which have sufficient sensitivity to resolve single atoms and to probe surface properties. Both the position of the impurities in the host crystal lattice and their interaction with the surrounding environment (e.g. capping ligands, solvent, etc.) are central to the design of the nanocrystals and can be exploited in several

applications spanning optoelectronics [149-151] and medical imaging. For example, multi-modal imaging could be enabled by doping QDs with paramagnetic centres [20]. NMR and ESR stand out as spectroscopic techniques that can resolve the structure and functionalities of systems that lack long-range order (e.g. proteins and biological membranes), which can be inaccessible with techniques like X-ray diffraction (XRD). To date, NMR has been employed to probe the structure and surfaces of colloidal metal nanoparticles [152] and quantum dots (QDs) [153-156]. Solid state NMR has been used to probe the incorporation of impurities at low concentration [157]. However, the preparation of solid-state samples involves the precipitation of the nanoparticles, which can affect the nanocrystal surface. In contrast, solution proton-NMR (^{1}H-NMR) is a non-destructive technique [152, 155, 158-160] and could be equally informative. Indeed, spectral broadening and proton spin relaxations studies have been used to investigate the interfacial electronic structure in colloidal QDs [161] as well as surface charge transfer processes [162, 163].

ESR is less commonly used than NMR because it relies on the presence of unpaired electrons. This limitation can be overcome by doping the nanocrystals with paramagnetic centres. The detection of electron spin impurities by pulsed-ESR methods, combined with theoretical modelling, enables the determination of structural and dynamical properties with nanosecond resolution [164]. Pulsed-ESR has become a standard approach employed to characterize proteins using site-directed mutagenesis and spin labelling [165, 166], nanocrystals doped with magnetic impurities [129, 167] or radiation defects [168, 169], as well as a technique for the detection of NV-centres in diamond as bio-markers [170], nanoscale sensors [171] and spin qubits [172].

This work demonstrates the combined use of ^{1}H-NMR and pulsed-ESR in magnetically doped nanocrystals, enabling sensitive probing of the QD surface and environment. We probe the location of Mn^{2+} impurities in colloidal PbS QDs and show that the interaction of single impurities with nearby protons provides a tool for discriminating between inequivalent proton spin relaxations of surrounding molecules, i.e. capping ligands and solvent molecules. Furthermore, we have determined the strength and anisotropies of the interactions between surface Mn

electron spins and nearby nuclear spins, as well as the Mn-nuclei distances with a sensitivity of ~1 Å. As such, nanocrystals doped with Mn-ions close to the QD surface provide a nanostructure with magnetic properties that are strongly sensitive to its environment. These results are relevant for future exploitation of magnetically doped QDs as sensitive magnetic nano-probes for use in medical imaging [20], as well as providing insight into the sources of decoherence of electron spins, relevant for application as qubits [50, 146].

6.2 Materials

PbS:Mn colloidal QDs were synthesised in aqueous solution. They were stabilised with a mixture of 1-thioglycerol (TGL) and 2,3-dimercapto-1-propanol (DTG), and the pH was controlled using Triethylamine (TEA) (Chapter 2.1). The QD solutions were dialysed prior to NMR/ESR studies to remove excess ligand molecules and free Mn^{2+} ions. NMR experiments (Chapter 2.4.1) were carried out on samples dispersed in H_2O:D_2O (1:9 v/v) and with Mn concentrations of 0 %, 0.01 %, 0.03 % and 0.1 %.

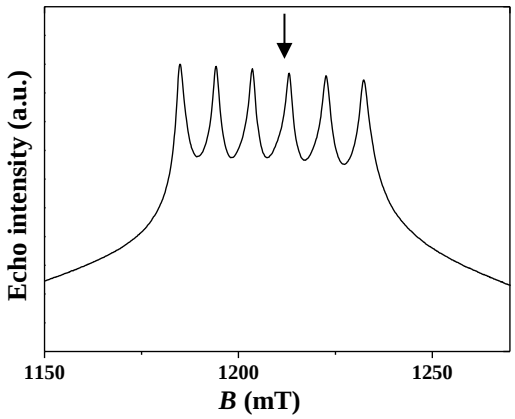

Figure 6-1 Echo field swept spectrum recorded at Q-band (ν_{mw} = 33.85 GHz) for D-PbS:Mn solid state sample with Mn concentration of 0.03%. The arrow indicates the magnetic field position (B = 1.211 T) at which the pulsed-ESR experiments were conducted.

Pulsed-ESR studies were performed on a PbS:Mn powder sample with Mn concentrations of, Mn = 0.03 % and Mn = 0.05 %, i.e. ~1 Mn^{2+} ion per QD. This provides a good compromise between long spin relaxation times (T_M ~ 1 μs and T_1 ~ 200 μs at T = 5 K) and a large signal/noise ratio [173]. ESEEM and ENDOR

experiments (Chapter 2.3.2) were conducted on protonated and deuterated (D-PbS:Mn) solid state samples and performed at Q-band (ν_{mw} = 33.85 GHz) with a fixed field corresponding to the fourth hyperfine peak (B = 1.211 T) of an echo field swept spectrum (Figure 6-1). This corresponds to the m_I = -1/2 nuclear line of the m_s = +1/2 ↔ -1/2 transition. The ESEEM and ENDOR spectra were simulated using *Easyspin* software [174].

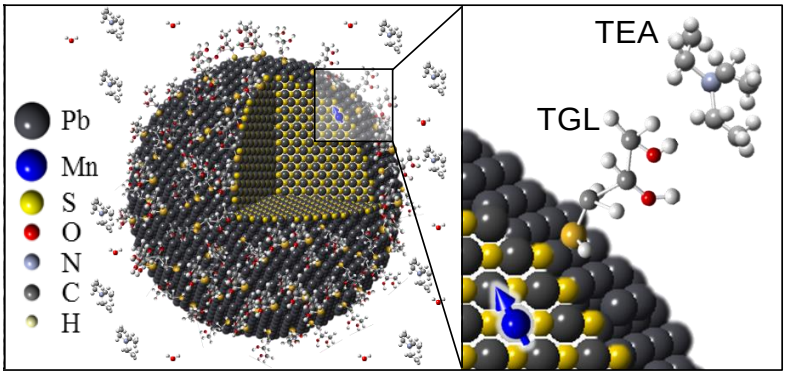

Figure 6-2 Schematic of a PbS:Mn QD and zoom of a surface Mn ion interacting with the TGL capping ligands and TEA solvent molecules in water solution.

The schematic in Figure 6-2 shows a PbS QD with a Mn-atom near its surface, a TGL ligand, which binds to the QDs via the SH-group, and a TEA molecule. ^{1}H-NMR spectra were measured in order to probe the QD surface and environment, and were compared to those of free TGL and TEA molecules.

6.3 ^{1}H-NMR

Two intense peaks centred at δ = 1.24 and 3.12 ppm are observed in the ^{1}H-NMR spectrum of PbS QDs in solution (Figure 6-3). They comprise a triplet and quartet, respectively, with a ratio between the integrated areas of 1.44. These peaks are similar to the triplet at δ = 0.89 ppm and the quartet at δ = 2.34 ppm observed in the ^{1}H-NMR spectrum for the TEA solvent molecule. However, the TEA peaks in the ^{1}H-NMR spectrum of PbS are shifted downfield compared to the TEA reference

spectrum (Figure 6-4) thus suggesting a deshielding of the TEA protons in presence of the QDs. The peak assignment is supported by the analysis of their integrated

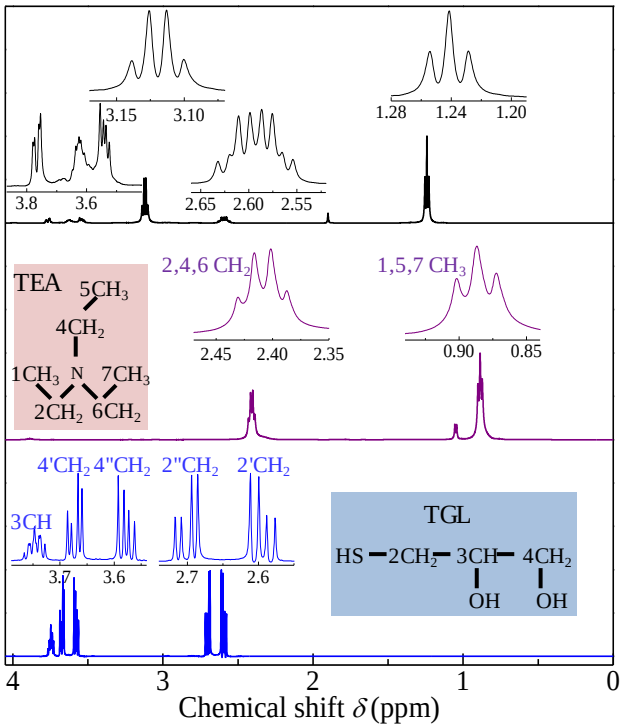

Figure 6-3 Overview of ^{1}H-NMR spectra for solutions of undoped PbS QDs, TEA and TGL molecules. Insets are skeletal formulas for TGL and TEA.

areas. For TEA, the triplet and quartet have intensity ratios 1:2:1 and 1:3:3:1, respectively. This results from the spin-spin coupling between the equivalent protons of the 2, 4, and 6CH_2-groups and those of the 1, 5 and 7CH_3-groups, and vice-versa. In the ^{1}H-NMR spectrum of PbS QDs, the ratio of the integrated intensities of the TEA peaks is 1.48, which is very close to the expected 3/2 ratio due to equivalent protons of the CH_3 and CH_2 groups.

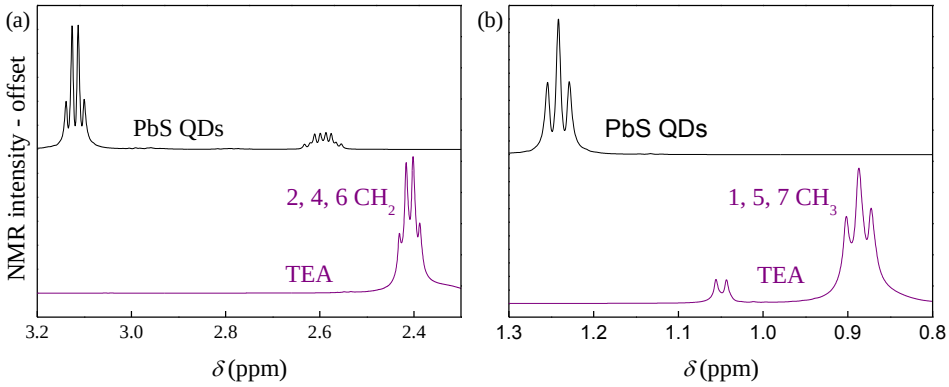

Figure 6-4 TEA peaks shifted downfield in PbS QDs. (a) 2, 4 and 5 CH_2 peaks and (b) 1, 5, and 7 CH_3 peaks.

A further four sets of low intensity multiplets centred at δ = 2.59, 3.55, 3.61 and 3.78 ppm are observed in the QD spectrum. These peaks resemble those of the NMR spectrum measured for the TGL ligands. In particular, the peak at δ = 2.59 ppm is close to the quartets of the two inequivalent 2' and 2" CH_2-groups centred at δ = 2.64 ppm. In the ^{1}H-NMR spectrum of PbS, the two quartets are shifted upfield and their separation is decreased (Figure 6-5b), and therefore suggests that the $2CH_2$-groups tend to be equivalent in the presence of the QDs. We assign the two quartets at δ = 3.55 and 3.78 ppm to the inequivalent 4' and 4" CH_2-groups of the TGL ligands. The separation between them increases with respect to the TGL spectrum and their central positions shift downfield indicating that the $4CH_2$-groups became more inequivalent in presence of the QDs (Figure 6-5a). The peak at δ = 3.61 ppm is assigned to the 3CH-group of the TGL ligand. This was shifted upfield and shows an almost unresolved multiplet due to the close chemical shift of the two multiples resulting from the interaction between the CH groups and the inequivalent $2CH_2$ and $4CH_2$ groups (Figure 6-5a). We also note that the ratio between the integrated intensities for the peaks assigned to 3CH, $2CH_2$ and $4CH_2$-groups followed the expected 1:2:2 ratio. We observe a broadening of the lines for the QD sample which would be expected for molecules attached to the QD surface [159]. We note that the peak at δ = 1.9 ppm (Figure 6-3) is due to residual acetate groups and there is no evidence of resonance peaks of DTG in the spectra recorded for the QD samples.

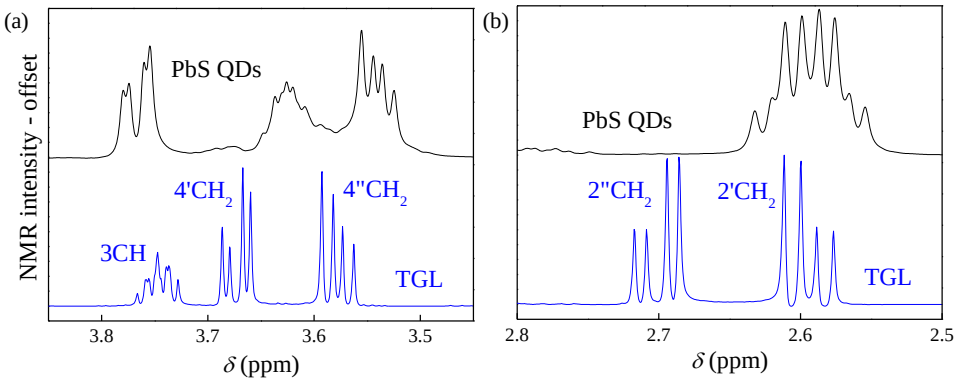

Figure 6-5 TGL peaks are shifted in PbS QDs. (a) The 3CH peak is shifted upfield becoming almost unresolved in the QDs, 4' and 4" CH2 peaks are shifted downfield and separation is increased in the QDs, and (b) 2', and 2" CH2 peaks are shifted upfield in the QDs and the separation is decreased.

Figure 6-6 shows the spectrum for a 2D ^{1}H–^{13}C heteronuclear single quantum coherence (HSQC) experiment. This supports the assignment of the ^{1}H-NMR resonances. The signals at δ^{C} = 8 ppm and 46 ppm, correspond to the TEA CH_3 and CH_2-groups, whereas the peaks at δ^{C} = 25 ppm, 75 ppm and 65 ppm are assigned to the 2-CH_2, 3-CH and 4-CH_2 groups of the TGL molecule, respectively.

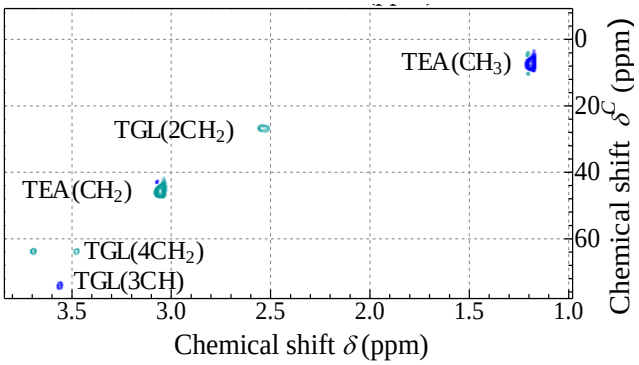

Figure 6-6 HSQC spectra of TGL and PbS QDs. The peaks assigned to the CH-groups of TEA and TGL molecules for the PbS QDs indicated. The different colour tone is used to distinguish between odd and even CH-groups.

The incorporation of Mn-ions into the QDs modifies the ^{1}H-NMR spectra (Figure 6-7). With increasing Mn-content up to 0.1%, the characteristic resonance peaks of

TEA (Figure 6-7a) broaden and shift upfield with greater chemical shifts observed for protons on CH_2-groups ($\Delta\delta$ = -0.08 ppm). More significant changes are observed for the resonant peaks of TGL (Figure 6-7b). All ^{1}H-NMR peaks broaden and shift downfield starting from a Mn concentration as low as 0.01%. The most pronounced changes are observed for the 2'CH_2 (δ = 2.54 ppm) and 2''CH_2-groups (δ = 2.65 ppm), where their peaks broaden with increasing Mn concentration, becoming undetectable at Mn = 0.1%. These results suggest that the spin relaxation rates of the protons of the capping ligands and solvent molecules increase due to the magnetic dipolar interactions with the Mn-ions.

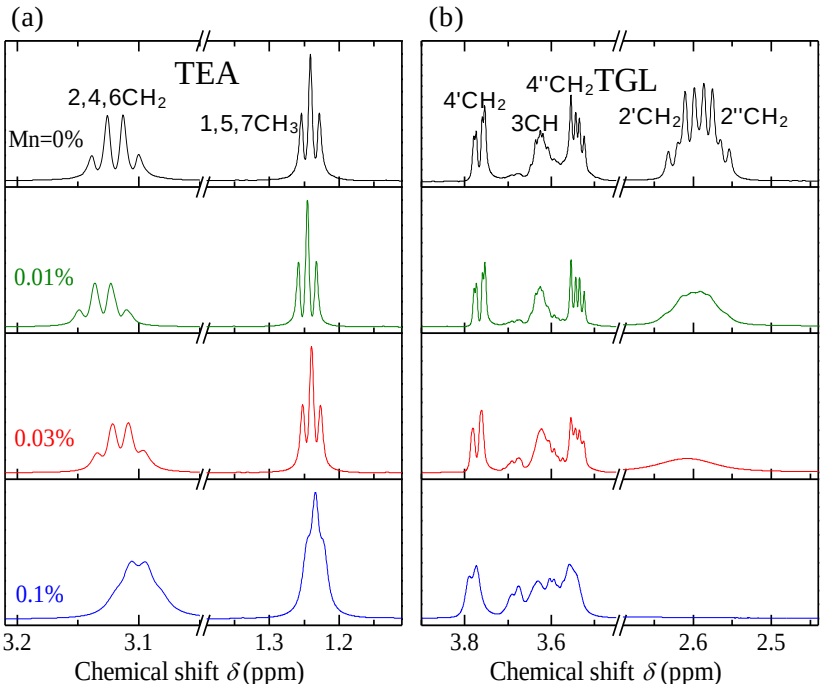

Figure 6-7 (a) ^{1}H-NMR spectra for PbS QDs undoped and doped with Mn concentrations of 0.01 %, 0.03 % and 0.1 %. Peaks corresponding to TEA (a) and TGL (b) CH-groups are indicated.

Figure 6-8 provides evidence that the Mn–^{1}H(TGL) interactions investigated are related to TGL molecules coordinated to the QD. The two plots show that for the same Mn concentration, we observe a larger degree of spectral broadening for both the TGL (Figure 6-8a) and TEA (Figure 6-8b) ^{1}H-NMR peaks in a control sample of $MnAc_2$ mixed with free TEA and TGL molecules.

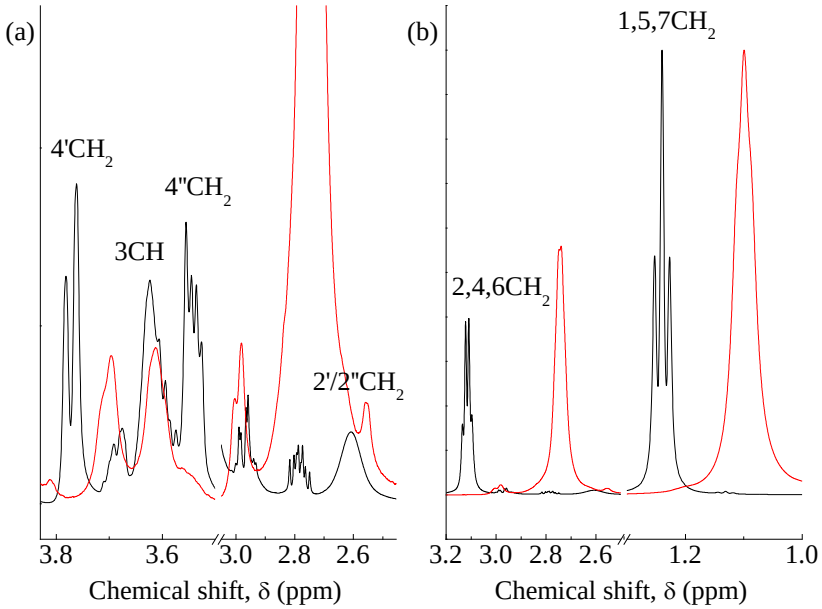

Figure 6-8 Comparison between 1H- MR spectra for TGL (a) and TEA (b) molecules free in a solution containing $MnAc_2$ molecules (red curve) and bonded to Mn^{2+} - doped PbS QDs (black curve) with Mn concentration, Mn = 0.03%.

The proton spin-lattice relaxation rate constant, $1/T_1$, for each CH-group of TGL (Figure 6-9a) and TEA (Figure 6-9b) molecules can be estimated from the analysis of ^{1}H-NMR spin-lattice relaxation experiments (see sequence, Chapter 2.4). We observe a general increase of $1/T_1$ with increasing Mn content. The relaxation rate in TGL molecules increases by up to 100× and is different for each CH-group: $1/T_1(2CH_2) > 1/T_1(3CH) > 1/T_1(4CH_2)$. In addition, for each CH-group, $1/T_1$ increases linearly with increasing Mn-content. In TEA, the relaxation rate for proton spins of CH_2- and CH_3-groups increases by up to 10× following the Mn-incorporation. The systematic decrease of $1/T_1$ along the C-chain of TGL molecules confirms the binding of the TGL to the QD surface at the –SH site (Figure 6-9a), while the slower proton T_1 relaxation for TEA indicates efficient passivation of the QDs with capping ligands, which screen the interactions of the Mn spins with the TEA molecules (Figure 6-9b).

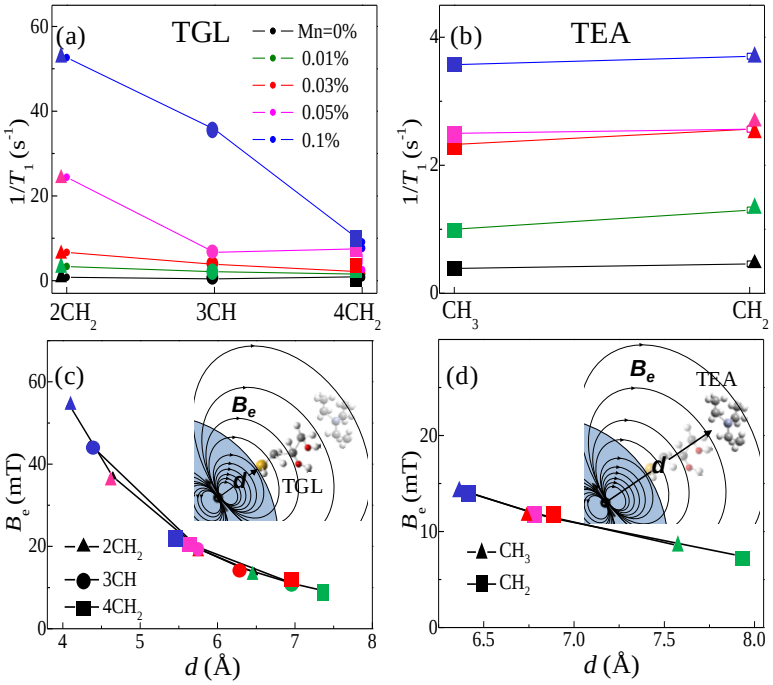

Figure 6-9 ^{1}H-NMR relaxation rates ($1/T_1$) for the TGL (a) and TEA (b) CH-groups of PbS:Mn QDs with Mn concentrations: 0 %, 0.01 %, 0.03 %, 0.05 % and 0.1 %. Calculated Mn induced magnetic fiels (B_e) and average distance, d between Mn and CH groups of the TGL (c) and (d) show the distance,*d* between Mn-spins and protons of TGL and TEA molecules and the magnetic field (B_e) generated by the Mn-spin impurity.

The proton spin relaxation rate depends on the distance, *d*, between the paramagnetic impurities and the proton spin, and the strength of the magnetic field generated by the paramagnetic impurities, B_e, which is defines as:

$$B_e = \frac{g\mu_0\mu_B\sqrt{S(S+1)}}{2\pi d^3} \qquad (6.1)$$

where *S* is the electron spin quantum number.

In the QD's reference frame, the position of Mn and proton spins of the TGL molecule, and hence the vector **SI** joining the electron and nuclear spins, is fixed and the hyperfine constant *A* is invariant under rotation. Neglecting the angular dependence of the vector **SI** with respect to the external magnetic field, the nuclear relaxation rate $1/T_1$ is given by the equation [24]:

$$\frac{1}{T_1} = \frac{2}{5}\frac{1}{\tau}\left(\frac{B_e}{B_0}\right)^2, \qquad (6.2)$$

where τ is the electron spin relaxation time and B_0 is the applied magnetic field.

For Mn ions incorporated in QDs, τ is of the order of 10^{-6} s at room temperature [175]. Thus, we can estimate the magnetic field B_e experienced by each inequivalent proton of TGL and the Mn-CH distances for each Mn concentration. Approximate Mn-CH distances for TEA were calculated in the same way by ignoring molecular rotation. The results along with the measured values of $1/T_1$ for different CH-groups of TGL and TEA are shown in Figure 6-9c and d, respectively.

For each Mn concentration, the TGL $2CH_2$-group is always closer to the Mn ions than 3CH and $4CH_2$ (Figure 6-9c). With increasing Mn content, the average Mn-^{1}H distance decreases while B_e increases for all the inequivalent protons. The calculated distance of Mn from the $2CH_2$-group is $d \sim 4$ Å for Mn = 0.1% and $d \sim 6.5$ Å for the lowest concentration Mn = 0.01%. This implies that Mn ions are located near the QD surface at a distance $d \sim 4$ - 7 Å. For TEA groups (Figure 6-9d), we find that for each Mn concentration, the Mn-^{1}H distance is always larger or comparable to the distance between Mn spins and TGL $4CH_2$-groups. For the lowest concentrations, i.e. Mn = 0.01%, the Mn-spin sensitivity to distant TEA protons extends up to $d \sim 8$ Å.

6.4 Pulsed-ESR

Although ^{1}H-NMR is very sensitive to ^{1}H-relaxation induced by surrounding electron spins, it only provides an indirect probe of the location and concentration of Mn ions in the QDs. More generally, the NMR sensitivity is limited by the weak nuclear magnetic moments and fast relaxation times for nuclear species with an electric quadrupole moment making, for instance, ^{55}Mn- and ^{207}Pb-NMR transitions undetectable. ESR has the advantage over NMR of much greater sensitivity due to the larger energy level separation and population difference. In pulsed-ESR, nuclear spin transitions are detected indirectly, either by modulation of the electron spin echo

signal induced by surrounding nuclear spin fluctuations, i.e. ESEEM, or by saturation or inversion of an ESR transition followed by rf excitation of nuclear spin transitions, i.e. ENDOR (Chapter 2.3.2). ESEEM and Mims-ENDOR are more sensitive to low-range nuclear frequencies (typically below ~ 10 MHz), whereas Davies-ENDOR is more sensitive in the mid-high frequency range [125].

The ^{2}H-ESEEM spectrum for deuterated PbSMn (Mn = 0.03%) of Figure 6-10a was simulated with the following spin-Hamiltonian:

$$\hat{H} = g\mu_B \vec{B} \cdot \hat{S} + \hat{S} \cdot A \cdot \hat{I} + \hat{I} \cdot Q \cdot \hat{I}, \qquad (6.3)$$

where the first term is the Zeeman interaction, the second term is the hyperfine coupling and the latter term is the nuclear quadrupole interaction with an axial nuclear quadrupole coupling e^2Q/h, where e is the electric charge. The results of the calculations are reported in Table 6-1. The spectrum reveals a resonant peak centred at the Q-band Larmor frequency of deuterium ^{2}H, $\omega(^2\text{H})/2\pi$ = 7.9 MHz, as well as combination frequencies: $\omega_\alpha - \omega_\beta$ and $\omega_\alpha + \omega_\beta$, and several satellite peaks. The ^{2}H-ESEEM signal can be ascribed to Mn spins interacting via dipolar coupling with ^{2}H of the TGL bound to the QDs. The ^{2}H-ESEEM spectrum is simulated by considering a Mn spin (S = 5/2) interacting with a ^{2}H nuclear spin (I = 1) with hyperfine coupling constants A_{iso} = 0.16 MHz and T = 0.5 MHz, where A_{iso} and T are the isotropic and anisotropic contributions to the hyperfine coupling interactions in spherical coordinates, and an axial nuclear quadrupole constant, i.e. e^2Qq/h ~ 0.3 MHz. Similar absolute values for e^2Qq/h were previously reported for deuterium [176].

The larger anisotropic contribution to the hyperfine interaction suggests that the dominant interaction between Mn and ^{2}H is dipole-dipole. In the point-dipole approximation, the electron-nuclear dipolar couplings (ω_{dd}) are distributed across the $\theta = 0$ and $\pi/2$ angles between the $\mathbf{B_0}$ vector and the **SI** inter-distance vector according to the equation [125]:

$$\omega_{dd} = \frac{\mu_0 g_S g_N \mu_B \mu_N}{2hd^3}(3\cos^2\theta - 1). \qquad (6.4)$$

If we convert the spherical form of the hyperfine tensor obtained from the ESEEM simulation to the Cartesian form, we obtain the principle values of the *A* tensors of $|A_x| = |A_y| = 0.34$ MHz and $|A_z| = 1.16$ MHz. The $A_{x/y}$ value relates to the frequency difference between the two singularities corresponding to $\theta = 90°$, from which, by neglecting the small quadrupole coupling [28], we can use Equation 6.4 to estimate the Mn-^{2}H distance as, $d \sim 6$ Å.

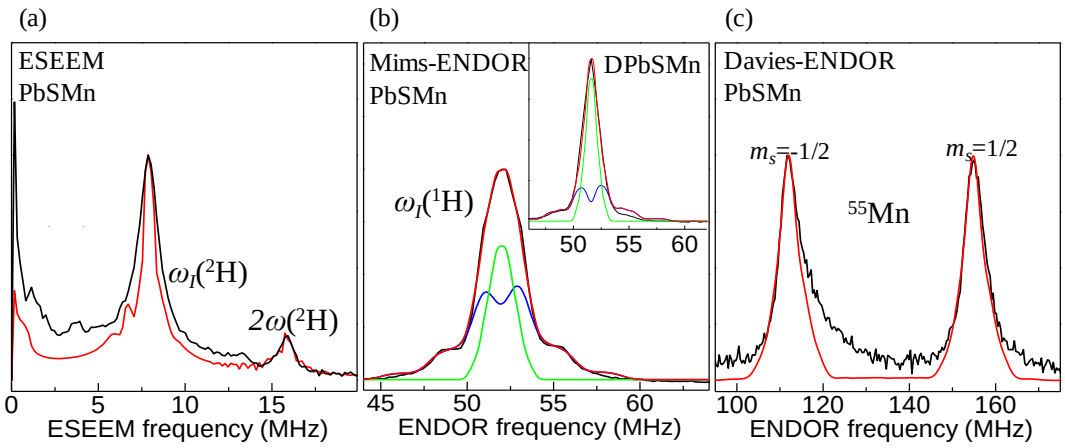

Figure 6-10 ^{2}H-ESEEM (a) ^{1}H-ENDOR-Mims (Inset: ^{1}H-ENDOR-Mims for a sample in deuterated solution) (b) and ^{55}Mn-Davies-ENDOR (c) Q-band spectra at T = 5 K for the PbS:Mn QD sample along with the simulations (green curve = matrix line, blue curve = ^{1}H and ^{2}H interacting with Mn ions, red curve = total contribution). The ^{1}H-Mims-ENDOR spectrum has been inverted along the intensity axis.

Table 6-1 pulsed ESR simulation parameters for ^{1}H and ^{2}H.

	Sample	Mn (%)	A_{iso} (MHz)	T (MHz)	e^2Q/h (MHz)	*lwENDOR* (MHz)	Weight *(%)*
^{2}H (bound)	DPbS	0.03	0.16 ± 0.1	0.5 ± 0.1	0.3 ± 0.1	-	-
^{1}H (bound)	DPbs	0.03	0.2 ± 0.1	1.3 ± 0.1	-	0.5	25
^{1}H (matrix)	DPbS	0.03	0	0.2 ± 0.1	-	0.28	75
^{1}H (bound)	PbS	0.05	0.27 ± 0.05	1.3 ± 0.1	-	0.8	70
^{1}H (matrix)	PbS	0.05	0	0.4 ± 0.1	-	0.4	30

The same Hamiltonian (Equation 6.3), with the omission of the nuclear quadrupole interaction, has been used for ^{1}H-ENDOR spectra for protonated PbS:Mn QDs and deuterated PbS:Mn QDs. The spectra reveal additional resonances at ν = 51.5 MHz (Figure 6-10b), 114 MHz and 157 MHz (Figure 6-10c). The latter two resonances are detected by Davies-ENDOR and are ascribed to Mn electro-nuclear spin transitions within the m_s = -1/2 and m_s = +1/2 manifolds in the strong coupling

regime ($2|\omega_I| < |A|$) with the doublet centred at $A/2$. The obtained value of A = 267 MHz [124, 146] is consistent with the simulation of the continuous X-band CW ESR spectrum for solid state PbS:Mn (Mn =0.05%) at T = 250 K (Figure 6-11). The spectrum was simulated with the following Hamiltonian:

$$\hat{H} = g\mu_B\vec{B}\cdot\hat{S} + \hat{S}\cdot A\cdot\hat{I} + D\hat{S}_z^2\left(-\frac{S(S+1)}{3}\right) + E\left(\hat{S}_x^2 + \hat{S}_y^2\right), \quad (6.5)$$

where g = 1.99, A = 267.2 MHz, D = 474.5 MHz and E = 90.5 MHz. The linewidth was simulated assuming a D strain of 305 MHz and intrinsic Gaussian FWHM of 0.9 mT. The sizeable D and E parameters suggest that Mn ions are surrounded by an axial crystal field with small planar anisotropy likely due to their proximity to the nanocrystal surface.

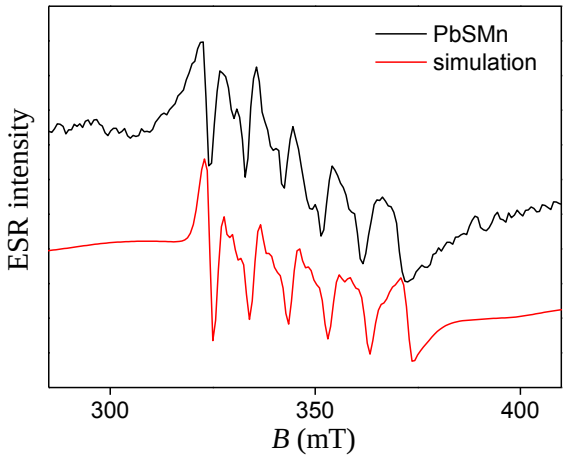

Figure 6-11 CW-ESR spectrum at X-band for PbSMn (Mn =0.05%) solid state (black curve) and simulation (red curve).

From first order perturbation theory [177], the separation Δν between the Mn nuclear resonance peaks (Figure 6-10c) should be twice the Larmor frequency of Mn, i.e. $2\nu(^{55}\text{Mn})$ ~ 25 MHz. The larger experimental value of $\Delta\nu$ ~ 43 MHz is similar to that reported for ^{55}Mn-complexes [177] and ascribed to second order hyperfine interaction contributions [177, 178] according to:

$$\Delta\nu = 2g_N\mu_N B + \frac{A^2}{\nu_0}[S(S+1) - m_s^2] - \frac{A^2}{\nu_0^2}[S(S+1) - m_s^2] - O(A^3). \quad (6.6)$$

By substituting A = 267 MHz, ν_0 = 34 GHz, S = 5/2 and m_s = 1/2 , the summation of the first term (~ 25 MHz) and the second term (~ 17 MHz) accounts for $\Delta\nu$ ~ 42 MHz, which is in agreement with the experimental data. The third term can be neglected given that $\nu_0^2 >> A^2$.

Finally, the peak at ν ~ 51.5 MHz resolved by Mims-ENDOR (Figure 6-10b) is centred near to the natural Larmor frequency of ^{1}H at B = 1.211 T with doublets symmetrically distributed. The spectrum was simulated by considering a contribution of Mn^{2+} ions interacting with protons of the TGL bound to the QDs with A_{iso} = 0.27 MHz and T = 1.3 MHz, and a contribution of Mn ions interacting with residual matrix protons, i.e. TEA and H_2O, with A_{iso} = 0 MHz and T = 0.4 MHz. The estimated Mn-TGL ^{1}H distances along the principal axis are: d = ~ 8 Å, while for Mn-matrix ^{1}H, we obtain a lower bound of, d ~ 9 Å.

6.5 Discussion

^{1}H-NMR and pulsed-ESR methods enable the observation of electron-nuclear spin interactions at the surface of the QDs, providing complementary information on the position and environment of a single paramagnetic centre in a nanocrystal. A single Mn^{2+} impurity in colloidal PbS QDs experiences a rhombic environment as a result of its proximity to the disordered QD surface. We have estimated the hyperfine dipolar interactions between the Mn-ions and the nuclei of the QDs capping ligands and solvent molecules, and the relative distances. Our findings demonstrate that Mn^{2+}-spins located near the QD surface (d < 7 Å) act as sensors of proton spins located at the QD surface with ~1 Å sensitivity. Therefore, as little as 1 Mn ions per QD is sufficient to induce a fast relaxation of the proton spins of the capping ligands as well as of the solvent molecules: a 60-fold and 10-fold enhancement for the protons of the capping ligands and solvent molecules, respectively. These features are relevant for the exploitation of Mn-doped colloidal QDs as imaging labels for combined fluorescence and magnetic resonance imaging. We note that at low Mn concentrations the optical properties of QDs are preserved [179]. Also, the

interaction of Mn-ions with surface protons presents a source of decoherence for electron spins which is relevant for applications such as electron spin qubits [175, 180]. Our findings indicate that Mn-^{1}H dipolar interactions reach a plateau at distances > 6 Å, thus providing a guide for developing QD encapsulation techniques to increase the electron spin coherence times. As such, combined pulsed-NMR and ESR studies of magnetically doped nanocrystals may pave the way for the use of electron spins as surface sensors. This will ultimately enable the design of multi-functional QDs for practical applications.

We envisage that pulsed-ESR could also be sensitive to inequivalent protons [181] and different Mn sites, which in our experiments are masked by the linewidth broadening due to simultaneous excitation of electron-nuclear transitions along different orientations. This sensitivity will provide more information about the distribution of Mn sites and the distances between a Mn^{2+} ion and the surrounding inequivalent protons. For instance, these could be achieved, by pulsed-ESR experiments either on ordered arrays of QDs or a single QD. Some progress in these directions has recently been achieved by pulsed-ESR experiments on individual atoms on a surface [182]. Alternatively, more sophisticated pulsed-ESR methods, which greatly increase the resolution of ENDOR spectra, and hence enable the distinction between inequivalent nuclear spins, could be implemented [183].

Chapter 7

Developing magnetic resonance instrumentation to study paramagnetically doped materials with mixed magnetic phases

This chapter seeks to explore a means of characterizing mechanisms responsible for the functionality of paramagnetically doped materials. The development of instrumentation to identify and quantify interactions between paramagnetic and ordered magnetic phases is described. A probe was designed and built with a fast response time and with the aim of facilitating fast field jump experiments to identifying interactions between the different magnetic phases by correlating the response of a sample to mw irradiation with its response to a field jump.

7.1 Introduction

For paramagnetic metal ions at non-cryogenic temperatures, EPR relaxation times can be so short that it becomes impossible to study them with conventional pulsed

techniques. Traditional magnetic resonance techniques use the same "antenna" for high power excitation as well as detection of very small magnetic fields from the precessing spins. As such, simultaneously exciting and detecting spins is not possible. Following an excitation pulse, it is necessary to have a period of deadtime before the signal can be measured. Spectral information may be obtained by cooling the sample to liquid helium temperatures; however, this is not satisfactory when studying relaxation times, as their temperature dependence provides important information about the nature of the interaction responsible for the relaxation. LOD EPR provides a complementary technique in which the signal depends purely on M_z and the longitudinal relaxation of a sample. Using this technique, data can be acquired even while the spins are being excited.

7.3 $KCr_3(SO_4)_2(OD)_6$ CW-ESR measurements

Samples with well-defined phase transitions at a convenient temperature were necessary for our initial studies. A CW ESR temperature dependence experiment was performed using conventional transverse detection on $KCr_3(SO_4)_2(OD)_6$ powder sample with a Nèel transition temperature of T_N = 50 K. The sample was one of a series of inorganic jarosite-structure compounds obtained from Dr. U.G. Nielsen of the University of Southern Denmark [184].

Following the experiment a reconstruction of the signal amplitude was performed by calculating the modulus using the equation,

$$modulus = \sqrt{Re^2 + Im^2} \tag{7.1}$$

The first derivative was then numerically calculated and the results were plotted (Figure 7-1).

The measurements reveal one sharp signal at temperatures of $T \leq 100$ K with a peak to peak linewidth of 0.9 mT $\leq lwpp \leq$ 6.8 mT and a resonant field of 3.384 T ($g =$

$2.000) \leq B \leq 3.391\ T\ (g = 2.004)$. As the temperature increases towards T_N a broad signal emerges. The signal is initially observed at T = 30 K and becomes dominant at $T \geq T_N$. The linewidth ranges from 7 mT $\leq lwpp \leq$ 34 mT and the resonant field lies between 3.413 T ($g = 1.965$) $\leq B \leq$ 3.447 T ($g = 1.9866$).

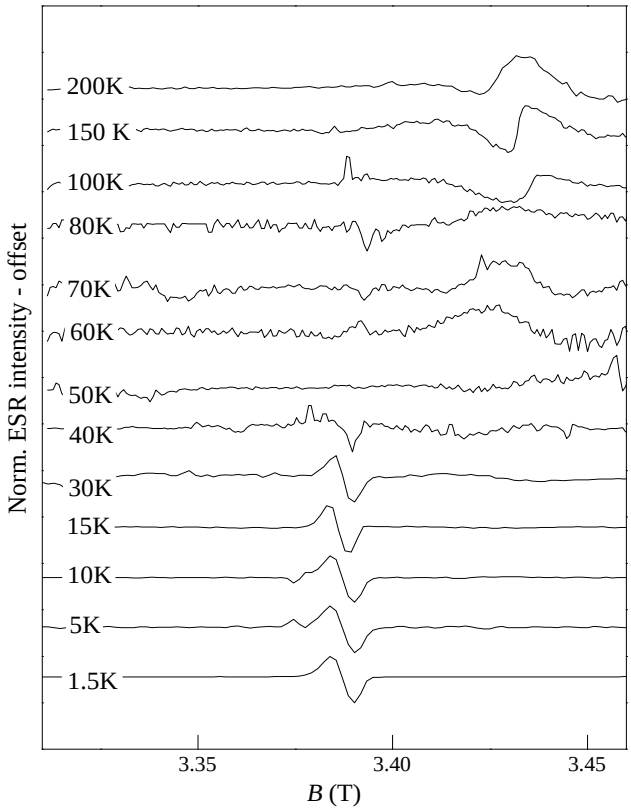

Figure 7-1 Normalized CW ESR temperature dependence for $KCr_3(SO_4)_2(OD)_6$ powder sample.

Below T_N the sharp signal dominates and it can be assumed that it is associated with antiferromagnetism from a domain with a very well defined spherical shape. Similarly, we assume the dominant broad signal above T_N to be associated with a paramagnetic signal of strongly exchange coupled spins. For the purposes of this study, the region of interest is where both signals are observed simultaneously, e.g. T = 40 K, representing a transition region from one to the other magnetic state. In this situation it should be possible to use field jumps to perform a 'pump-probe' experiment in which one resonance is excited and the effects of the excitation, if any,

are monitored on the other resonance providing possible insight into how the different magnetic phases interact. This operation would need to be done before any induced signal has a chance to relax back to equilibrium, as such, for fast relaxing samples it is necessary to employ a technique with no deadtime requirement such as LOD ESR. This requires the design and construction of bespoke hardware compatible with the W-band spectrometer at the University of Nottingham [101].

7.4 Hardware development

This work builds on previous longitudinal detection studies at the University of Nottingham [185]; in particular, a probe designed by Dr Peter Roberts for combined ESR and NMR detection [186].

We designed and built a probe consisting of three main elements: a gradiometer tuning mechanism, a gradiometer detection coil and a self-shielding field jump coil. The detection coil is positioned inside the field jump coil. It consists of two small coils (sample coil and compensation coil) wound in opposite directions and connected in series (Figure 7-3). Thus, if the two coils are otherwise identical as well as being placed in identical environments, the field jump coil should induce exactly equal but opposite signals in the two coils. This would result in a perfect cancellation of the signal induced by the field jumps, ensuring only the signal obtained from the sample, which is located in the sample coil, is observed. In reality producing two identical coils and creating identical fields in two different locations is not possible. It is therefore necessary to determine a means of tuning the gradiometer by balancing the two coils.

7.4.1 Gradiometer tuning mechanism

It was found that by making the compensation coil slightly more sensitive, i.e. with more turns, the coils could then be mechanically tuned by moving the compensation

coil towards the end of the field jump coil where the field begins to diminish. Figure 7-2 shows a photograph of the finished probe with a diagram illustrating the tuning mechanism. A dynamic o-ring shaft seal *FMH-25A*, fixed to an epoxy glass laminate lid, is used to produce rotary motion whilst maintaining the vacuum. This rotary motion is then used to produce linear motion of a stainless steel rod inside the aluminium casing and stainless steel shaft. This is attached to the compensation coil, which is able to move independently of the sample coil, and consequently can be used to tune the gradiometer.

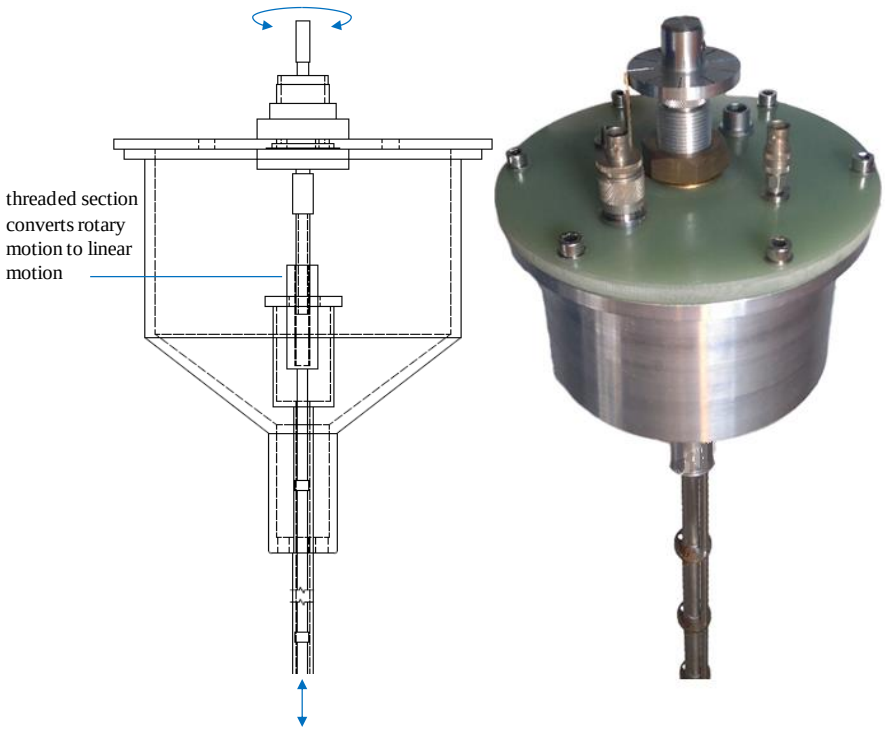

Figure 7-2 Diagram illustrating the probe structure and gradiometer tuning mechanism and a photograph of the finished probe.

7.4.2 Gradiometer detection coil

The detection coil was mounted on a polyether ether ketone (PEEK) probe head (photograph: Figure 7-3). It is possible to machine this thermoplastic down to a

thickness of ~1/4 mm and it has been shown not to contract significantly at low temperatures [187]. This, along with price considerations, makes it an ideal material for use in the probe head. The coil is connected to a SMA jack-jack bulkhead adaptor (Radial, *R125753001*), which was mounted on the lid (photograph: Figure 7-2), via the inner and outer conductor of a copper-copper semi-rigid cable (Micro-coax, *UT-085C*).

The diagram in Figure 7-3 shows the basic principle of the detection coil with the sample cup positioned in the centre of the sample coil. The sample cup is also made of PEEK with a copper plug that serves as a mw mirror. The spring above the probe-head ensures good contact with the probe-base (the probe-base is a 'sleeve' which houses the waveguide and into which the probe is inserted). This contact ensures the sample remains in position directly above the waveguide. With everything in the correct position the sample coil forms a mw shield [188] around the sample cup with the mirror at the top and the waveguide at the bottom, thus creating a crude resonator (see photograph: Figure 7-3). A *LakeShore* cryogenic temperature sensor (*CX-1050-LR-1.4L*) was mounted on the sample coil as close as possible to the sample (not shown in figures) in order to limit errors in temperature readings due to the steep temperature gradient in the bore. It was connected to a *Fischer* 12-way receptacle (*DBEU 1031 A012-130*) which was mounted on the lid (photograph: Figure 7-2).

Bench-top tests were performed to establish how successfully the gradiometer detection coil can be tuned. In order to generate a signal from the detection coil, it was positioned inside a solenoid which was connected to a *Tektronix AFG 3102* dual channel arbitrary/function generator. The 'detected' signal was amplified with a *Femto HVA-200M-40-F* high input impedance voltage amplifier and observed with a *Tektronix TDS 3052* two channel oscilloscope.

The compensation and sample coils were initially balanced by adjusting the number of turns on the compensation coil until the signal was observed to cancel. It was then fine-tuned by adjusting the position of the compensation coil. An attenuation of G_{dB} = 38 dB was calculated, with n_s = 535 and n_c = 635 turns for the sample and compensation coils respectively, using the equation:

$$G_{dB} = 20\log_{10}(V_1/V_0) \quad (7.2)$$

Where V_1 is the voltage without compensation and V_0 is the voltage with the coils balanced.

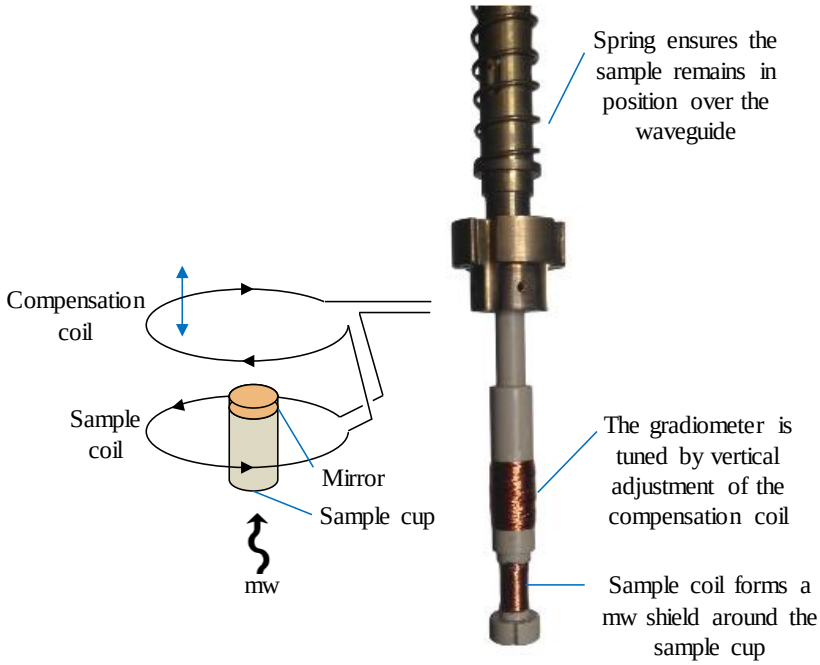

Figure 7-3 Diagram and photograph showing the axial gradiometer detection coil.

7.4.3 Self-shielding field jump coil

The change in magnetic field caused by the field jump induces electric currents (Eddy currents) within any conductors close enough to feel the change. These Eddy currents induce magnetic fields which distort the observed signals. A shielded field jump coil will stop the field-change from reaching the bore (the largest metallic surface within close proximity to the probe-head) thus restricting problems originating from Eddy currents. Further Eddy currents may be generated from the much smaller, but closer, metallic surfaces on the probe-base. However, if this

proves to be a problem, most of these surfaces, with the exception of the waveguide, could be replaced with non-conducting material.

A program implementing a multi-layer approach [189, 190] was adopted to design a coil to shield the field outside the coil while minimizing the effect on the field inside the coil. The approach uses multiple concentric layers of current, capable of acting as primary layers, shield layers or some combination of the two. The program enables us to specify the current distribution such that it produces a zero net field in a region outside the coil when field components produced by every harmonic in every layer are summed.

In order to construct the coil, epoxy resin was spread over a PEEK 'base' and pared down on a lathe. Grooves were etched in the epoxy resin according to the layout for Layer 1 in Figure 7-4, 0.5 mm copper wire was inserted and more epoxy resin was spread and pared down before etching the grooves for Layer 2. This process was repeated until all five layers were in place. The coil was connected to an N jack-jack bulkhead adaptor (Radiall, *R161753000*), which was mounted on the lid (photograph: Figure 7-2), via a beryllium-copper semi-rigid cable (Micro-coax *UT-141B-SS*). It was characterized by taking gaussmeter readings, inside and outside the coil along both the *z* and *r* axis, and the results were compared with the simulations.

The simulation shows the field to be cancelled at r ~ 17 mm i.e. 17 mm from the centre of the coil, which equates to 4 mm from the edge of the coil (Figure 7-5a). This however, is not replicated in the gaussmeter readings. Using Equation 7.2 with V_1 and V_2 replaced with the field measured near the surface of the coil, r = 16 mm, and at the magnet bore, r = 30 mm, respectively, a 22 dB attenuation was calculated between these two points (Figure 7-5b).

The simulation approximates the coil as a series of concentric circles (Figure 7-4) whereas in reality it is a continuous coil and as such it was necessary to have a row of 'notches' along the *z* axis connecting the 'circles'. In order to establish their effect, further measurements were taken both perpendicular and parallel to the notches (Figure 7-6). No significant deviations from the previous readings were observed.

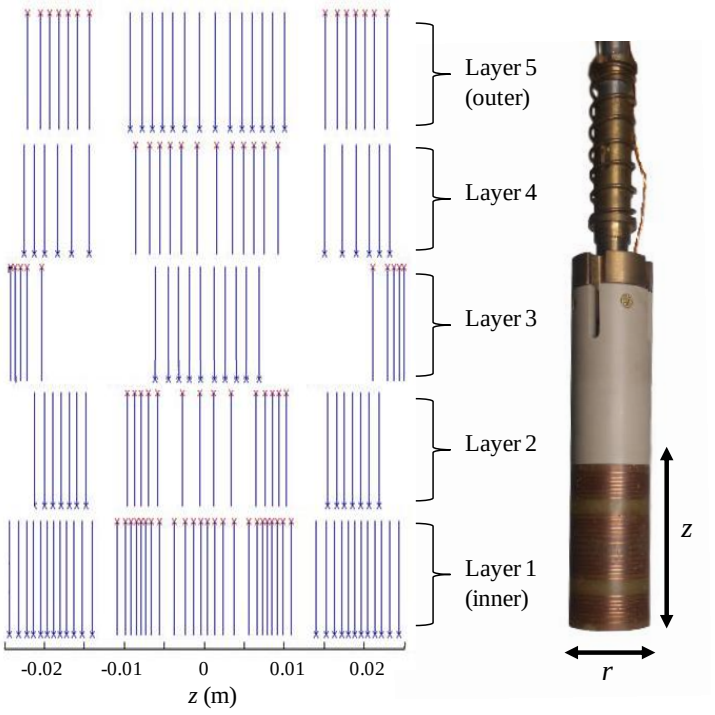

Figure 7-4 Layout of wires in each layer of multi-layer self-shielding coil (crosses denote the direction of the current) and photograph of the finished coil with layer 5 visible.

Measurements were also taken inside the coil to establish the strength and homogeneity of the field experienced by the sample. The simulation shows better than 1 % homogeneity over almost the entire area of one quadrant of the sample cup (Figure 7-7a). The gaussmeter measurements show good homogeneity near the centre of the sample cup but only ~ 10 % homogeneity over the entire sample area (Figure 7-7b). The measurements also show ~ 5 dB attenuation of the signal at the centre of the sample compared with what would be expected from an ideal solenoid according to the equation:

$$B = \mu_0 In/L \tag{7.3}$$

Where I is the current, n is the number of turns and L is the length of the solenoid.

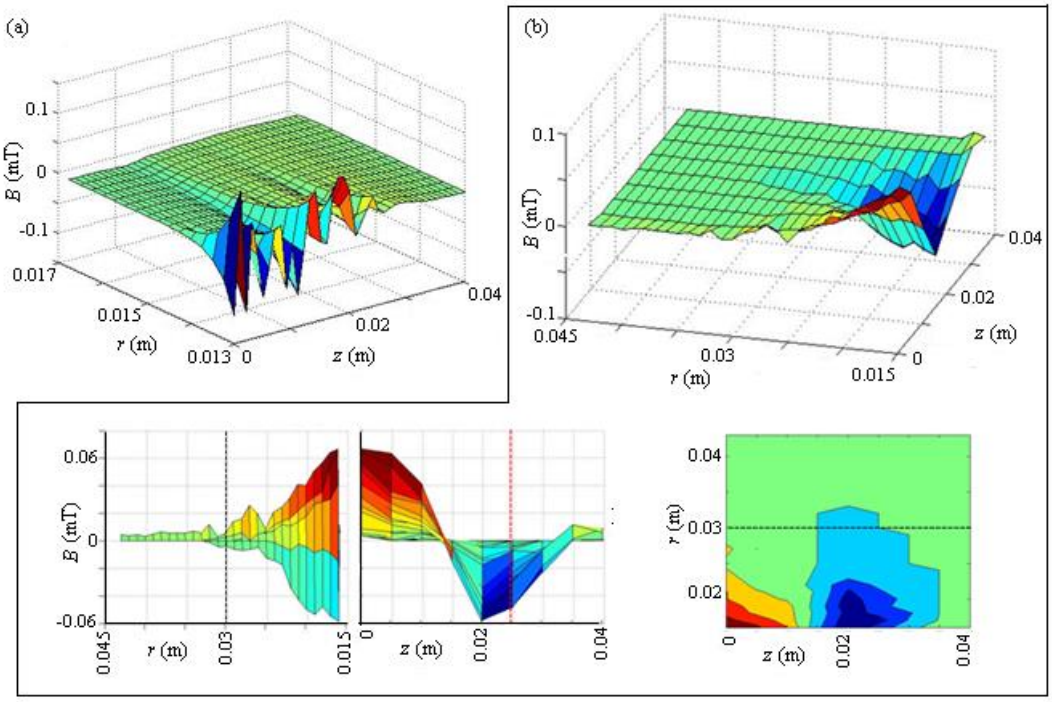

Figure 7-5 (a) Simulated field outside shielded multi-layer coil. (b) Field outside shielded coil (*r*: perpendicular distance from the coil centre, *z*: axial distance from the centre of the coil). The black dashed line represents the magnet bore and the red dashed line represents the edge of the coil.

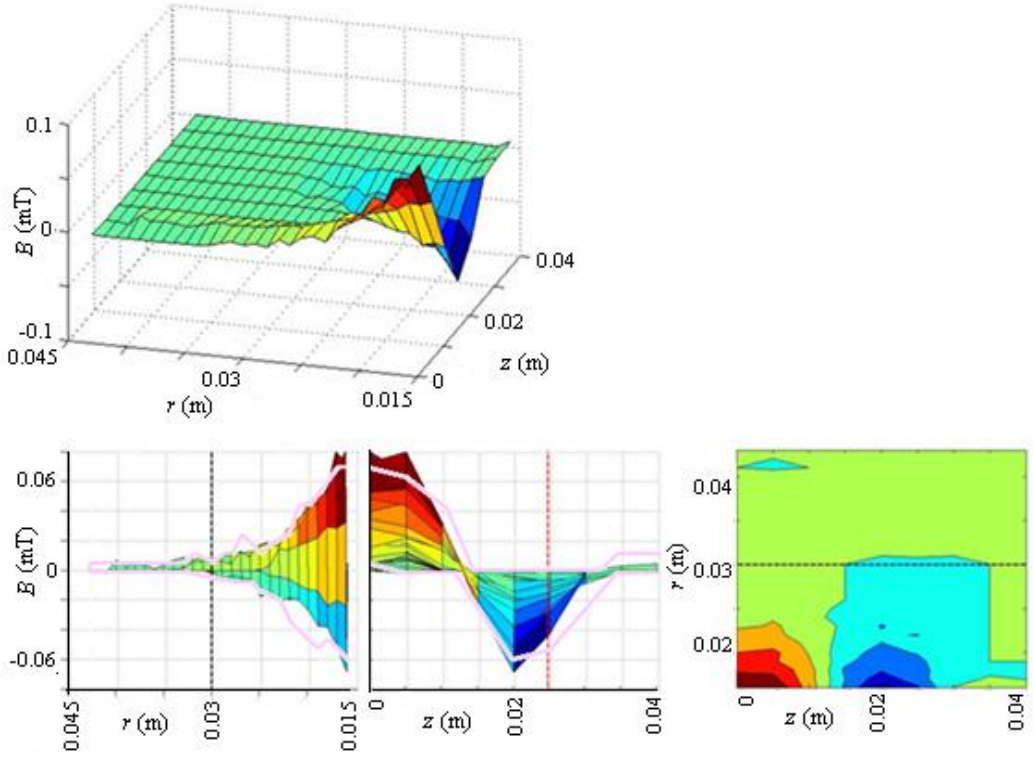

Figure 7-6 Gaussmeter measurements outside shielded coil, along 'notches' (*r*: perpendicular distance from the coil centre, *z*: axial distance from the centre of the coil). The pink lines represent the 'normal' field (as Fig. 7.6b), the black dashed line represents the magnet bore and the red dashed line represents the edge of the coil.

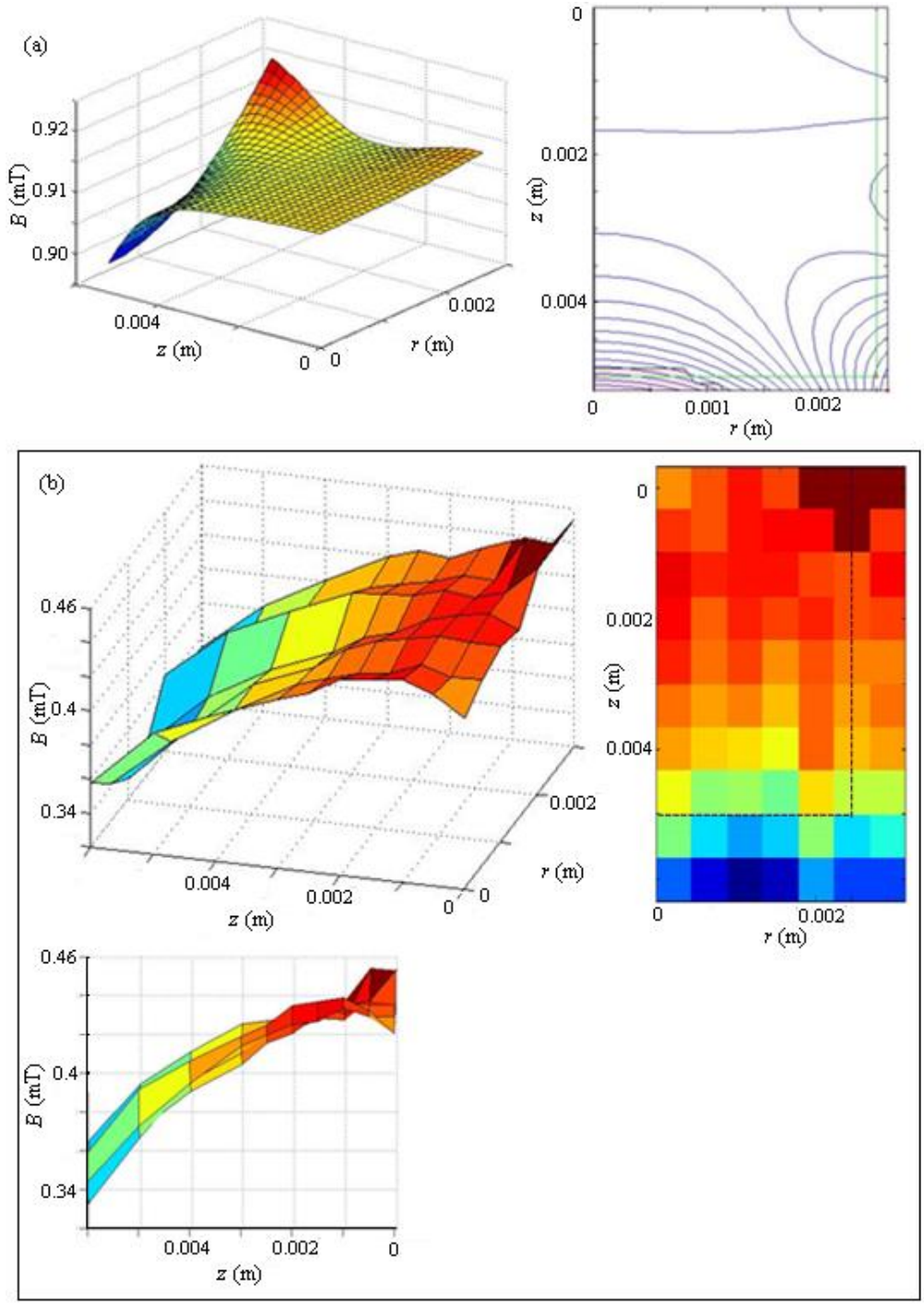

Figure 7-7 (a) simulated field over one quadrant of the sample. (b) Field inside the shielded coil over 1 quadrant of the sample cup (*r*: perpendicular distance from the coil centre, *z*: axial distance from the centre of the coil). The black dashed line represents the edge of the sample cup.

Finally, measurements were made for the field inside the rest of the coil and beyond the coil along the *z* axis (Figure 7-8). The figure shows considerable inhomogeneity as the measurements move away from the centre of the coil, $r = z = 0$. This can be

largely ignored other than to highlight the importance that the sample cup is located as close to the centre of the field jump coil as possible.

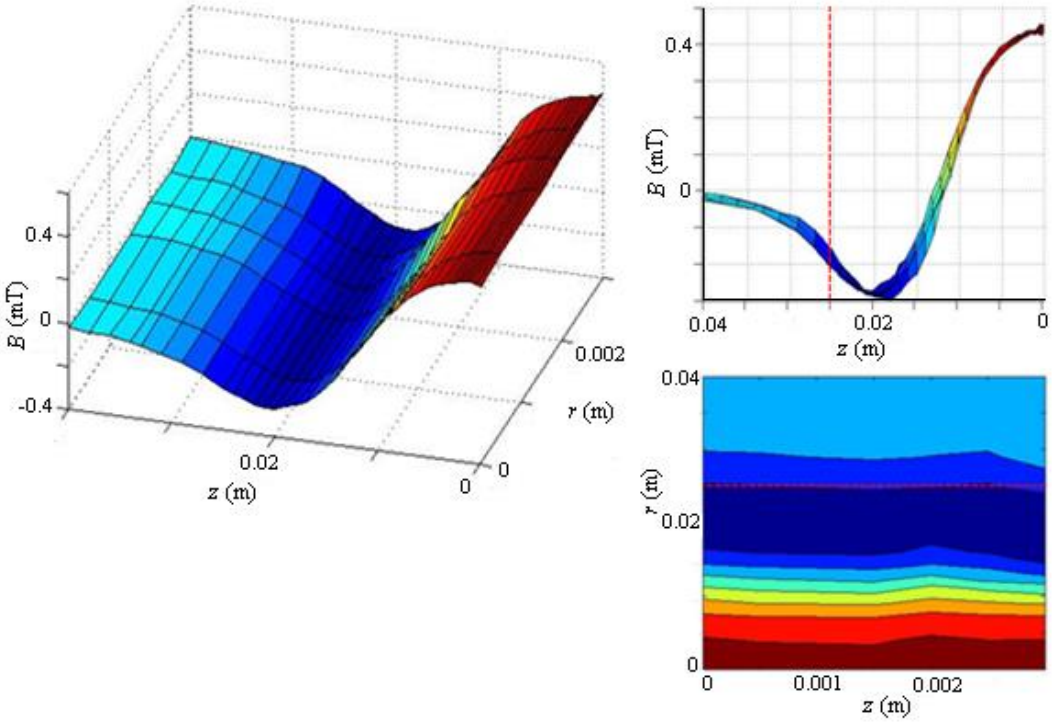

Figure 7-8 Field inside the shielded coil (*r*: perpendicular distance from the coil centre, *z*: axial distance from the centre of the coil). The red dashed line represents the axial distance to the end of the coil.

7.5 Discussion

The results for the gradiometer detection coil are encouraging and would be expected to provide an acceptable cancellation of signals generated by the field jump coil and consequently isolating the signal from the sample. Furthermore, the tuning mechanism has performed well in both bench-top experiments and at cryogenic conditions.

The results for the shelf-shielding field jump coil were less successful. The inhomogeneity of the field over the area of the sample, although disappointing, could

be easily rectified by reducing the length of the sample cup by about half which will affect the amount of sample that can be used and consequently the sensitivity of measurements. However, sample sizes will still be relatively large and this should not cause serious problems providing the accurate positioning of the sample in the centre of the field jump coil, $r = z = 0$.

The poor shielding outside the coil is a more challenging problem. Bench-top oscilloscope readings have shown significant distortion of the signal with the introduction of stainless steel tubing to emulate the magnet bore. This problem is likely to increase in the magnet due to the lower temperature and correspondingly higher conductivity of the stainless steel. Addressing this problem of distortions produced by Eddy currents will require further research to establish why the gaussmeter measurements show such a large deviation from the simulations. Until this has been done it is not possible perform the proposed experiments with the necessary accuracy.

Chapter 8

Conclusions and Outlook

The aim of the work in this thesis was to explore magnetic resonance techniques and develop hardware in order to characterize paramagnetically doped materials, in particular, Mn-doped PbS colloidal QDs.

Initial characterization studies of PbS:Mn QDs demonstrate the successful incorporation of Mn ions into the nanocrystal core with no significant effect on the shape, structure or size distribution. Furthermore, PL and ESR studies show that the optical and magnetic properties can be tailored for specific applications by tuning the Mn content.

We have assessed the potential of PbS:Mn colloidal QDs as electron spin qubits in QIP; in particular, we have studied the limiting factors and ways to enhance the spin coherence times. We have also considered incorporating the nanocrystals in rigid photonic crystal structures for the initialization and readout of the spin qubits.

There was no discernible benefit in engineering the structure of the nanocrystals by overgrowing the core with an undoped shell. It would be of interest to determine whether this was due simply to the shell being too thin and whether a more substantial shell would cause a significant increase in relaxation times, or whether it is the case that the Mn ions are defusing outwards, from the core into the shell.

Dispersing the nanocrystals in a proton free solvent and measuring in frozen solution had significant benefits. We reported unprecedentedly long phase memory and spin–lattice relaxation time constants for Mn^{2+} ions at low temperature, as well as observable coherence near room temperature. These results suggest that further improvements may be possible in nanocrystals with deuterated capping ligands.

The work we have carried out to incorporate nanocrystals into photonic crystal cavities is still in its early stages and more work needs to be done in order to establish the most suitable fabrication technique before we can assess the potential benefits of these devices for QIP applications.

We explored the potential for using magnetically doped QDs as sensitive magnetic nano-probes and the use of electron spins for surface sensing. Magnetic resonance techniques were used to distinguish inequivalent proton spin relaxations of the capping ligands and solvent molecules, strengths and anisotropies of the Mn-nuclear spin interactions, and Mn-nuclear distances. This work demonstrates the complementary use of ^{1}H-NMR and pulsed-ESR for the understanding and control of the QD's surface morphology. This is of great importance for the optimization of their optical and magnetic properties and will ultimately enable the design of multi-functional QDs for a range of practical applications. It is envisaged that further work, to improve the sensitivity of pulsed-ESR or to develop more sophisticated pulsed-ESR methods, will provide more information about the distribution of Mn sites and enable the distinction between inequivalent protons.

The initial development of hardware to study paramagnetically doped materials with mixed magnetic phases was completed. A probe was designed and built with a fast response time and with the aim of facilitating fast field jump experiments to identify interactions between the different magnetic phases by correlating the response of a

sample to mw irradiation with its response to a field jump. Further research is required to address the hardware challenges that have become apparent in the course of this work.

Bibliography

[1] Y. Yin, A. Alivisatos, Colloidal nanocrystal synthesis and the organic-inorganic interface, Nature, 437 (2005) 664-670.

[2] J. Szczech, J. Higgins, S. Jin, Enhancement of the thermoelectric properties in nanoscale and nanostructured materials, Journal of Materials Chemistry, 21 (2011) 4037-4055.

[3] A.L. Efros, A.L. Efros, Interband absorption of light in a semiconductor sphere, Sov. Phys. Semicond., 16 (1982) 772-775.

[4] A.I. Ekimov, F. Hache, M.C. Schanne-Klein, D. Ricard, C. Flytzanis, I.A. Kudryavtsev, T.V. Yazeva, A.V. Rodina, A.L. Efros, Absorption and intensity-dependent photoluminescence measurements on CdSe quantum dots: assignment of the first electronic transitions, J. Opt. Soc. Am. B, 10 (1993) 100-107.

[5] M. El-Sayed, Small is different: Shape-, size-, and composition-dependent properties of some colloidal semiconductor nanocrystals, Accounts of Chemical Research, 37 (2004) 326-333.

[6] V. Lesnyak, N. Gaponik, A. Eychmuller, Colloidal semiconductor nanocrystals: the aqueous approach, Chemical Society Reviews, 42 (2013) 2905-2929.

[7] J. Hollingsworth, V. Klimov, 'Soft' Chemical Synthesis and Manipulation of Semiconductor Nanocrystals, in: V. Klimov (Ed.) Nanocrystal Quantum Dots, CRC Press2010, pp. 1-57.

[8] F.F.P. X. Michalet, L. A. Bentolia, J. M. Tsay, S. Doose, J. J. Li, G. Sundaresan, A. M. Qu, S. S. Gambhir, and S. Weiss, Quantum dots for live cells, in vivo imaging, and diagnostics, 307 (2005).

[9] C. Smith, D. Binks, Multiple Exciton Generation in Colloidal Nanocrystals, Nanomaterials, 4 (2014) 19-45.

[10] W. Chan, S. Nie, Quantum dot bioconjugates for ultrasensitive nonisotopic detection, Science, 281 (1998) 2016-2018.

[11] M. Bruchez, M. Moronne, P. Gin, S. Weiss, A. Alivisatos, Semiconductor nanocrystals as fluorescent biological labels, Science, 281 (1998) 2013-2016.

[12] Y. Gu, R. Cui, Z. Zhang, Z. Xie, D. Pang, Ultrasmall Near-Infrared Ag_2Se Quantum Dots with Tunable Fluorescence for in Vivo Imaging, Journal of the American Chemical Society, 134 (2012) 79-82.

[13] G. Hong, J. Robinson, Y. Zhang, S. Diao, A. Antaris, Q. Wang, H. Dai, In Vivo Fluorescence Imaging with Ag_2S Quantum Dots in the Second Near-Infrared Region, Angewandte Chemie-International Edition, 51 (2012) 9818-9821.

[14] K. Yong, H. Ding, I. Roy, W. Law, E. Bergey, A. Maitra, P. Prasad, Imaging Pancreatic Cancer Using Bioconjugated InP Quantum Dots, ACS Nano, 3 (2009) 502-510.

[15] S. Tamang, G. Beaune, I. Texier, P. Reiss, Aqueous Phase Transfer of InP/ZnS Nanocrystals Conserving Fluorescence and High Colloidal Stability, ACS Nano, 5 (2011) 9392-9402.

[16] K. Fujioka, M. Hiruoka, K. Sato, N. Manabe, R. Miyasaka, S. Hanada, A. Hoshino, R. Tilley, Y. Manome, K. Hirakuri, K. Yamamoto, Luminescent passive-oxidized silicon quantum dots as biological staining labels and their cytotoxicity effects at high concentration, Nanotechnology, 19 (2008).

[17] H. Li, Z. Kang, Y. Liu, S. Lee, Carbon nanodots: synthesis, properties and applications, Journal of Materials Chemistry, 22 (2012) 24230-24253.

[18] L. Turyanska, F. Moro, A. Knott, M. Fay, T. Bradshaw, A. Patane, Paramagnetic, Near-Infrared Fluorescent Mn-Doped PbS Colloidal Nanocrystals, Particle & Particle Systems Characterization, 30 (2013) 945-949.

[19] E. Cassette, M. Helle, L. Bezdetnaya, F. Marchal, B. Dubertret, T. Pons, Design of new quantum dot materials for deep tissue infrared imaging, Advanced Drug Delivery Reviews, 65 (2013) 719-731.

[20] L. Jing, K. Ding, S. Kershaw, I. Kempson, A. Rogach, M. Gao, Magnetically Engineered Semiconductor Quantum Dots as Multimodal Imaging Probes, Advanced Materials, 26 (2014) 6367-6386.

[21] B. Oregan, M. Gratzel, A low-cost, high efficiency solar-cell based on dye-sensitized colloidal TiO_2 films, Nature, 353 (1991) 737-740.

[22] M. Gratzel, Recent Advances in Sensitized Mesoscopic Solar Cells, Accounts of Chemical Research, 42 (2009) 1788-1798.

[23] A. Zaban, O. Micic, B. Gregg, A. Nozik, Photosensitization of nanoporous TiO2 electrodes with InP quantum dots, Langmuir, 14 (1998) 3153-3156.

[24] R. Plass, S. Pelet, J. Krueger, M. Gratzel, U. Bach, Quantum dot sensitization of organic-inorganic hybrid solar cells, Journal of Physical Chemistry B, 106 (2002) 7578-7580.

[25] V. Klimov, A. Mikhailovsky, S. Xu, A. Malko, J. Hollingsworth, C. Leatherdale, H. Eisler, M. Bawendi, Optical gain and stimulated emission in nanocrystal quantum dots, Science, 290 (2000) 314-317.

[26] C. She, I. Fedin, D. Dolzhnikov, A. Demortiere, R. Schaller, M. Pelton, D. Talapin, Low-Threshold Stimulated Emission Using Colloidal Quantum Wells, Nano Letters, 14 (2014) 2772-2777.

[27] V. Colvin, M. Schlamp, A. Alivisatos, Light-Emitting-Diodes made from Cadmium Selenide Nanocrystals And A Semiconducting Polymer, Nature, 370 (1994) 354-357.

[28] B. Dabbousi, M. Bawendi, O. Onitsuka, M. Rubner, Electroluminescence from CdSe Quantum-Dot Polymer Composites, Applied Physics Letters, 66 (1995) 1316-1318.

[29] S. Coe, W. Woo, M. Bawendi, V. Bulovic, Electroluminescence from single monolayers of nanocrystals in molecular organic devices, Nature, 420 (2002) 800-803.

[30] B.I. Shklovskii, A.L. Efros, Electronic Properties of Doped Semiconductors, Springer2013.

[31] J. Bryan, D. Gamelin, K. Karlin, Doped Semiconductor Nanocrystals: Synthesis, Characterization, Physical Properties, and Applications, Progress in Inorganic Chemistry, Vol 54, 54 (2005) 47-126.

[32] J. Huang, X. Zhong, L. Wang, L. Yang, H. Mao, Improving the Magnetic Resonance Imaging Contrast and Detection Methods with Engineered Magnetic Nanoparticles, Theranostics, 2 (2012) 86-102.

[33] R. Koole, W. Mulder, M. van Schooneveld, G. Strijkers, A. Meijerink, K. Nicolay, Magnetic quantum dots for multimodal imaging, Wiley Interdisciplinary Reviews-Nanomedicine and Nanobiotechnology, 1 (2009) 475-491.

[34] K. Ando, Magneto-optics of diluted magnetic semiconductors: New materials and applications, Springer, Germany, 2000.

[35] G. Salis, Y. Kato, K. Ensslin, D. Driscoll, A. Gossard, D. Awschalom, Electrical control of spin coherence in semiconductor nanostructures, Nature, 414 (2001) 619-622.

[36] M. Doty, M. Scheibner, I. Ponomarev, E. Stinaff, A. Bracker, V. Korenev, T. Reinecke, D. Gammon, Electrically tunable g factors in quantum dot molecular spin states, Physical Review Letters, 97 (2006).

[37] T. Nakaoka, T. Saito, J. Tatebayashi, S. Hirose, T. Usuki, N. Yokoyama, Y. Arakawa, Tuning of g-factor in self-assembled In(Ga)As quantum dots through strain engineering, Physical Review B, 71 (2005).

[38] D. Bussian, S. Crooker, M. Yin, M. Brynda, A. Efros, V. Klimov, Tunable magnetic exchange interactions in manganese-doped inverted core-shell ZnSe-CdSe nanocrystals, Nature Materials, 8 (2009) 35-40.

[39] M. Atature, J. Dreiser, A. Badolato, A. Hogele, K. Karrai, A. Imamoglu, Quantum-dot spin-state preparation with near-unity fidelity, Science, 312 (2006) 551-553.

[40] D. Kim, W. Sheng, P. Poole, D. Dalacu, J. Lefebvre, J. Lapointe, M. Reimer, G. Aers, R. Williams, Tuning the exciton g factor in single InAs/InP quantum dots, Physical Review B, 79 (2009).

[41] J. Furdyna, Diluted Magnetic Semiconductors, Journal of Applied Physics, 64 (1988) R29-R64.

[42] G. Bacher, A. Maksimov, H. Schomig, V. Kulakovskii, M. Welsch, A. Forchel, P. Dorozhkin, A. Chernenko, S. Lee, M. Dobrowolska, J. Furdyna, Monitoring statistical magnetic fluctuations on the nanometer scale, Physical Review Letters, 89 (2002).

[43] B. Peng, W. Liang, M. White, D. Gamelin, X. Li, Theoretical Evaluation of Spin-Dependent Auger De-Excitation in Mn^{2+}-Doped Semiconductor Nanocrystals, Journal of Physical Chemistry C, 116 (2012) 11223-11231.

[44] R. Beaulac, Y. Feng, J. May, E. Badaeva, D. Gamelin, X. Li, Orbital pathways for Mn^{2+}-carrier *sp-d* exchange in diluted magnetic semiconductor quantum dots, Physical Review B, 84 (2011).

[45] R. Beaulac, P. Archer, J. van Rijssel, A. Meijerink, D. Gamelin, Exciton storage by Mn^{2+} in colloidal Mn^{2+}-doped CdSe quantum dots, Nano Letters, 8 (2008) 2949-2953.

[46] R. Beaulac, P. Archer, D. Gamelin, Luminescence in colloidal Mn^{2+}-doped semiconductor nanocrystals, Journal of Solid State Chemistry, 181 (2008) 1582-1589.

[47] R. Beaulac, P. Archer, X. Liu, S. Lee, G. Salley, M. Dobrowolska, J. Furdyna, D. Gamelin, Spin-polarizable excitonic luminescence in colloidal Mn^{2+}-doped CdSe quantum dots, Nano Letters, 8 (2008) 1197-1201.

[48] L. Bradshaw, A. Hauser, E. McLaurin, D. Gamelin, Luminescence Saturation via Mn^{2+}-Exciton Cross Relaxation in Colloidal Doped Semiconductor Nanocrystals, Journal of Physical Chemistry C, 116 (2012) 9300-9310.

[49] Y. Feng, E. Badaeva, D. Gamelin, X. Li, Excited-State Double Exchange in Manganese-Doped ZnO Quantum Dots: A Time-Dependent Density-Functional Study, Journal of Physical Chemistry Letters, 1 (2010) 1927-1931.

[50] S. Ochsenbein, D. Gamelin, Quantum oscillations in magnetically doped colloidal nanocrystals, Nature Nanotechnology, 6 (2011) 111-114.

[51] E. Badaeva, J. May, J. Ma, D. Gamelin, X. Li, Characterization of Excited-State Magnetic Exchange in Mn^{2+}-Doped ZnO Quantum Dots Using Time-Dependent Density Functional Theory, Journal of Physical Chemistry C, 115 (2011) 20986-20991.

[52] N. Norberg, K. Kittilstved, J. Amonette, R. Kukkadapu, D. Schwartz, D. Gamelin, Synthesis of colloidal Mn^{2+}: ZnO quantum dots and high-Tc ferromagnetic nanocrystalline thin films, Journal of the American Chemical Society, 126 (2004) 9387-9398.

[53] C. Johnson, K. Kittilstved, T. Kaspar, T. Droubay, S. Chambers, G. Salley, D. Gamelin, Mid-gap electronic states in $Zn_{1-x}Mn_xO$, Physical Review B, 82 (2010).

[54] A. Louie, Multimodality Imaging Probes: Design and Challenges, Chemical Reviews, 110 (2010) 3146-3195.

[55] N. Murase, R. Jagannathan, Y. Kanematsu, M. Watanabe, A. Kurita, K. Hirata, T. Yazawa, T. Kushida, Fluorescence and EPR characteristics of Mn^{2+}-doped ZnS nanocrystals prepared by aqueous colloidal method, Journal of Physical Chemistry B, 103 (1999) 754-760.

[56] A. Pattantyus-Abraham, I. Kramer, A. Barkhouse, X. Wang, G. Konstantatos, R. Debnath, L. Levina, I. Raabe, M. Nazeeruddin, M. Gratzel, E. Sargent, Depleted-Heterojunction Colloidal Quantum Dot Solar Cells, ACS Nano, 4 (2010) 3374-3380.

[57] N. Zhao, T. Osedach, L. Chang, S. Geyer, D. Wanger, M. Binda, A. Arango, M. Bawendi, V. Bulovic, Colloidal PbS Quantum Dot Solar Cells with High Fill Factor, ACS Nano, 4 (2010) 3743-3752.

[58] J. Choi, Y. Lim, M. Santiago-Berrios, M. Oh, B. Hyun, L. Sung, A. Bartnik, A. Goedhart, G. Malliaras, H. Abruna, F. Wise, T. Hanrath, PbSe Nanocrystal Excitonic Solar Cells, Nano Letters, 9 (2009) 3749-3755.

[59] O. Madelung, Semiconductor: Data Handbook, 3 ed., Springer 2004.

[60] S. Erwin, L. Zu, M. Haftel, A. Efros, T. Kennedy, D. Norris, Doping semiconductor nanocrystals, Nature, 436 (2005) 91-94.

[61] N. Pradhan, D. Sarma, Advances in Light-Emitting Doped Semiconductor Nanocrystals, Journal of Physical Chemistry Letters, 2 (2011) 2818-2826.

[62] D. Isheim, J. Kaszpurenko, D. Yu, Z. Mao, D. Seidman, I. Arslan, 3-D Atomic-Scale Mapping of Manganese Dopants in Lead Sulfide Nanowires, Journal of Physical Chemistry C, 116 (2012) 6595-6600.

[63] S. Prado, L. Villegas-Lelovsky, A. Alcalde, V. Lopez-Richard, G. Marques, Magneto-optical properties in IV-VI lead-salt semimagnetic nanocrystals, Nanoscale Research Letters, 7 (2012).

[64] T. Ji, W. Jian, J. Fang, The first synthesis of $Pb_{1-x}Mn_xSe$ nanocrystals, Journal of the American Chemical Society, 125 (2003) 8448-8449.

[65] R. Silva, O. Baffa, F. Chen, S. Lourenco, N. Dantas, Luminescence in semimagnetic $Pb_{1-x}Mn_xSe$ quantum dots grown in a glass host: Radiative and nonradiative emission processes, Chemical Physics Letters, 567 (2013) 23-26.

[66] R. Silva, P. Morais, F. Qu, A. Alcalde, N. Dantas, H. Sullasi, Synthesis process controlled magnetic properties of $Pb_{1-x}Mn_xS$ nanocrystals, Applied Physics Letters, 90 (2007).

[67] G. Long, B. Barman, S. Delikanli, Y. Tsai, P. Zhang, A. Petrou, H. Zeng, Carrier-dopant exchange interactions in Mn-doped PbS colloidal quantum dots, Applied Physics Letters, 101 (2012).

[68] C.H. Bennett, G. Brassard, Quantum cryptography: Public key distribution and coin tossing, IEEE International Conference on Computers, Systems and Signal Processing, 1984, pp. 175-179.

[69] D. DiVinchenzo, The Physical Implementation of Quantum Computation, Fortschr. Phys., 48 (2000) 771-783.

[70] C. Le Gall, R.S. Kolodka, C.L. Cao, H. Boukari, H. Mariette, J. Fernández-Rossier, L. Besombes, Optical initialization, readout, and dynamics of a Mn spin in a quantum dot, Phys Rev B, 81 (2010).

[71] L.L. Besombes, Y. Bernos, J. Boukari, H. Mariette, H. Poizat, J. P. Clement, T. Fernández-Rossier, J. Aguado, R., Optical probing of spin fluctuations of a single paramagnetic Mn atom in a semiconductor quantum dot, Phys. Rev. B, 78 (2008).

[72] A.M. Tyryshkin, J.J.L. Morton, S.C. Benjamin, A. Ardavan, G.A.D. Briggs, J.W. Ager, S.A. Lyon, Coherence of spin qubits in silicon, J. Phys. Condens. Matter 18 (2006) S783-S794.

[73] A.M. Tyryshkin, S. Tojo, J.J.L. Morton, H. Riemann, N.V. Abrosimov, P. Becker, H. Pohl, T. Schenkel, M.L.W. Thewalt, K.M. Itoh, S.A. Lyon, Electron spin coherence exceeding seconds in high-purity silicon, Nature Materials, 11 (2012) 143-147.

[74] M. Steger, K. Saeedi, M.L.W. Thewalt, J.J.L. Morton, H. Riemann, N.V. Abrosimov, P. Becker, H.-J. Pohl, Quantum Information Storage for over 180 s Using Donor Spins in a ^{28}Si "Semiconductor Vacuum", Science, 336 (2012) 1280-1283.

[75] G.W. Morley, P. Lueders, M.H. Mohammady, S.J. Balian, G. Aeppli, C.W. M. Kay, W.M. Witzel, J. G., T.S. Monteiro, Quantum control of hybrid nuclear–electronic qubits, Nature Materials, 12 (2013) 103-107.

[76] K. Bader, D. Dengler, S. Lenz, B. Endeward, S. Jiang, P. Neugebauer, J. van Slageren, Room temperature quantum coherence in a potential molecular qubit, Nature Communications, 5 (2014).

[77] T. Kennedy, J. Colton, J. Butler, R. Linares, P. Doering, Long coherence times at 300 K for nitrogen-vacancy center spins in diamond grown by chemical vapor deposition, Applied Physics Letters, 83 (2003) 4190-4192.

[78] S. Takahashi, R. Hanson, J. van Tol, M. Sherwin, D. Awschalom, Quenching spin decoherence in diamond through spin bath polarization, Physical Review Letters, 101 (2008).

[79] A. Schimpf, S. Ochsenbein, D. Gamelin, Surface Contributions to Mn^{2+} Spin Dynamics in Colloidal Doped Quantum Dots, Journal of Physical Chemistry Letters, 6 (2015) 457-463.

[80] L. Besombes, Y. Leger, L. Maingault, D. Ferrand, H. Mariette, J. Cibert, Probing the spin state of a single magnetic ion in an individual quantum dot, Physical Review Letters, 93 (2004).

[81] G. Scholes, G. Rumbles, Excitons in nanoscale systems, Nature Materials, 5 (2006) 683.

[82] R. Beaulac, P. Archer, S. Ochsenbein, D. Gamelin, Mn^{2+}-Doped CdSe Quantum Dots: New Inorganic Materials for Spin-Electronics and Spin-Photonics, Advanced Functional Materials, 18 (2008) 3873-3891.

[83] C.R.J. Sheppard, Approximate calculation of the reflection coefficient from a stratified medium, Pure Appl. Opt., 4 (1995) 665-669.

[84] J.W. Strutt, On the Maintenance of Vibrations by Forces of Double Frequency, and on the Propagation of Waves Through a Medium Endowed with a Periodic Structure, Phil. Mag., 24 (1887) 145-159.

[85] S. Lukishova, L. Bissell, V. Menon, N. Valappil, M. Hahn, C. Evans, B. Zimmerman, T. Krauss, C. Stroud, R. Boyd, Organic photonic bandgap microcavities doped with semiconductor nanocrystals for room-temperature on-demand single-photon sources, Journal of Modern Optics, 56 (2009) 167-174.

[86] D. Goldberg, V. Menon, Enhanced amplified spontaneous emission from colloidal quantum dots in all-dielectric monolithic microcavities, Applied Physics Letters, 102 (2013).

[87] L. Martiradonna, L. Carbone, M. De Giorgi, L. Manna, G. Gigli, R. Cingolani, M. De Vittorio, High Q-factor colloidal nanocrystal-based vertical microcavity by hot embossing technology, Applied Physics Letters, 88 (2006).

[88] M. Kahl, T. Thomay, V. Kohnle, K. Beha, J. Merlein, M. Hagner, A. Halm, J. Ziegler, T. Nann, Y. Fedutik, U. Woggon, M. Artemyev, F. Perez-Willard, A. Leitenstorfer, R. Bratschitsch, Colloidal quantum dots in all-dielectric high-Q pillar microcavities, Nano Letters, 7 (2007) 2897-2900.

[89] P. Lodahl, A. van Driel, I. Nikolaev, A. Irman, K. Overgaag, D. Vanmaekelbergh, W. Vos, Controlling the dynamics of spontaneous emission from quantum dots by photonic crystals, Nature, 430 (2004) 654-657.

[90] J. Wijnhoven, W. Vos, Preparation of photonic crystals made of air spheres in titania, Science, 281 (1998) 802-804.

[91] Z. Wu, Z. Mi, P. Bhattacharya, T. Zhu, J. Xu, Enhanced spontaneous emission at 1.55 mu m from colloidal PbSe quantum dots in a Si photonic crystal microcavity, Applied Physics Letters, 90 (2007).

[92] R. Bose, X. Yang, R. Chatterjee, J. Gao, C. Wong, Weak coupling interactions of colloidal lead sulphide nanocrystals with silicon photonic crystal nanocavities near 1.55 mu m at room temperature, Applied Physics Letters, 90 (2007).

[93] I. Fushman, D. Englund, J. Vuckovic, Coupling of PbS quantum dots to photonic crystal cavities at room temperature, Applied Physics Letters, 87 (2005).

[94] L. Levina, W. Sukhovatkin, S. Musikhin, S. Cauchi, R. Nisman, D.P. Bazett-Jones, S.E. H., Efficient infrared-emitting PbS quantum dots grown on DNA and stable in aqueous solution and blood plasma, Advanced Materials, 17 (2005).

[95] D.J. Smith, The realization of atomic resolution with the electron microscope, Rep. Prog. Phys., 60 (1997) 1513-1580.

[96] X. Michalet, F. Pinaud, L. Bentolila, J. Tsay, S. Doose, J. Li, G. Sundaresan, A. Wu, S. Gambhir, S. Weiss, Quantum dots for live cells, in vivo imaging, and diagnostics, Science, 307 (2005) 538-544.

[97] K. Tsuji, J. Injuk, G.R. V, X-Ray Spectroscopy: Recent Technological Advances, Wiley2004.

[98] J.B. Pethica, W.C. Oliver, Tip Surface Interaction in STM and AFM, Physica Scripta. T, 19 (1987) 61-66.

[99] N.M. Atherton, Principles of Electron Spin Resonance, Ellis Horwood Limited1993.

[100] A. Schweiger, G. Jeschke, Principles of Pulse Electron Paramagnetic Resonance, Oxford University Press2001.

[101] I. Gromov, V. Krymov, P. Manikandan, D. Arieli, D. Goldfarb, A W-band pulsed ENDOR spectrometer: Setup and applicationto transition metal centers, J. Magn. Reson., 139 (1999) 8-17.

[102] S. Stoll, A. Schweiger, EasySpin, a comprehensive software package for spectral simulation and analysis in EPR, *J. Magn. Reson.*, 178 (2006) 42-55.

[103] S. Bertaina, S. Gambarelli, A. Tkachuk, I.N. Kurkin, B. Malkin, A. Stepanov, B. Barbara, Rare-earth solid-state qubits, Nat. Nanotechnol., 2 (2007) 39-42.

[104] E.R. Davies, A New Pulse ENDOR Technique, Physics Letters, 47A (1974) 1-2.

[105] W.B. Mims, Pulsed ENDOR experiments, Proc. R. Soc. London, 283 (1965) 452-457.

[106] J. Granwehr, J. Forrer, A. Schweiger, Longitudinally Detected EPR: Improved Instrumentation and New Pulse Schemes Journal of Magnetic Resonance, 151 (2001) 78-84.

[107] J. Granwehr, A New Approach to Longitudinally detected Electron Paramagnetic Resonance, Swiss Federal Institute of Technology Zurich Zurich, 2002.

[108] M. Fox, Optical Properties of Solids, Oxford University Press2004.

[109] J. Serbin, A. Ovsianikov, B. Chichkov, Fabrication of woodpile structures by two-photon polymerization and investigation of their optical properties, Optics Express, 12 (2004) 5221-5228.
[110] Nanoscribe, Datasheet IP Photoresist.
[111] Nanoscribe, Data sheet Photonic Professional *GT*, 2015.
[112] L. Turyanska, R. Hill, O. Makarovsky, F. Moro, A. Knott, O. Larkin, A. Patane, A. Meaney, P. Christianen, M. Fay, R. Curry, Tuneable paramagnetic susceptibility and exciton g-factor in Mn-doped PbS colloidal nanocrystals, Nanoscale, 6 (2014) 8919-8925.
[113] S. Mochizuki, N. Takayama, Spin-Wave-Assisted Photoluminescence in MnS at Low-Temperatures, Journal of Physics-Condensed Matter, 3 (1991) 2729-2734.
[114] Y. Wang, A. Suna, W. Mahler, R. Kasowski, PBS in Polymers - From Molecules to Bulk Solids, Journal of Chemical Physics, 87 (1987) 7315-7322.
[115] F. Moro, L. Turyanska, J. Granwehr, A. Patane, Spin manipulation and spin-lattice interaction in magnetic colloidal quantum dots, Physical Review B, 90 (2014).
[116] M. Hines, P. Guyot-Sionnest, Synthesis and characterization of strongly luminescing ZnS-Capped CdSe nanocrystals, Journal of Physical Chemistry, 100 (1996) 468-471.
[117] A. Pandey, P. Guyot-Sionnest, Slow Electron Cooling in Colloidal Quantum Dots, Science, 322 (2008) 929-932.
[118] B. Mahler, P. Spinicelli, S. Buil, X. Quelin, J. Hermier, B. Dubertret, Towards non-blinking colloidal quantum dots, Nature Materials, 7 (2008) 659-664.
[119] D. Oron, M. Kazes, U. Banin, Multiexcitons in type-II colloidal semiconductor quantum dots, Physical Review B, 75 (2007).
[120] L. Turyanska, U. Elfurawi, M. Li, M. Fay, N. Thomas, S. Mann, J. Blokland, P. Christianen, A. Patane, Tailoring the physical properties of thiol-capped PbS quantum dots by thermal annealing, Nanotechnology, 20 (2009).
[121] X.L. Tan, M. Bernardo, H. Thomann, C.P. Scholes, ^{17} O hyperfine and quadrupole interactions for water ligands in frozen solutions of high spin Mn^{2+}, Journal of Chemical Physics, 102 (1995) 2675-2690.
[122] R. Buonsanti, D. Milliron, Chemistry of Doped Colloidal Nanocrystals, Chemistry of Materials, 25 (2013) 1305-1317.
[123] F. Qu, P. Hawrylak, Theory of electron mediated Mn-Mn interactions in quantum dots, Physical Review Letters, 96 (2006).

[124] A. Abragam, B. Bleaney, Electron Paramagnetic Resonance of Transition Ions, Oxford University Press1970.

[125] A. Schweiger, G. Jeschke, Principles of pulse electron paramagnetic resonance, Oxford University Press2005.

[126] S. Eaton, G. Eaton, Relaxation times of organic radicals and transition metal ions, Kluwer Academic/Plenum Publ2000.

[127] D. Marsh, R. Bartucci, R. Guzzi, L. Sportelli, M. Esmann, Librational fluctuations in protein glasses, Biochimica Et Biophysica Acta-Proteins and Proteomics, 1834 (2013) 1591-1595.

[128] S. Goldman, B. GV, F. JH, ESR studies of anisotropic rotational reorientation and slow tumbling in liquid and frozen media. II. Saturation and nonsecular effects, Journal of Chemical Physics, 59 (1973).

[129] P.G. Baranov, S.B. Orlinskii, C.d.M. Donega, J. Schmidt, High-frequency EPR and ENDOR spectroscopy on semiconductor quantum dots, Appl. Magn. Reson., 39 (2010) 151-183.

[130] M. Scheibner, T. Kennedy, L. Worschech, A. Forchel, G. Bacher, T. Slobodskyy, G. Schmidt, L. Molenkamp, Coherent dynamics of locally interacting spins in self-assembled $Cd_{1-x}Mn_xSe/ZnSe$ quantum dots, Physical Review B, 73 (2006).

[131] C. Wedge, G. Timco, E. Spielberg, R. George, F. Tuna, S. Rigby, E. McInnes, R. Winpenny, S. Blundell, A. Ardavan, Chemical Engineering of Molecular Qubits, Physical Review Letters, 108 (2012).

[132] M. Goryca, M. Koperski, P. Wojnar, T. Smolenski, T. Kazimierczuk, A. Golnik, P. Kossacki, Coherent Precession of an Individual 5/2 Spin, Physical Review Letters, 113 (2014).

[133] R. Warburton, Single spins in self-assembled quantum dots, Nature Materials, 12 (2013) 483-493.

[134] T. Dietl, P. Peyla, W. Grieshaber, Y. Daubigne, Dynamics of Spin Organization in Diluted Magnetic Semiconductors, Physical Review Letters, 74 (1995) 474-477.

[135] S. Cronenberger, P. Barate, A. Brunetti, M. Vladimirova, D. Scalbert, F. Teran, G. Karzewski, T. Wojtowicz, Electron spin relaxation in very diluted CdMnTe quantum wells, Superlattices and Microstructures, 43 (2008) 427-430.

[136] S. Crooker, D. Tulchinsky, J. Levy, D. Awschalom, R. Garcia, N. Samarth, Enhanced Spin Interactions in Digital Magnetic Heterostructures, Physical Review Letters, 75 (1995) 505-508.

[137] P. Baranov, S. Orlinskii, C. Donega, J. Schmidt, High-frequency EPR, ESE, and ENDOR spectroscopy of Co- and Mn-doped ZnO quantum dots, Physica Status Solidi B-Basic Solid State Physics, 250 (2013) 2137-2140.

[138] M. Kneip, D. Yakovlev, M. Bayer, A. Maksimov, I. Tartakovskii, D. Keller, W. Ossau, L. Molenkamp, A. Waag, Spin-lattice relaxation of Mn ions in ZnMnSe/ZnBeSe quantum wells measured under pulsed photoexcitation, Physical Review B, 73 (2006).

[139] V. Ivanov, M. Godlewski, ODMR Study of Zn1-xMnxSe/Zn1-yBeySe and (Cd_{1-x},Mn)Te/Cd_{1-y}MgyTe Diluted Magnetic Semiconductor Quantum Wells, Applied Magnetic Resonance, 39 (2010) 31-47.

[140] G. Eaton, S. Eaton, Solvent and temperature dependence of spin echo dephasing for chromium(V) and vanadyl complexes in glassy solution, Journal of Magnetic Resonance, 136 (1999) 63-68.

[141] A. Zecevic, G. Eaton, S. Eaton, M. Lindgren, Dephasing of electron spin echoes for nitroxyl radicals in glassy solvents by non-methyl and methyl protons, Molecular Physics, 95 (1998) 1255-1263.

[142] R. Colombelli, K. Srinivasan, M. Troccoli, O. Painter, C. Gmachl, D. Tennant, A. Sergent, D. Sivco, A. Cho, F. Capasso, Quantum cascade surface-emitting photonic crystal laser, Science, 302 (2003) 1374-1377.

[143] H. Ryu, Large Enhancement of Extraction Efficiency in Thin-Film Photonic Crystal InGaN Light-Emitting Diode Structures, Journal of the Korean Physical Society, 55 (2009) 2642-2645.

[144] M. Gratzel, Photoelectrochemical cells, Nature, 414 (2001) 338-344.

[145] S. Carter, T. Sweeney, M. Kim, C. Kim, D. Solenov, S. Economou, T. Reinecke, L. Yang, A. Bracker, D. Gammon, Quantum control of a spin qubit coupled to a photonic crystal cavity, Nature Photonics, 7 (2013) 329-334.

[146] F. Moro, L. Turyanska, J. Wilman, A. Fielding, M. Fay, J. Granwehr, A. Patane, Electron spin coherence near room temperature in magnetic quantum dots, Scientific Reports, 5 (2015).

[147] J.D. Joannopoulos, S.G. Johnson, J.N. Winn, R.D. Meade, Photonic Crystals: Molding the Flow of Light, pp. 246-247, 2 ed., Princeton University Press2008.

[148] K. Vahala, Optical microcavities, Nature, 424 (2003) 839-846.
[149] N. Ray, N. Staley, D. Grinolds, M. Bawendi, M. Kastner, Measuring Ligand-Dependent Transport in Nanopatterned PbS Colloidal Quantum Dot Arrays Using Charge Sensing, Nano Letters, 15 (2015) 4401-4405.
[150] D. Mocatta, G. Cohen, J. Schattner, O. Millo, E. Rabani, U. Banin, Heavily Doped Semiconductor Nanocrystal Quantum Dots, Science, 332 (2011) 77-81.
[151] R. Saran, R. Curry, Lead sulphide nanocrystal photodetector technologies, Nature Photonics, 10 (2016) 81-92.
[152] X. Liu, M. Yu, H. Kim, M. Mameli, F. Stellacci, Determination of monolayer-protected gold nanoparticle ligand-shell morphology using NMR, Nature Commun., 3 (2012).
[153] L. Piveteau, T.-C. Ong, A.J. Rossini, L. Emsley, C. Coperet, M.V. Kovalenko, Structure of Colloidal Quantum Dots from Dynamic Nuclear Polarization Surface Enhanced NMR Spectroscopy, J. Am. Chem. Soc., 137 (2015) 13964-13971.
[154] E.A. Chekhovich, M.N. Makhonin, A.I. Tartakovskii, A. Yacoby, H. Bluhm, K.C. Nowack, L.M.K. Vandersypen, Nuclear spin effects in semiconductor quantum dots, Nature Mater., 12 (2013) 494-504.
[155] A.J. Morris-Cohen, M. Malicki, M.D. Peterson, J.W.J. Slavin, E.A. Weiss, Chemical, Structural, and Quantitative Analysis of the Ligand Shells of Colloidal Quantum Dots, Chem. Mater., 25 (2013) 1155-1165.
[156] M.G. Berrettini, G. Braun, J.G. Hu, G.F. Strouse, NMR analysis of surfaces and interfaces in 2-nm CdSe, J. Am. Chem. Soc., 126 (2004) 7063-7070.
[157] F.V. Mikulec, M. Kuno, M. Bennati, D.A. Hall, R.G. Griffin, M.G. Bawendi, Organometallic synthesis and spectroscopic characterization of manganese-doped CdSe nanocrystals, J. Am. Chem. Soc., 122 (2000) 2532-2540.
[158] J. Cure, Y. Coppel, T. Dammak, P.F. Fazzini, A. Mlayah, B. Chaudret, P. Fau, Monitoring the Coordination of Amine Ligands on Silver Nanoparticles Using NMR and SERS, Langmuir, 31 (2015) 1362-1367.
[159] R. Gomes, A. Hassinen, A. Szczygiel, Q. Zhao, A. Vantomme, J.C. Martins, Z. Hens, Binding of Phosphonic Acids to CdSe Quantum Dots: A Solution NMR Study, J. Phys. Chem. Lett., 2 (2011) 145-152.
[160] M. Malicki, K.E. Knowles, E.A. Weiss, Gating of hole transfer from photoexcited PbS quantum dots to aminoferrocene by the ligand shell of the dots, Chem. Comm., 49 (2013) 4400-4402.

[161] R.D. Harris, V.A. Amin, B. Lau, E.A. Weiss, Role of Interligand Coupling in Determining the Interfacial Electronic Structure of Colloidal CdS Quantum Dots, ACS Nano, 10 (2016) 1395-1403.
[162] D.J. Weinberg, S.M. Dyar, Z. Khademi, M. Malicki, S.R. Marder, M.R. Wasielewski, E.A. Weiss, Spin-Selective Charge Recombination in Complexes of CdS Quantum Dots and Organic Hole Acceptors, J. Am. Chem. Soc., 136 (2014) 14513-14518.
[163] K.E. Knowles, M. Malicki, R. Parameswaran, L.C. Cass, E.A. Weiss, Spontaneous Multielectron Transfer from the Surfaces of PbS Quantum Dots to Tetracyanoquinodimethane, J. Am. Chem. Soc., 135 (2013) 7264-7271.
[164] M.W. Makinen, D. Mustafi, S. Kasa, ENDOR of Spin Labels for Structure Determination: from Small Molecules to Enzyme Reaction Intermediates, in: L.J. Berliner (Ed.) Biol. Magn. Reson., Kluwer Academic Publisher, Ohio, 2002.
[165] P.P. Borbat, A.J. Costa-Filho, K.A. Earle, J.K. Moscicki, J.H. Freed, Electron spin resonance in studies of membranes and proteins, Science, 291 (2001) 266-269.
[166] G. Jeschke, Y. Polyhach, Distance measurements on spin-labelled biomacromolecules by pulsed electron paramagnetic resonance, Phys. Chem. Chem. Phys., 9 (2007) 1895-1910.
[167] P.G. Baranov, S.B. Orlinskii, C.D. Donega, J. Schmidt, High-frequency EPR, ESE, and ENDOR spectroscopy of Co- and Mn-doped ZnO quantum dots, Phys. Status Solidi B, 250 (2013) 2137-2140.
[168] B.V. Yavkin, G.V. Mamin, S.B. Orlinskii, M.R. Gafurov, M.K. Salakhov, T.B. Biktagirov, E.S. Klimashina, V.I. Putlayev, Y.D. Tretyakov, N.I. Silkin, Pb^{3+} radiation defects in $Ca_9Pb(PO_4)_6(OH)_2$ hydroxyapatite nanoparticles studied by high-field (W-band) EPR and ENDOR, Phys. Chem. Chem. Phys., 14 (2012) 2246-2249.
[169] M. Gafurov, T. Biktagirov, G. Mamin, E. Klimashina, V. Putlayev, L. Kuznetsova, S. Orlinskii, The Interplay of manganese and nitrate in hydroxyapatite nanoparticles as revealed by pulsed EPR and DFT, Phys. Chem. Chem. Phys., 17 (2015) 20331-20337.
[170] A.S. Barnard, Diamond standard in diagnostics: nanodiamond biolabels make their mark, Analyst, 134 (2009) 1751-1764.
[171] R. Schirhagl, K. Chang, M. Loretz, C. Degen, M. Johnson, T. Martinez, Nitrogen-Vacancy Centers in Diamond: Nanoscale Sensors for Physics and Biology, Annual Review of Physical Chemistry, Vol 65, 65 (2014) 83-105.

[172] F. Jelezko, J. Wrachtrup, Single defect centres in diamond: A review, Phys. Status Solidi A, 203 (2006) 3207-3225.

[173] F. Moro, L. Turyanska, J. Granwehr, A. Patanè, Spin manipulation and spin-lattice interaction in magnetic colloidal quantum dots, Phys. Rev. B, 90 (2014) 205428.

[174] S. Stoll, A. Schweiger, EasySpin, a comprehensive software package for spectral simulation and analysis in EPR, J. Magn. Reson., 178 (2006) 42-55.

[175] F. Moro, L. Turyanska, J. Wilman, A.J. Fielding, M.W. Fay, J. Granwehr, A. Patane, Electron spin coherence near room temperature in magnetic quantum dots, Sci. Rep., 5 (2015).

[176] S.A. Dikanov, Y. Tsvetkov, Electron Spin Echo Envelope Modulation (ESEEM) Spectroscopy, CRC Press1992.

[177] B.E. Sturgeon, J.A. Ball, D.W. Randall, R.D. Britt, ^{55}Mn Electron-Spin Echo ENDOR Of Mn^{2+} Complexes, J. Phys. Chem., 98 (1994) 12871-12883.

[178] R. Boettcher, A. Poeppl, M. Lorenz, S. Friedlaender, D. Spemann, M. Grundmann, Mn-55 pulsed ENDOR spectroscopy of Mn^{2+} ions in ZnO thin films and single crystal, J. Magn. Reson., 245 (2014) 79-86.

[179] L. Turyanska, R.J.A. Hill, O. Makarovsky, F. Moro, A.N. Knott, O.J. Larkin, A. Patanè, A. Meaney, P.C.M. Christianen, M.W. Fay, R.J. Curry, Tuneable paramagnetic susceptibility and exciton g-factor in Mn-doped PbS colloidal nanocrystals, Nanoscale, 6 (2014) 8919-8925.

[180] S.T. Ochsenbein, D.R. Gamelin, Quantum oscillations in magnetically doped colloidal nanocrystals, Nature Nanotech., 6 (2011) 111-114.

[181] A.T. Murray, M.J.H. Dowley, F. Pradaux-Caggiano, A. Baldansuren, A.J. Fielding, F. Tuna, C.H. Hendon, A. Walsh, G.C. Lloyd-Jones, M.P. John, D.R. Carbery, Catalytic Amine Oxidation under Ambient Aerobic Conditions: Mimicry of Monoamine Oxidase B, Ang. Chem. Int. Ed., 54 (2015) 8997-9000.

[182] S. Baumann, W. Paul, T. Choi, C.P. Lutz, A. Ardavan, A.J. Heinrich, Electron paramagnetic resonance of individual atoms on a surface, Science, 350 (2015) 417-420.

[183] G. Jeschke, A. Schweiger, Chirp Hyperfine Spectroscopy, J. Magn. Res., 119 (1996) 45-52.

[184] U. Nielsen, I. Heinmaa, A. Samoson, J. Majzlan, C. Grey, Insight into the Local Magnetic Environments and Deuteron Mobility in Jarosite

($AFe_3(SO_4)_2(OD,OD_2)_6$, A = K, Na, D_3O) and Hydronium Alunite ((D_3O)$Al_3(SO_4)_2(OD)_6$), from Variable-Temperature ^2H MAS NMR Spectroscopy, Chemistry of Materials, 23 (2011) 3176-3187.

[185] J. Granwehr, J. Leggett, W. Kockenberger, A low-cost implementation of EPR detection in a dissolution DNP setup, Journal of Magnetic Resonance, 187 (2007) 266-276.

[186] P.J. Roberts, EPR relaxation: progress in hardware and analysis methods. School of Physics & Astronomy, University of Nottingham, UK, 2013.

[187] S. Fu, Polymers at Cryogenic Temperatures, Springer2013.

[188] J.C. Murphy, Tunable esr cavity suitable for high
frequency field modulation, Review of Scientific Instruments, 39 (1968) 135-&.

[189] J. Legget, Multi-Layer Gradient Coil Design, Physics and astronomy, University of Nottingham, 2004.

[190] J. Leggett, S. Crozier, S. Blackband, B. Beck, R. Bowtell, Multilayer transverse gradient coil design, Concepts in Magnetic Resonance Part B-Magnetic Resonance Engineering, 16B (2003) 38-46.